2022 RMZ – M&G **Vol. 69** No. 2

RMZ

MATERIALS and GEOENVIRONMENT

MATERIALI in GEOOKOLJE

RMZ – M&G, **Vol. 69**, No. 2
pp. 67–130 (2022)

Ljubljana, December 2022

Table of Contents

Kazalo

Original scientific articles
Izvirni znanstveni članki

Original Scientific Article • DOI: 10.2478/rmzmag-2021-0016

Received: July 19, 2022
Accepted: July 29, 2022

Microstructure of a nickel insert, a special copper alloy, and a cast joint between them

Mikrostruktura nikljevega vstavka, posebne bakrove zlitine in litega spoja med njima

Iztok Naglič[1,*], Žan Kresnik[2], Andrej Resnik[2], Boštjan Markoli[1]

[1]University of Ljubljana, Faculty of Natural Sciences and Engineering, Aškerčeva cesta 12, 1000 Ljubljana, Slovenia

[2]OMCO Metals Slovenia d.o.o., Cesta Žalskega tabora 10, 3310 Žalec, Slovenia

*Corresponding author: E-mail: iztok.naglic@ntf.uni-lj.si

Abstract in English

This work deals with the characterisation of the microstructure of a nickel insert, a special copper alloy and the cast joint between them after their use as a glass manufacturing mould. The microstructure was characterised by optical microscopy, scanning electron microscopy and microanalysis by energy dispersive X-ray spectroscopy.

It was found that the nickel insert contained 7 at. % Si and 0.3 at. % Fe. The special copper alloy contains undesirable phases or compounds, including lead, aluminium-based oxides and borides. The borides are either iron-, iron-chromium- or chromium-based with different stoichiometries between metal components and boron. The cast joint between the nickel insert and the special copper alloy has evidence of mixing the two alloys, while only in some areas porosity and oxides prevented the formation of a suitable cast joint. Aluminium-based oxides and some borides could be the cause of the formation of cracks due to their morphology.

Keywords: nickel alloy, copper alloy, microstructure, microanalysis

Povzetek

Delo obravnava karakterizacijo mikrostrukture nikljevega vstavka, posebne bakrove zlitine in litega spoja med njima po uporabi kot kalupa za oblikovanje stekla. Mikrostrukturo smo karakterizirali z optično mikroskopijo, vrstično elektronsko mikroskopijo in mikroanalizo z energijsko disperzijsko rentgensko spektroskopijo.

Ugotovljeno je bilo, da nikljev vstavek vsebuje 7 at. % silicija in 0,3 at. % železa. Posebna bakrova zlitina vsebuje nezaželene faze, kot so svinec, oksidi na osnovi aluminija in boridi. Boridi so železovi, železo-kromovi ali le kromovi z različnimi stehiometrijami med kovinami in borom. Na litem spoju med nikljevim vstavkom in posebno bakrovo zlitino je opazno mešanje obeh zlitin, le na nekaterih mestih pa so poroznost in oksidi preprečili nastanek ustreznega litega spoja. Oksidi na osnovi aluminija in nekateri boridi lahko zaradi svoje morfologije povzročijo nastanek razpok.

Ključne besede: nikljeva zlitina, bakrova zlitina, mikrostruktura, mikroanaliza

Introduction

Moulds for glass production are usually made of special copper alloys. Standardised copper alloys for these purposes are designated as C99300 and C99350 according to UNS [1–3]. In addition to copper, these alloys usually contain some nickel, aluminium, zinc, and iron as the main alloying elements and should have high hardness, oxidation resistance, and resistance to thermal fatigue. In the glass mould industry, a slightly modified special copper alloy is often used, which in addition to copper also contains 15–16.5 wt. % Ni, 9.5–10.0 wt. % Al, 7.5–9.0 wt. % Zn, 0.8–1.2 wt. % Si and up to 1.25 wt. % Fe, 0.2 wt. % Mn, 0.15 wt. % P, 0.1 wt. % Sn, 0.1 wt. % Pb, 0.1 wt. % Cr, 0.1 wt. % Mg and 0.1 wt. % Sb. The microstructure of these alloys generally consists of face-centred cubic α_{Cu} and cubic β-AlNi intermetallic phases or compounds with

space group Pm-3m (CsCl prototype) [4, 5]. A considerable amount of copper is soluble in the intermetallic β-AlNi phase, which affects its lattice parameters and mechanical properties [6].

The moulds for making glass have nickel inserts and nickel plates in certain places. The nickel inserts have a cast joint with a special copper alloy, while the nickel plates are welded to a special copper alloy using a boron-containing additive. This boron can form very stable borides with iron and chromium [7-9]. The moulds for glass production are recycled together with the nickel inserts and plates after their end-of-life cycle. The amount of recycled material in the production of a new special copper alloy is limited because of the need to obtain the correct chemical composition of the alloy and to limit other undesirable compounds that accumulate in the alloy.

The objective of this work was to characterise the composition and microstructure of the nickel insert, the special copper alloy, and the cast joint after their end-of-life cycle as a glass manufacturing mould.

Materials and methods

This paper characterises the microstructure of the cast joint between a nickel insert and a special copper alloy, which is part of a mould used for the production of glass products. The special copper alloy presented in this work was made from used casting moulds. This mould was analysed after the end of its life cycle. The joint between a nickel insert and a special copper alloy was cut out of the used mould. Smaller pieces were mounted and metallographically prepared for light and scanning electron microscopy by grinding and polishing with diamond paste. Final polishing was performed with a SiO_2 suspension.

Characterisation of the microstructure of the nickel insert, the special copper alloy and its cast joint was performed using optical microscopy, scanning electron microscopy (SEM), and microanalysis. Light microscopy was performed using a Zeiss Axio Imager A1m with AxioCam ICc 3 and AxioVision software, while SEM and microanalysis were performed using a JEOL JSM-7600F scanning electron microscope with field emission gun and energy dispersive X-ray spectroscopy (EDS) at an accelerating voltage of 20 kV.

Results and discussion

The average chemical composition, determined by EDS, is shown in Table 1. The results show that the nickel insert consists of silicon and iron in addition to nickel. The microstructure of a nickel insert is shown in Figure 1. The light microscopy image of the microstructure in Figure 1a shows that large nickel dendrites are present. The backscattered electron image (BE) of the interdendritic region is shown in Figure 1b. This region consists of a heterogeneous structure of nickel and one or more intermetallic phases, which could be either β_3-Ni_3Si, β_2-Ni_3Si, γ-$Ni_{31}Si_{12}$ or β_1-Ni_3Si according to the binary Ni-Si system [10–12]. According to this system, 3.5 wt. % Si lowers the liquidus and solidus to about 1380 and 1310 °C, respectively.

Figure 2 shows the microstructure of the special copper alloy. The chemical composition of this alloy, determined by EDS, is given in Table 2. Among the elements found in the alloy, the most important is iron, whose content is limited in these alloys. Solidification of such an alloy begins with primary solidification of the intermetallic β-AlNi phase, followed by a eutectic reaction forming a heterogeneous structure of α_{Cu} and β-AlNi [13]. Upon further cooling, the solubility of copper in the β-AlNi phase decreases, and α_{Cu} precipitates within the intermetallic β-AlNi phase [13]. In addition to these two phases, other phases are present as inclusions in the microstructure. These phases are present due to recycling. As shown in Figure 2c, these phases are darker than α_{Cu} and the intermetallic β-AlNi phase. This fact indicates that these regions consist of a significant amount of elements with low atomic number.

Table 1: *Chemical composition of the nickel insert determined by EDS.*

	Ni	Si	Fe
at. %	92.8	7	0.3
wt. %	96.3	3.5	0.3

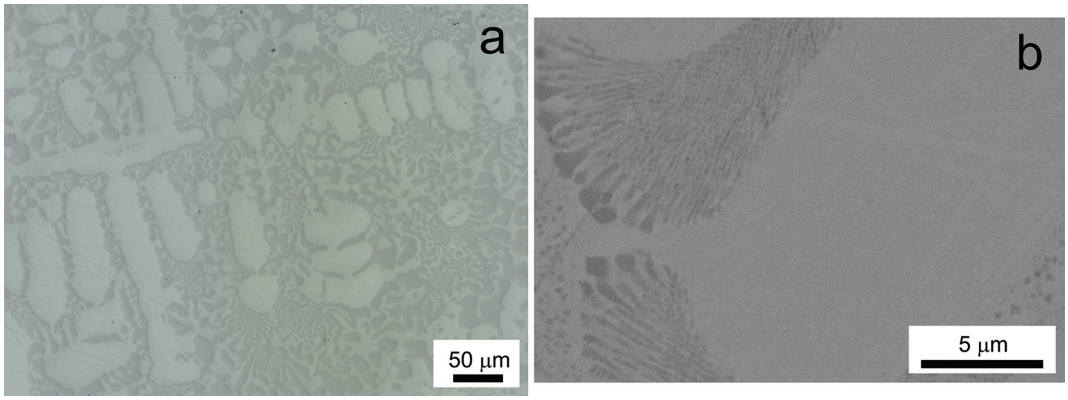

Figure 1: *Light microscopy image (a) and BE image (b) of the nickel insert.*

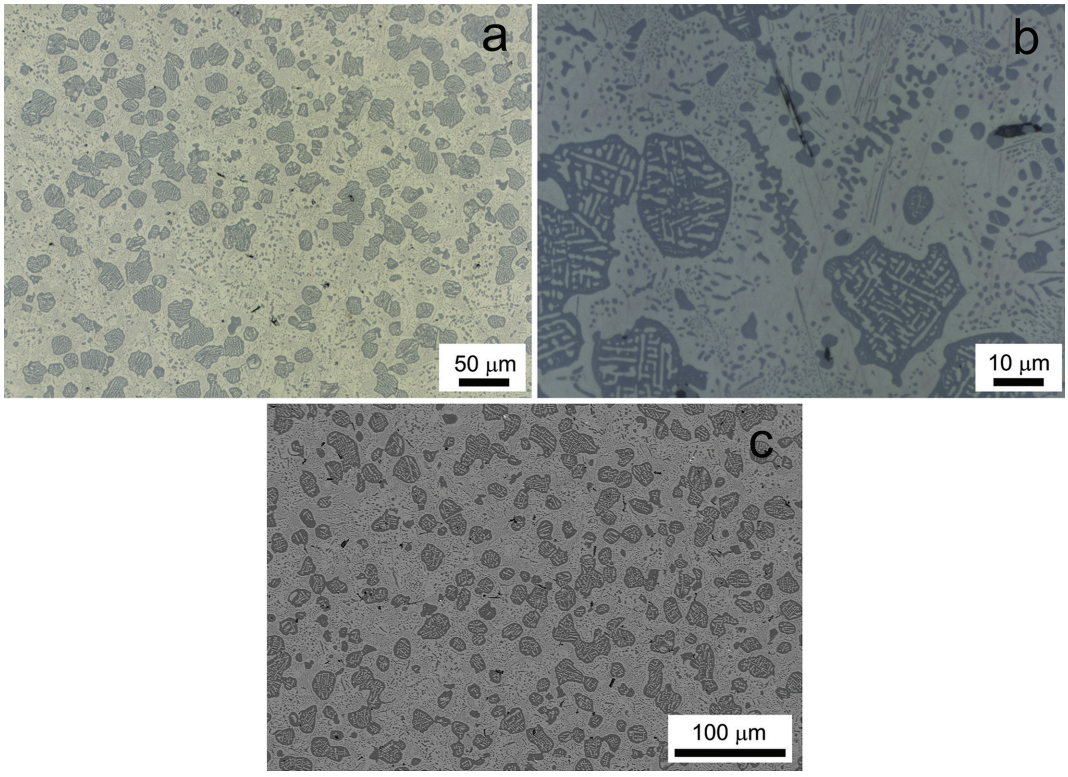

Figure 2: *Light (a, b) and BE (c) images of the microstructure of a special copper alloy.*

Table 2: *Chemical composition of the special copper alloy determined by EDS.*

	Cu	Ni	Al	Zn	Si	Fe
at. %	52.6	16.6	21.5	5.9	2.4	1.0
wt. %	61.8	18.0	10.7	7.1	1.2	1.0

Figure 3 shows a higher magnification BE image with marked areas of microanalyses of the special copper alloy containing several darker and lighter phases. The results of the microanalyses are shown in Table 3. The areas labelled 1 and 2 represent lead, which is very bright on the BE image due to its high atomic number. The regions labelled 3 and 4 are

related to darker phases on the BE image and consist predominantly of boron. Region 3 contains mostly chromium, but also some iron and manganese. Other elements, including copper and nickel, are detected due to the low analytical spatial resolution. Considering only boron, chromium, iron, and manganese, this boride has a composition of 78.9 at. % B, 17.2 at. % Cr, 3.6 at. % Fe, and 0.3 at. % Mn. According to the binary B-Cr and B-Fe and ternary B-Cr-Fe and B-Fe-Mn systems [7–9, 14], this boride could be of the CrB_4 type with the space group Immm. This boride can contain up to 7 at. % Fe at an equilibrium temperature of 1080 °C [9].

The boride in Region 4 contains predominantly chromium, iron and manganese, while other elements with significant contents were detected due to low analytical spatial resolution. Considering only these four elements, the composition of this boride is 67.5 at. % B, 16.1 at. % Cr, 15.5 at. % Fe and 0.9 at. % Mn. The composition of this boride is very close to the CrB_2 boride type with space group P6/mmm [7, 9]. According to the ternary B-Cr-Fe system [9], this boride can only contain up to 2 at. % Fe at 1080 °C. However, the temperature commonly used in melting and holding the melt of this particular copper alloy is much higher. The liquidus temperature for the copper alloy in question was found to be between 1170 and 1180 °C [13], while the melt is normally held at temperatures at least 100 °C higher during the production process. This means that the borides are kept at temperatures probably at least 200 °C higher than the temperature designated in the ternary B-Cr-Fe system [9]. This could also mean that the solubility of the iron could be higher at these temperatures. Lastly, it is possible that the boride itself is not an equilibrium phase at all. The solubility of the 0.9 at. % Mn is quite likely; however, since manganese itself forms MnB_2 with the same crystal structure and space group P6/mmm, it is hard to tell them apart [14, 15]. Yet, the boride in Region 4 exhibits an acicular morphology, which is a typical characteristic of hexagonal phases or compounds.

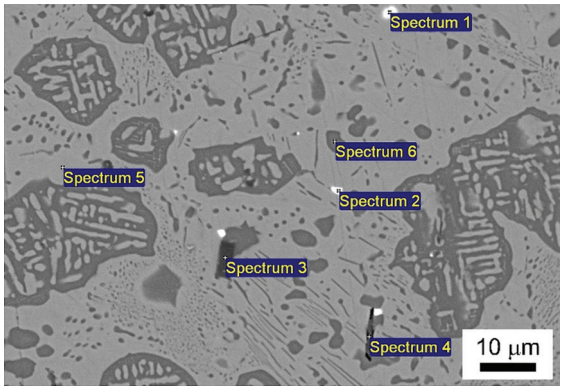

Figure 3: *BE Image of the microstructure of a special copper alloy with marked areas of microanalyses.*

Region 5 corresponds to a copper-rich cubic solid solution that also contains aluminium, zinc and some nickel. Region 6 is related to the β-AlNi intermetallic phase that contains aluminium and nickel as well as copper, silicon and some iron. The detection of zinc in Region 6 is most likely again the result of low analytical spatial resolution.

Figure 4 shows the BE image of the special copper alloy at various magnifications. Figure 4b also shows the regions of the microanalyses, which correspond to a darker particle similar to the borides in Figure 3 in the first case and a large dark and thin phase in the second and third. The results of the microanalyses are shown in Table 4.

Table 3: *EDS microanalyses of the areas shown in Figure 3 in at. %.*

	B	O	Al	Si	P	Ti	Cr	Mn	Fe	Ni	Cu	Zn	Mo	Pb
1	-	11.4	2.2	-	-	-	-	-	-	2.8	24.8	2.3	-	56.5
2	-	10.6	7.9	-	-	-	-	-	0.7	12.9	35.6	4.1	-	28.2
3	75.5	-	0.2	0.1	0.2	0.1	16.5	0.3	3.4	1.1	1.9	0.2	0.3	-
4	62.3	-	1.3	0.2	0.4	-	14.9	0.8	14.3	1.8	3.7	0.4	-	-
5	-	-	10.5	0.8	-	-	-	-	0.3	3.4	76.7	8.2	-	-
6	-	-	32.9	5.2	-	-	-	0.2	1.9	34.2	23.3	2.3	-	-

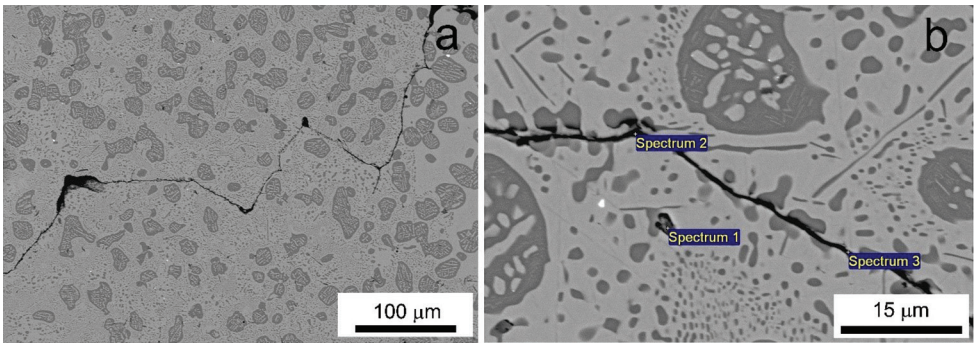

Figure 4: *BE Images of the microstructure of a special copper alloy (a) and magnified detail with marked areas of microanalyses (b).*

Table 4: *EDS Microanalysis of the areas shown in Figure 4b in at. %.*

	B	O	Mg	Al	Si	S	Cr	Mn	Fe	Ni	Cu	Zn	Pb	F
1	52.6			0.69			0.57	1.15	38.1	1.61	2.06			3.21
2		42.7	5.7	22.2		0.3			0.3	1.7	24.4	2.8		
3		35.5	4.3	19	0.7				0.5	11	24.9	3.9	0.3	

The particle in Region 1 represents the boride, which also contains iron, manganese, and chromium. Considering only boron, iron, manganese, and chromium, the composition of this boride is 56.9 at. % B, 41.2 at. % Fe, 1.2 at. % Mn, and 0.6 at. % Cr. Since this boride contains mainly only iron, we can primarily use the B-Fe binary system to look for a possible candidate. According to the binary system, only FeB exists with the space group Pbmn containing 50.0 at. % B. The other boride from the same binary system contains even less boron [8]. The borides from the ternary systems B-Cr-Fe and B-Fe-Mn [9, 14] all contain much smaller amounts of iron, so FeB, which also has infinite solubility of manganese and chromium, is the closest equilibrium phase. However, it is more likely that this boride is metastable and will continue to transform to a more stable form during cooling and service time.

Regions 2 and 3 correspond to a thin dark line, which, as shown by the analyses in Table 4, is aluminium oxide that also contains some magnesium. Other elements with significant contents are probably detected because of the low analytical spatial resolution. The formation of an aluminium-based oxide is to be expected since aluminium is the alloying element with the most thermodynamically stable oxides in this alloy and, consequently, all surfaces exposed to oxygen would form this oxide. Such oxides are commonly found in these alloys.

Figure 5 shows light and BE images of the cast joint between the nickel insert and the special copper alloy and a dark thin line near the joint that resembles the oxides described earlier. Figure 5a shows part of a cast joint where mixing of both alloys took place. Such a joint is desirable. Figure 5b, on the other hand, shows an area of the joint where dark pores and a thin dark line are both present at the boundary between the special copper alloy and the nickel insert. It can be seen that no mixing took place in this part of the joint. Such areas are undesirable due to their inferior mechanical properties. In addition, these areas probably contain an oxide layer common in the investigated copper alloy, which by itself prevents the mixing of the two alloys. The shape of this oxide layer can also lead to the cracking and ultimate fracture of such a mould during service time. Figure 5c shows the BE image of a cast joint with a thin dark line near the joint similar to the aluminium-based oxides characterised earlier. In Figure 5d, this part is shown enlarged, and microanalyses were performed in two areas, as shown in Table 5. Both analyses confirm that aluminium-based oxides are present in both regions and probably contain some magnesium, chromium, and silicon. Other

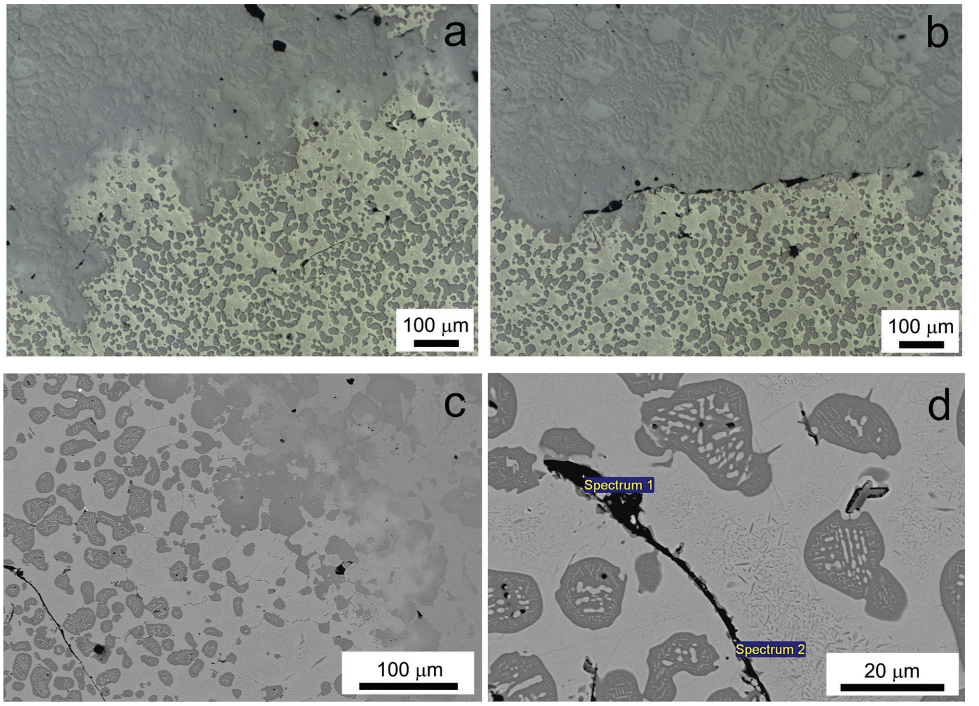

Figure 5: *Light (a, b) and BE images (c, d) of the microstructure of a special copper alloy.*

Table 5: *EDS microanalysis of the areas shown in Figure 5d in at. %.*

	O	Na	Mg	Al	Si	S	Ca	Cr	Mn	Fe	Ni	Cu	Zn
1	55.8	0.9	3.6	16.5	5.4	0.2	0.5	0.8	-	1.1	2.9	11.3	1.0
2	54.5	-	4.0	21.0	3.4	-	0.4	1.1	0.2	1.5	2.7	10.0	1.1

elements were most likely detected due to the low analytical spatial resolution.

The results of this work show that the special copper alloy contains several undesirable phases, many of which are a consequence of recycling. Lead and boride inclusions are certainly a result of recycling, while aluminium-based oxides found were probably formed during casting. However, aluminium-based oxides can also survive during remelting if not removed physically. These oxides could lead to the moulds cracking. Borides also accumulate in the alloy as a result of recycling. The borides found in this work are either iron-, iron-chromium-, or chromium-based, and all contain some manganese. These borides also have different morphologies and stoichiometries with respect to the metal/boron ratio and are not necessarily equilibrium phases. Some morphologies, such as the acicular morphology shown in Figure 3, could also be potentially harmful, as they can lead to the formation of cracks.

Conclusions

This work deals with the composition and microstructure of the nickel insert, the special copper alloy, and the cast joint between them.

The results show that the nickel insert contains 7 at. % Si and 0.3 at. % Fe. The special copper alloy, in addition to the intermetallic β-AlNi phase and the cubic copper-based solid solution, also contains some undesirable phases, including lead, aluminium-based oxides, and borides. Borides can be either iron-based, iron-chromium-based, or chromium-based with different stoichiometries for metallic components and boron. All of these borides also contain small amounts of manganese. Aluminium-based

oxides and some borides can potentially lead to cracking due to their morphology. The cast joint between the nickel insert and the special copper alloy generally shows mixing of the two alloys, which is desirable. In some areas of the joint, we observed porosity and, most likely, an oxide layer that prevented the two alloys from mixing. Such parts of the joint are not desirable, as they deteriorate the mechanical properties of the joint.

Acknowledgements

The authors would like to acknowledge the financial support of the Slovenian Research Agency through the research programme P1-0195.

References

[1] Taylor, D.E., Black, W.T. (1992): Introduction to Copper and Copper Alloys. In: *ASM Handbook, Volume 2 – Properties and selection: Nonferrous Alloys and Special-Purpose Materials*, ASM International Handbook Committee (eds.). ASM International, Materials Park, Ohio, p. 228.

[2] C99300 [online]. Copper Development Association Inc. [cited 23/08/2022]. Available on: *https://alloys.copper.org/alloy/C99300*.

[3] C99350 [online]. Copper Development Association Inc. [cited 23/08/2022]. Available on: *https://alloys.copper.org/alloy/C99350*.

[4] Wang, C.H., Chen, S.W., Chang, C.H., Wu, J.C. (2003): Phase Equilibria of the Ternary Al-Cu-Ni System and Interfacial Reactions of Related Systems at 800 °C. *Metallurgical and Materials Transactions A*, 34A, pp. 199–209.

[5] Wang, W., Chen, H.L., Larsson, H., Mao, H. (2019): Thermodynamic constitution of the Al–Cu–Ni system modeled by CALPHAD and ab initio methodology for designing high entropy alloys. *Calphad*, 65, pp. 346–369, DOI:10.1016/j.calphad.2019.03.011.

[6] Colín, J., Serna, S., Campillo, B., Rodríguez, R.A., Juárez-Islas, J. (2010): Effect of Cu additions over the lattice parameter and hardness of the NiAl intermetallic compound. *Journal of Alloys and Compounds*, 489, pp. 26–29, DOI:10.1016/j.jallcom.2009.09.034.

[7] Liao, P.K., Spear, K.E. (1986): B-Cr. In: *ASM Handbook, Volume 3–Alloy Phase Diagrams*, ASM International Handbook Committee (eds.). ASM International, Materials Park, Ohio, p. 81.

[8] Liao, P.K., Spear K.E. (unpublished): B-Fe. In: *ASM Handbook, Volume 3–Alloy Phase Diagrams*, ASM International Handbook Committee (eds.). ASM International, Materials Park, Ohio, p. 81.

[9] Homolová, V., Hiripová, L. (2017): Experimental Investigation of Isothermal Section of the B-Cr-Fe Phase Diagram at 1353K. *Advances in Materials Science and Engineering*, ID 2703986, pp. 1–7, DOI:10.1155/2017/2703986.

[10] Nash, P., Nash, A. (1991): Ni-Si. In: *ASM Handbook, Volume 3–Alloy Phase Diagrams*, ASM International Handbook Committee (eds.). ASM International, Materials Park, Ohio, p. 318.

[11] Baker, I., Yuan, J., Schulson, E.M. (1993): Formation of $L1_2$-Structured Ni_3Si. *Metallurgical and Materials Transactions A*, 24A, pp. 283–292.

[12] Tokunaga, T., Nishio, K., Ohtani, H., Hasebe, M. (2003): Thermodynamic assessment of the Ni–Si system by incorporating ab initio energetic calculations into the CALPHAD approach. *Calphad*, 27, pp. 161–168, DOI:10.1016/S0364-5916(03)00049-X.

[13] Zupanič, F., Bončina, T., Medved, J., Vončina, M. (2018): *Študija strjevanja nikelj-aluminijevega brona 3 OMX z mikrostrukturno, EDS-mikrokemično, DTA, XRD analizo ter modeliranja s programom Thermocalc*. Fakulteta za strojništvo: Maribor, 26 p.

[14] Repovský, P., Homolová, V., Čiripová, L., Kroupa, A., Zemanová, A. (2016): Experimental study and thermodynamic modelling of the B-Fe-Mn ternary system. *Calphad*, 55, pp. 252–259, DOI:10.1016/j.calphad.2016.10.002.

[15] Liao, P.K., Spear, K.E. (1986): B-Mn. In: *ASM Handbook, Volume 3–Alloy Phase Diagrams*, ASM International Handbook Committee (eds.). ASM International, Materials Park, Ohio, p. 82.

Original Scientific Article • DOI: 10.2478/rmzmag-2021-0018

Received: April 08, 2022
Accepted: June 03, 2022

Rare Earth Element Geochemistry and Abundances in Syenites and Charnockitic Rocks of Selected Locations within Southwestern Nigeria

Geokemija prvin redkih zemelj in njihova vsebnost v sienitih in čarnokitnih kamninah z izbranih lokacij v jugozahodni Nigeriji

Olugbenga Akindeji Okunlola[1], Oluwabusayo Mary Ajibola[1,*], Olusegun Gbenga Olisa[2]

[1]Department of Geology, University of Ibadan, Ibadan

[2]Department of Earth Sciences, Olabisi Onabanjo University Ago-Iwoye, Ogun State, Nigeria

*Corresponding author: E-mail: ajibolabusayo4@gmail.com

Abstract in English

Rare earth elements (REE) are critical metals widely used in modern technology. There is an increased demand for these elements which has necessitated additional exploration. The REE geochemistry of syenites and charnockitic rocks from selected locations within southwestern Nigeria were studied to determine their concentrations, distribution patterns, and mineralisation potential to deduce if they can be economically exploited. Mineralogical studies were carried out using scanning electron microscopy (SEM). Ten rock samples including five syenites and five charnockites were analysed for their elemental composition using inductively coupled plasma – mass spectrometry (ICP-MS). The REE-bearing minerals identified from the SEM analysis include apatite and monazite. The fractionation ratio $(La/Yb)_N$ ranged from 29.36 to 48.75 for the syenites and from 24.43 to 48.29 for the charnockites, indicating magmatic differentiation. Total REE (∑REE) in the syenites (342–675 ppm) and charnockites (220–802 ppm) suggests that they are enriched with respect to REE but the REE concentration in the rocks of the study area had very low ∑REE compared to the REE contents of the rocks where they have been mined and may therefore not be economically viable.

Keywords: rare earth elements, syenites, charnockites, abundances, fractionation

Povzetek

Prvine redkih zemelj (REE) so kritične kovine, široko uporabljane v moderni tehnologiji. Povečano povpraševanje po teh prvinah vodi v dodatna raziskovanja. V izbranih lokacijah jugozahodne Nigerije smo v sienitih in čarnokitnih kamninah določili vsebnosti REE, porazdelitvene vzorce in mineralizacijski potencial, da bi ugotovili upravičenost ekonomskega izkoriščanja. Mineraloške raziskave so bile opravljene z vrstičnim elektronskim mikroskopom (SEM). Elementna sestava desetih vzorcev, od tega pet sienitov in pet čarnokitov, je bila določena z induktivno sklopljeno plazemsko masno spektrometrijo (ICP-MS). S SEM smo kot nosilca REE prepoznali apatit in monacit. Frakcionacijsko razmerje $(La/Yb)_N$ ima za sienite razpon od 29,36 do 48,75, za čarnokite 24,43–48,29, kar kaže na magmatsko diferenciacijo. Skupna vsebnost REE (∑REE) v sienitih (342–675 ppm) in čarnokitih (220–802 ppm) nakazuje na obogatitev REE, so pa vsebnosti REE v raziskanih vzorcih nižje od tistih, ki jih izkazujejo kamnine iz trenutno rentabilnih rudnikov, zato ekonomsko izkoriščanje preiskanih sienitov in čarnokitov ni upravičeno.

Ključne besede: elementi redkih zemelj, sieniti, čarnokiti, vsebnost, frakcionacija

Introduction

Rare earth elements (REE) have attracted much attention in recent years due to their high significance to the entire human population. Their importance in the production of modern technological applications cannot be underestimated, and their global reserve, which is gradually diminishing, has led to an increased demand for these elements. As the global demand for REE increases, the exploration of new REE deposits is essential [1].

Economically, the REE mineralisation and deposits include two separate types: light rare earth element (LREE) deposits and heavy rare earth element (HREE) deposits. Most LREE are produced from carbonatite deposits. Ion-adsorption clay deposits in southern China (referred to as "south China clays") are currently the world's main source of HREE, they have low REE content, but they are economical because the REE can be easily extracted from them. The second significant HREE sources are alkaline rock-hosted deposits containing HREE and Y as their primary product or co-product. The deposits containing HREE generally tend to be lower grade than the LREE deposits. However, the HREE, based on unit value, can be more valuable and their low-grade deposits may still be economically exploitable [2]. LREE are generally more abundant, and less valuable than the HREE.

Many studies have been carried out in various areas to check for possible REE potential and recent studies have shown possible potential for REE mineralisation in areas that might have been initially overlooked. Because of the need for more exploration and exploitation of these REEs, there is an awakening call for more studies to be carried out in other areas and in rocks that have not been explored [3].

The focus of this study is on determining the abundances of REEs in syenites and charnockitic rocks of selected areas in southwestern Nigeria, in order to determine their mineralisation potential. The study area is underlain by the basement complex of Nigeria. Rahaman [4] reviewed the geology of southwestern Nigeria

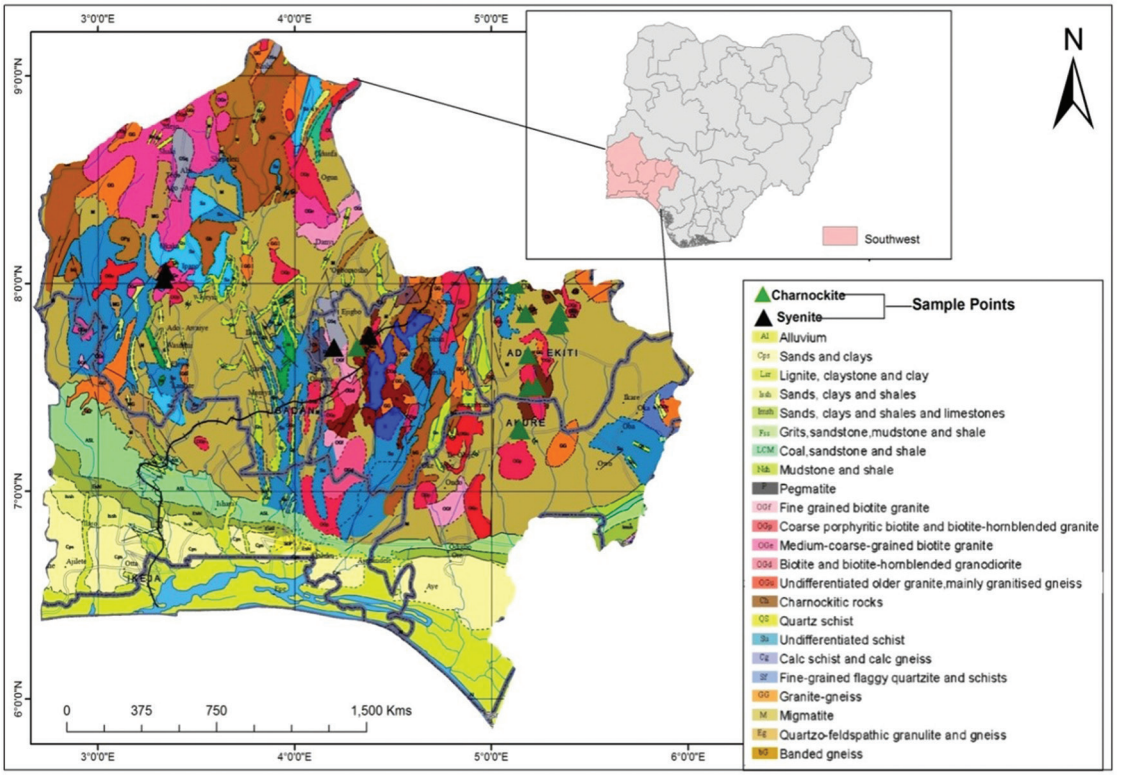

Figure 1: *Geological map of southwestern Nigeria showing the sampling points. (Modified after the Nigerian Geological Survey Agency [5]).*

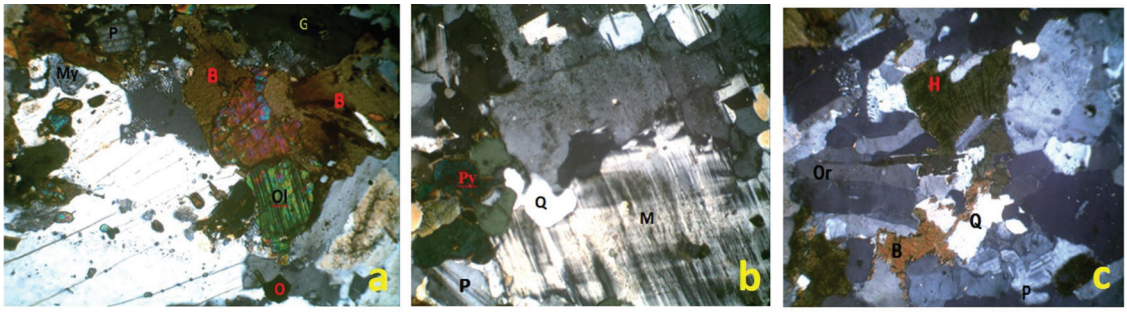

Figure 2: *Photomicrograph of syenites from: (a) Okeho showing B = biotite, P = plagioclase, Ol = Oolivine, My = mymerkite, O = opaque, G = garnet (b) Iwo showing Q = qQuartz, M = microcline, P = plagioclase, Py = pyroxene (c) Kajola showing P = plagioclase, B = biotite, Or = orthoclase, H = hornblende.*

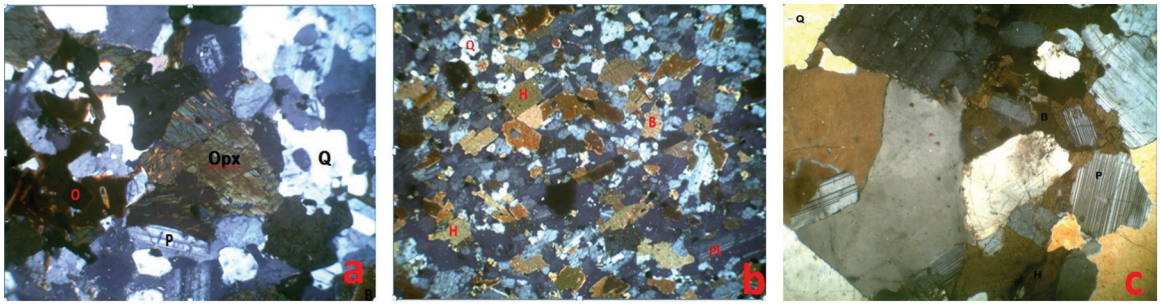

Figure 3: *Photomicrographs of charnockite from a) Akure showing Q = quartz, B = biotite, Opx = orthopyroxene, P = plagioclase, O = opaque; b) Ikere showing Q = quartz, B = biotite, Pl = plagioclase, H = Hornblendeh; and c) Ado showing Q = quartz, B = biotite, P = plagioclase, H = hornblende.*

and recognised six major lithological units, which include (1) the migmatite-gneiss-quartzite complex; (2) the paraschists and metaigneous rocks that consist of pelitic schist, amphibolite, and talcose rocks; (3) metaconglomerates, marbles, and calc-silicate rocks; (4) the charnockitic rocks, (5) the older granites varying in composition from granodiorite to true granites; and (6) potassic syenites and the dolerites. Fifteen different locations around southwestern Nigeria were chosen for the study (Figure 1). The mapped lithological units for these studies are syenites and charnockitic rocks.

Materials and methods

Fresh samples of syenites and charnockitic rocks were obtained during systematic field mapping. Petrographic analysis was carried out at the University of Ibadan. Scanning Electron Microscopy-Energy Dispersive Spectroscopy (SEM-EDS) was used to study possible REE-bearing minerals at the Department of Geology, University of the Free State, South Africa. Ten representative rock samples inclusive of five syenites and five charnockites were analysed for their elemental concentration at the Bureau Veritas Mineral Services, Vancouver, Canada using an inductively coupled plasma-mass spectrometer (ICP-MS).

Results and discussion

Field occurrences and petrographic descriptions

Syenites: The syenites studied were found in the following areas: Awo, Iwo, Okeho, Ayetoro-Oke, and Iwere-Oke. The syenite of Iwo is found as a low-lying and very extensive outcrop; quartzo-feldspathic and pegmatitic veins were observed in the outcrop. It is grey in colour with fine- to medium-grained texture. The Okeho, Ayetoro Oke, and Iwere Oke syenite outcrops were found as low-lying and huge

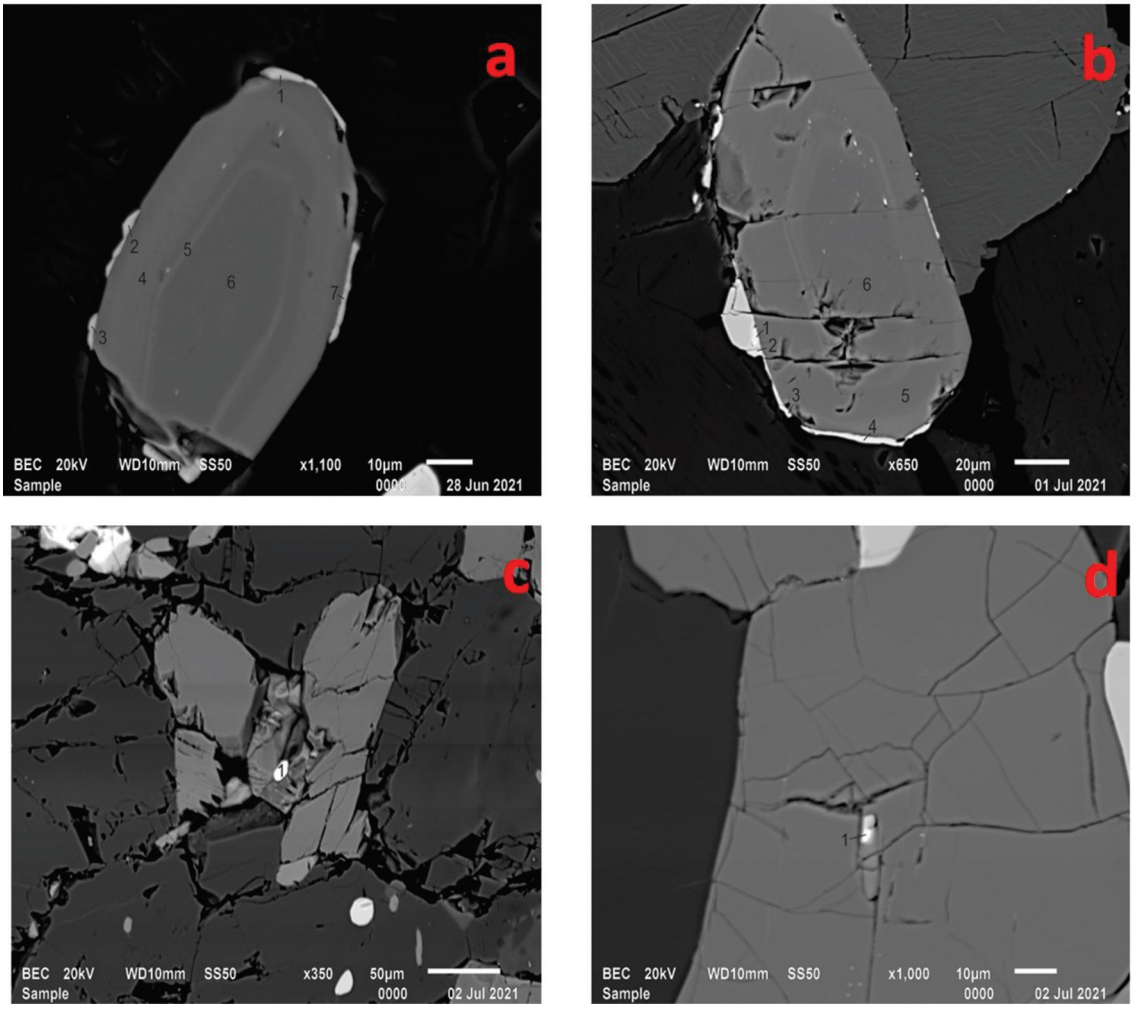

Figure 4: *(a and b): Back-scattered electron (BSE) image of REE-bearing minerals in the rims of zoned apatite from charnockites; (c and d): BSE image of REE-bearing minerals in syenites.*

continuous boulders. They are dark green to dark grey in colour with medium- to coarse-grained texture. The petrographic analysis for syenites reveals mineral assemblages of quartz, plagioclase, biotite, olivine, pyroxenes, hornblende, microcline, augites, and opaque minerals (Figure 2a–c).

Charnockites: The charnockite samples were collected from: Oye, Otun, Ido Osi, Ado, Ikere Ekiti, Akure, and Osuntedo. The charnockitic rocks of Oye occur as low-lying outcrops, boulders, and as road cut in some places. The charnockites in Ado-Ekiti, Ikere, and Akure occur mostly as hills and as large, elongated, and rounded boulders in close association with the porphyritic Older Granite. They are coarse grained with a colour variety ranging from dark green to greenish grey and whitish grey as observed in the sample from Ado-Ekiti. The petrographic analysis revealed mineral assemblages of quartz, plagioclase, orthoclase, biotite, pyroxenes, hornblende, microcline, and opaque minerals (Figure 3a–c).

REE minerals

REE-bearing accessory minerals were studied using their chemical compositions as observed via Scanning Electron Microscopy. The observed REE in the charnockite occurred along the rims of zoned apatite (Ca_5 $(PO_4)_3$ (F,

Cl, OH) grain (Figure 4a and b). The zoning might be due to a change in temperature or composition of the fluid from which the crystal crystalised.

Apatite was observed to be associated with a mineral suspected to be monazite, which is an REE-concentrating mineral more enriched in LREE. REE minerals in syenites are small and scarce (Figure 4 c and d). Their composition is also very different to the REE minerals in the other samples. The REE-bearing mineral identified in the BSE image of the syenite is suspected to be monazite, on the basis based of its chemical compositions (Table 1).

REE geochemistry

The total REE (∑REE) ranges from 342.54 to 675.15 ppm. The syenites are more enriched in LREE, with values ranging from 325.66 to 648.24 ppm, and Ce, being the most prevalent REE, HREE ranged 19.03-26.91 ppm. The Iwo quartz potassic syenite is characterized by higher ∑REE than the syenites from other areas, with a value of 675.15 ppm. The Kajola and Iwere–Oke syenites have comparable values of 469.17 ppm and 462.69 ppm, respectively, for their ∑REE, while the syenites from Ayetoro–Oke have the lowest ∑REE value of 325.66 ppm (Table 2).

The ∑REE of the charnockitic rocks varies with location, ranging from 224.26 ppm in the charnockite of Otun to 801.03 ppm in Akure charnockite. The charnockites are more enriched in LREE with values ranging from 211.28 ppm to 754.03 ppm and relatively depleted in HREE with values ranging from 8.64 ppm to 47.7 ppm. The Akure charnockite is characterised by anomalously high REE contents of 801.03 ppm compared to other charnockites. The syenites and charnockites are characterised by high concentration of LREE and relatively low contents of HREEs with significant LREE/HREE fractionation.

The rocks having more LREE than HREE may be a result of newly formed P-bearing minerals such as apatite or monazite being important carriers of LREE [6, 7]. That the syenites and charnockitic rocks are characterised by high REE concentrations, which is due to the presence of high values of LREE, suggests REE-concentrating minerals (especially monazite, which contains LREE), which indicates that their original magma had crustal input [8].

Table 1: *Chemical composition of the REE minerals in charnockites and syenites.*

	1	2	3	4	5	6	7	8	9
F				2.41	2.57	2.41			
Na_2O			1.88				3.6		
MgO	0.4	0.52	0.61				0.37		0.86
Al_2O_3	13.46	13.17	13.3				15.74	1.7	0.49
SiO_2	28.39	27.91	29.48	0.75	0.63	0.16	38.14	3.78	4.94
P_2O_5	5.25	5.85	7	39.4	39.7	40.57	1.87	32.45	25.65
Cl				0.12	0.17	0.12			
CaO	18.06	20.12	19.04	57.32	56.94	56.73	12.86	10.9	8.92
Fe_2O_3	14.22	13.76	12.72				11.85	0.32	12.6
La_2O_3	5.88	4.91	4.83				4.36	16.99	13.36
Ce_2O_3	11.01	10.54	8.52				8.66	28.13	25.92
Nd_2O_3	3.33	3.21	2.62				2.55	5.38	7.25
Total	100	99.99	100	100	100.01	99.99	100		
Mineral	Monazite	Monazite	Monazite	Apatite	Apatite	Apatite	Monazite		

1–7, REE minerals in charnockites, 8–9 REE in syenites.

Table 2: *Trace and rare elemental concentration in syenites and charnockites in selected locations in southwestern Nigeria (all values in ppm)*

	1	2	3	4	5	6	7	8	9	10
Ba	2495	1565	1493	1754	1429	1942	1915	1467	1144	2018
Ga	20.3	19.8	20.1	18.4	20	18.7	19	19.8	19	22.6
Hf	24.5	15.7	11.6	10.2	11.6	5.6	5.6	7.4	12.1	20.6
Nb	31.3	30.4	27.3	22.9	27.9	13	12.9	12.2	24.7	39.3
Rb	384	366.9	263.5	315.7	296	93.4	86	69.8	78.6	105.4
Sr	842	438.1	463.9	455.1	464.1	1062	1028	535.7	465.6	399.3
Th	79.6	60.7	30.8	36.1	45.7	7.6	6	16.6	9	16.4
U	5.9	4.8	4.9	3.9	3.4	1.5	1.1	2.2	1.6	0.8
V	90	60	76	51	64	88	85	59	88	116
W	0.7	1.8	2.2	1.7	1.1	0.9	0.7	<0.5	<0.5	0.8
Zr	1063	597	461	3867	441.6	223.6	220	301.5	531.3	895
Y	28	24.9	26.8	22	32.2	17	15.9	11	26.1	64.1
La	141	111.4	93.6	81.7	106.7	51.4	50.8	70.2	72.1	195.6
Ce	290	212.4	178.5	150.2	200.7	96.1	93.3	109.6	137.1	338.4
Pr	39	24.35	23.08	18.32	25.87	11.97	11.66	11.81	17.45	41.96
Nd	149	81.1	83.6	63.5	93.4	42.9	42.7	37.7	62.6	150.7
Sm	24	12.04	13.54	9.75	15.15	6.77	6.64	4.81	10	23.06
Eu	4.58	2.37	2.57	2.19	2.67	2.12	2.11	2.49	2.86	4.31
Gd	14	7.73	8.96	6.85	10.29	5.1	4.82	3.46	7.94	18.72
Tb	1.44	0.97	1.11	0.83	1.24	0.64	0.6	0.42	1.03	2.39
Dy	6.02	4.72	5.31	4.2	6.02	3.2	3.19	2.05	5.07	12.51
Ho	0.88	0.83	0.94	0.73	1.06	0.6	0.56	0.37	0.93	2.23
Er	2.21	2.11	2.4	1.89	2.85	1.63	1.54	1.08	2.49	5.73
Tm	0.32	0.32	0.33	0.28	0.41	0.22	0.22	0.14	0.33	0.77
Yb	1.95	2.03	2.12	1.82	2.45	1.4	1.35	0.98	1.99	4.64
Lu	0.28	0.32	0.31	0.28	0.36	0.21	0.2	0.14	0.31	0.71
Y	28	24.9	26.8	22	32.2	17	15.9	11	26.1	64.1
ΣLREE	648	443.66	394.89	325.66	444.49	211	207	236	302.11	754.03
ΣHREE	26	19.03	21.48	16.88	24.68	13	12.48	8.64	20.09	47.7
ΣREE	675	462.69	416.37	342.54	469.17	224	220	245	322	802
ΣLREE/ ΣHREE	24	23.31	18.38	19.29	18.01	16.26	16.6	27.39	15.1	18.81
ΣREE+Y	703	487.59	443.17	364.54	501.37	241.26	235.59	256.25	348.3	865.83
Eu/Eu*	0.77	0.75	0.71	0.82	0.65	1.1	1.14	1.87	0.98	0.63
Ce/Ce*	0.94	0.98	0.92	0.93	0.92	0.93	0.92	0.92	0.93	0.9
$(La/Yb)_N$	48	37	29.77	30.26	29.36	24.75	25.37	48.29	24.43	28.42
$(La/Sm)_N$	3.66	5.82	4.35	5.27	4.43	4.78	4.81	9.18	4.54	5.34
$(Ce/Yb)_N$	38	27.06	21.78	21.35	21.19	17.76	17.88	28.93	17.82	18.86

Syenites: 1-1wo, 2-Iwere-Ile, 3 - Okeho, 4 - Ayetoro Oke, 5 - Kajola.

Charnockites: 6 - Otun. 7, Ado, 8 – Afao, 9 - Kajola, 10-Akure

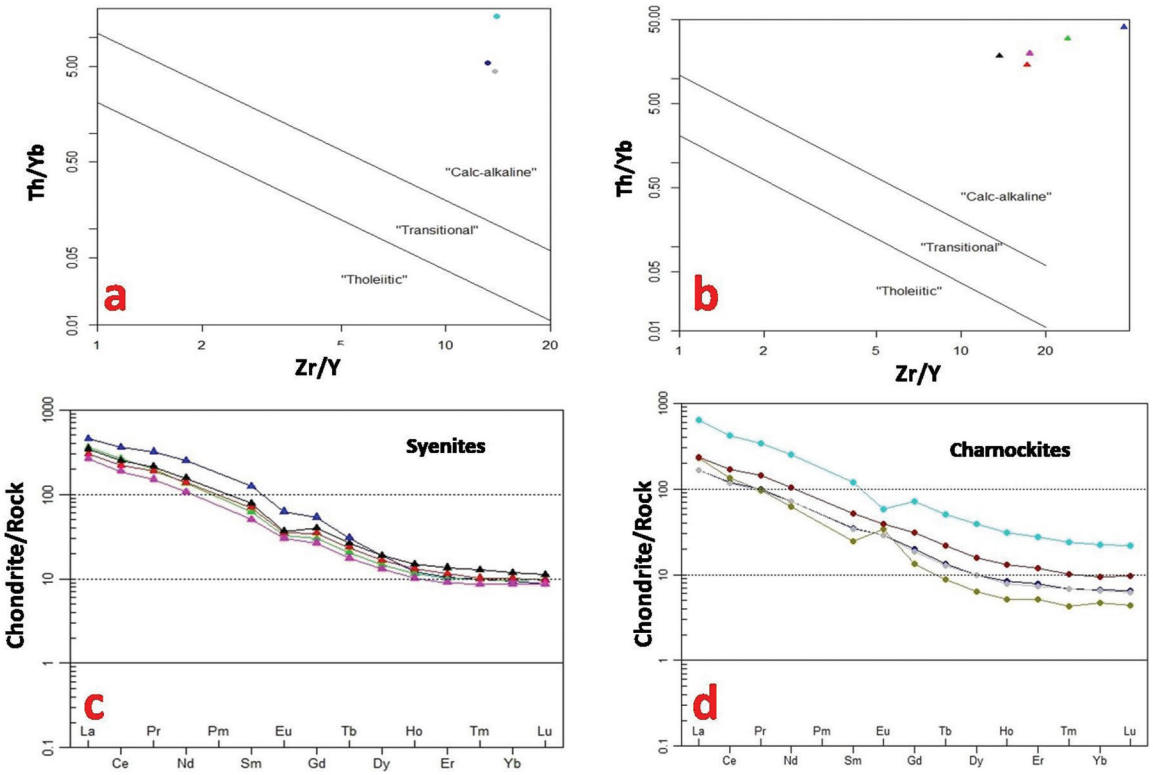

Figure 5: *a) Plots of Zr/Y vs Th/Yb for charnockites of the study areas showing three sampling points (after Ross and Bédard [14]; b) Plots of Zr/Y vs Th/Yb for syenites of the study area (after Ross and Bédard [14]); c) Chondrite normalised REE distribution pattern for the syenites (after Boynton [13]); d) Chondrite normalised REE distribution pattern for the charnockites (after Boynton [13]).*

The $(La/Yb)_N$ values ranged from 29.36 to 48.75 for the syenites and from 24.43 to 48.29 for the charnockites; the $(La/Sm)_N$ values in syenites is 4.35 : 5.82; and 4.54 : 9.18 in the charnockites. The $(Ce/Yb)_N$ ranges from 21.19 to 38.49 for the syenites, and from 17.76 to 28.93 for the charnockites. The high values of the normalised ratios of La to Yb, La to Sm, and Ce to Yb in the different rock types are evidence of a high degree of fractionation, which shows that the REE patterns are LREE enriched.

According to Ukaegbu and Ekwueme [9], the La/Yb, Ce/Yb, and La/Sm values are normally higher in residual products than in primary melts. Hence, $(La/Yb)_N$ values higher than 5 are an indication of magmatic differentiation [10]. This implies that even though the magma might have originated from a mixed source, differentiation was important in the formation of these rocks [8].

The syenites showed negative Eu anomalies of 0.65–0.82, suggesting that a large amount of plagioclase was removed from felsic magma during fractional crystallisation. It could also be due to the presence of pyroxenes in them, as pyroxene-rich cumulates acquire a negative Eu anomaly [11]. The charnockitic rocks showed both a negative and a positive Eu anomaly of 0.63–1.87, indicating accumulation of plagioclase during the fractionation of magma for the later (Figure 5). According to Weill and Drake [12], magma crystallising stable plagioclase has most of the Eu being incorporated into the plagioclase mineral leading to a higher concentration of Eu in the mineral relative to other rare earth elements in the magma.

The Ce anomaly ranges from 0.92 to 0.98 in the syenites, and from 0.90 to 0.93 in the charnockitic rocks. Ce anomalies reflect the oxygen fugacity in the environment of formation, [13]. According to Boynton [13], when there is no large negative Ce anomaly, it indicates formation under reducing conditions; a large negative Ce anomaly indicates formation under oxidising conditions.

Table 3: *Comparison of the REE concentration in the syenites of the study area with other related rock types (all values in ppm).*

	1	2	3	4	5	6
REE	RANGE	AVERAGE	AVERAGE	Mean	RANGE	AVERAGE
La	81.72–111.4	257	93.36	42.07	5082–94810	449.5
Ce	150.2–290.2	450	214.36	60.57	7021–90630	798
Pr	18.32–39.02	N/A	N/A	5.01	510–5835	75.5
Nd	63.5–149.2	304	105.51	13.04	1592–16418	43.5
Sm	9.75–24.25	66.5	16.72	1.18	110–1147	265.5
Eu	2.19–2.67	7.1	3.69	0.36	22.8–236.5	39
Gd	7.73–10.29	54.8	9.43	1.9	53–513	1.9
Tb	0.83–1.44	6	N/A	0.28	26–52	26
Dy	4.2–6.02	N/A	5.2	1.77	29–338	2.9
Ho	0.73–1.06	N/A	0.98	0.47	23–40	12.5
Er	1.89–2.85	N/A	2.31	1.56	36–395	2.35
Tm	0.28–0.41	N/A	N/A	0.15	6–7	5.95
Yb	1.82–2.45	14.4	1.51	1.61	3–52	0.85
Lu	0.28–0.36	2.55	0.21	0.29	0.5–10	0.8
ΣLREE	325.66–648.24	1084.6	433.64	122.23	N/A	1655.4
ΣHREE	16.88–26.91	77.75	19.64	8.03	N/A	29.89
REE	342.54–674.85	1162.35	453.28	130.26	14458–199154	1685.3
ΣLREE/ΣHREE	18.01–24.11	13.95	22.07	15.22	N/A	55.38

1. Syenites of the study areas
2. Syenites of Nigeria Mesozoic granites [15]
3. Syenites of Minias Grais, Brazil [16]
4. Nepheline syenites of Gboko area, Nigeria [17]
5. Carbonatites from Wu dyke, Bayan Obo, North China [18]
6. Quartz syenites of Prakasam alkaline province, India [19]

REE mineralisation potential in the syenites and charnockites

In order to determine the mineralisation potential of the syenites and charnockites, the REE-bearing minerals in the rocks were searched for, the mineral apatite and monazite were observed, and a comparative study was carried out comparing between the syenites of this present study with related rocks, which includes the following: the nepheline syenites of the Gboko area, with ∑REE = 130.26 ppm; quartz syenites of the Prakasam alkaline province of India ∑REE = 1685.3 ppm; the quartz syenites from the Nigerian younger granites province ∑REE =1084.6 ppm; and the syenites of Capituva Massif, Brazil ∑REE = 453.28 ppm in order to determine the abundance of ∑REE in the study area syenites relative to those of other areas, (Table 3).

Charnockitic rocks of the study area were compared with related rock types to determine their ∑REE abundance relative to those of the related rock types. The comparison was done with Charnockites/enderbites of the Obudu Plateau; Garnet-charnockitic gneiss of Congo; charnockites from Kogi, Nigeria; charnockite gneiss from Norway; and charnockites from Pallavaram, Madras city, India (Table 4). The abundance of REE in the syenites and charnockites, when compared to concentrations from regions where REE has been studied and shown to be substantially enriched, suggests that the syenites are fairly enriched, while the charnockites are moderately enriched.

Further comparison was done for both the syenites and the charnockitic rocks with carbonatites from Wu dyke, Bayan Obo, North China, an area where REE is mined. The REE

Table 4: *Comparison of the REE concentration in the charnockites of the study area with other related rock types (all values in ppm).*

	1	2	3	4	5	6
REE	RANGE	RANGE	AVERAGE	AVERAGE	AVERAGE	RANGE
La	50.8–195.6	40.9–147	280.38	136	80.5	20.7–81.7
Ce	93.3–338.4	85.3–287	26.24	301	182.5	28.0–159.0
Pr	11.66–41.96	10.4–31.9	85.5	35.3	N/A	N/A
Nd	37.7–150.7	46.9–123	13.62	146	95.5	6.9–66.0
Sm	4.81–23.06	9.7–20.3	4.33	26	20	0.76–15.9
Eu	2.11–4.31	2.35–3.85	12.55	5.8	2.5	1.23–3.17
Gd	3.46–18.72	8.2–15.1	1.95	17.7	18.5	6.0–19.4
Tb	0.42–2.39	1.2–1.8	12.28	2.4	2.95	0.08–0.78
Dy	2.05–12.51	5.9–9.2	2.41	12.6	N/A	N/A
Ho	0.37–2.23	1.1–1.6	6.65	2.2	N/A	N/A
Er	1.08–5.73	3.1–4.2	0.97	5.7	N/A	N/A
Tm	0.22–0.77	0.43–0.54	6.47	0.75	1.445	0.03–2.25
Yb	0.98–4.64	2.6–3.2	0.95	4.2	8.2	0.27–13.8
Lu	0.14–0.71	0.37–0.51	30	0.63	1.13	0.21–1.91
ΣLREE	211.26–754.03	196.7–611	422	650.1	381	57.59–325.77
ΣHREE	8.64–47.7	25.9–36.3	61.7	46.18	32.23	6.59–38.14
ΣREE	219.69–801.73	220.02–647.96	484	696.28	413.23	64.18–363.91

N/A - Not Available

1. Charnockite of the study area
2. Charnockites of Obudu Plateau [20]
3. Garnet-charnockitic gneiss of Congo, South Cameroon [21]
4. Charnockites from Kogi area, Nigeria [22]
5. Charnockites gneiss from South Norway [23]
6. Charnockites from Pallavaram, Madras City, India [24]

concentration in the rocks of the study areas had very low ∑REE relative to the very high REE contents of this rock and are therefore not be economically viable.

Conclusion

The SEM studies of discrete phases of the charnockites revealed the possible presence of REE-bearing minerals, apatite, and monazite, while studies of syenites revealed a possible presence of monazite. The abundance of REEs in the syenites and charnockites, when compared to concentrations from regions where REEs have been studied and shown to be substantially enriched, suggests that the syenites are fairly enriched, while the charnockites are moderately enriched.

References

[1] Long, K., Gosen, B., Foley, N., Cordier, D. (2010): The principal rare Earth Elements Deposits of the United States: A summary of domestic deposits and a global perspective. *U.S. Geological Survey Scientific Investigations Report* 2010–5220, 96 p.

[2] Dostal, J. (2017): Rare earth element deposits of alkaline igneous rocks. *Resources*, 6(34), pp. 1–2, DOI:10.3390/resources6030034.

[3] Omotunde, V.B., Olatunji, A.S., Abdus-Salam, M.O. (2020): Rare earth elements assessment in the granitoids of part of Southwestern Nigeria. *European*

Journal of Environment and Earth Sciences, 1(5), pp. 1–10.

[4] Rahaman, M.A. (1976): Review of the Basement Geology of Southwestern Nigeria. In: *Geology of Nigeria*, Kogbe, C.A. (ed.). Elizabethan Publ. Co.: Lagos, pp. 41–48.

[5] Nigerian Geological Survey Agency (2004): Geological map of Nigeria, scale 1:2,000,000. *Geological Survey of Nigeria,* Abuja.

[6] Nyakairu, G.W.A., Koeberl, C. (2001): Mineralogical and chemical composition and distribution of rare earth elements in clay-rich sediments from Central Uganda. *Geochemistry Journal,* 35, pp. 13–28.

[7] Roy, P.D., Smykatz-Kloss, W. (2007): REE geochemistry of the recent playa sediments from the Thar Desert, India: an implication to playa sediment provenance. *Chemie der Erde -Geocheistry,* 67, pp. 55–68.

[8] Oyinloye, A.O., Obasi, R. (2006): Geology, geochemistry and geotectonic setting of the Pan-African granites and charnockites around Ado-Ekiti, southwestern Nigeri. *Pakistan Journal of Scientific and Industrial Research,* 49(5), pp. 299–308.

[9] Ukaegbu, V.U., Ekwueme, B.N. (2005): Petrogenetic significance of rare earth element behavior in the basement rocks of southern Obudu Plateau, Bamenda Massif, southeastern Nigeria. *Chinese Journal of Geochemistry,* 24, pp. 129–135.

[10] Feng, R., Kerrich, R. (1990): Geochemistry of fine-grained clastic sediments in the Archean Abitibi greenstone belt, Canada: Implications for provenance and tectonic setting. *Geochimica et Cosmochimica Acta,* 54(4), pp. 1061–1081.

[11] Papike, J.J., Shearer, C.K., Simon, S.B., Shimizu, N. (1988): Lunar pyroxenes: Crystal chemical rationalization of REE zoning, pattern, and shapes and abundances—an ion microprobe investigation. *Abstracts of the Lunar and Planetary Science Conference,* 19, pp. 901–902.

[12] Weill, D.F., Drake, M.J. (1973): Europium anomaly in plagioclase feldspar: Experimental results and quantitative model, *Science*, 180(4090), 1059–1060, DOI:10.1126/science.180.4090.1059.

[13] Boynton, W.V. (1984): Cosmochemistry of the rare earth elements: Meteorite studies. In: *Rare Earth Element Geochemistry*, Henderson P. (ed.). Elsevier: New York, pp. 63–114, DOI:10.1016/B978-0-444-42148-7.50008-3.

[14] Ross, P.S., Bédard J.H. (2009): Magmatic affinity of modern and ancient subalkaline volcanic rocks determined from trace-element discriminant diagrams. *Canadian Journal of Earth Sciences,* 46(11), pp. 823–839, DOI:10.1139/E09-054.

[15] Bowden, P., Bennett, J.N., Whitley, J.E., Moyes, A.B. (1979): Rare earths in Nigerian mesozoic granites and related rock. *Physics and Chemistry of the Earth*, 11, pp. 479–491, DOI:10.1016/0079-1946(79)90045-4.

[16] Valdecir, J. (1993): Petrogenesis and tectonic setting of the Neoproterozoic Capituva k-syenitic massif, SW Minas Gerais, Brazil. *Revista Brasileira de Geociencias*, 23, pp. 129–138.

[17] Najime, T., Abaa, S.I., Magaji, S. (2012): Petrology and rare earth elements (REE) distribution patterns of magmatic rocks in Gboko Area, Lower Benue Trough Nigeria: implication for tectonic evolution. *Global Journal of Geological Sciences,* 10(1), pp. 47–58.

[18] Yang, X., Yang, X.Y., Zheng, Y., Le Bas, M. (2003): A rare earth element-rich carbonatite dyke at Bayan Obo, Inner Mongolia, North China. *Mineralogy and Petrology,* 78, pp. 93–110.

[19] Sridhar, N., Mallikarjuna, R., Reddy, Nagendrababu, G. (2018): Quartz syenites from the Prakasam alkaline province, Southern India; A comparative study with special emphasis on their rare earth element contents. *Journal of India Geophysical Union,* 22(5), pp. 507–517.

[20] Ukaegbu, V.U., Beka, F.T. (2007): Petrochemistry and geotectonic significance of enderbite-charnockite association in the Pan-African Obudu plateau, southeastern Nigeria. *Journal of Mining and Geology,* 43(1), pp. 1–14.

[21] Mbongue, N.J.L., Ngnotue, T., Nlend, N., Suh, C.E. (2014): Origin and evolution of the formation of the Cameroon Nyong series in the western border of the Congo Craton. *Journal of Geosciences and Geomatics,* 2(2), pp. 62–75.

[22] Oroh, S. (2018): *Geochemical and petrogenetic study of the charnockitic rocks of Akure and Ekiti areas, southwestern, Nigeria.* M. Sc. Thesis. University of Ibadan, Department of Geology, 128 p.

[23] Field, D., Drury, S.A., Cooper, D.C. (1980): Rare-earth and LIL element fractionation in high grade charnockitic gneisses, south Norway, *Lithos,* 13(3), pp. 281–289.

[24] Weaver, Barry L. (1980): Rare earth elements geochemistry of Madras granulites. *Contributions to Mineralogy and Petrology*, 71(3), pp. 271–279.

Original Scientific Article • DOI: 10.2478/rmzmag-2021-0017

Received: April 17, 2022
Accepted: June 03, 2022

Solid Mineral Potential and Geothermal Energy Reserve of Northern Basement Complex, Nigeria

Možna prisotnost rude in geotermalna energija v Severnem bazalnem kompleksu, Nigerija

Okechukwu Stephen Ifeanyi*, Opara Alexander Ifeanyichukwu, Chikezie Peter Chidozie, Akaolisa Chukwuemeka Casmir, Okoli Austin Emeka, Agoha Chidebere Charles
Department of Geology, Federal University of Technology, Owerri, Nigeria
*Corresponding author: E-mail: stephen.okechukwu@futo.edu.ng

Abstract in English

The spectral analysis of aeromagnetic data over the study area (Northern basement complex, Nigeria) revealed the existence of two major source depths. The second segment of the spectrum layer shows shallow sources ranging in depth from 0.135 km to 0.201 km, with an average depth of 0.140 km. The depth to the basement or deeper source ranges between 1.655 km and 2.021 km, with an average depth of 1.882 km. The Precambrian basement is reflected in the deeper sources, beginning with the first segment of the power spectrum. Structural and topographic relief of the basement surface, lateral differences in basement susceptibilities, and intra-basement features such as faults and fractures contribute to the variation in basement composition. The mean thickness of sediments in the study area is represented by the D2 values obtained from the spectral plots. The depths revealed by this study appears to be reasonable and consistent with previous researchers' findings. Tectonically active regions have a major impact on heat flows. The average heat flow in thermally normal continental regions is reported to be above 60 mW/m^2. Values between 80 and 100 mW/m^2 indicate a good geothermal source; values in excess of about 80–100 mW/m^2 indicate anomalous geothermal conditions.

Keywords: 3-D Euler deconvolution, spectral inversion, magnetic basement depth, linear features, Nigeria

Povzetek

Spektralna analiza aeromagnetnih podatkov je na preiskanem območju razkrila obstoj virov v dveh glavnih globinah. Drugi segment spektralnega sloja kaže na plitve vire, ki ležijo na globini od 0,135 km do 0,201 km, s povprečno globino 0,140 km. Globina do podlage ali globljega vira je med 1,655 km in 2,021 km, s povprečno globino 1,882 km. Predkambrijska podlaga se odraža v globljem viru s prvim segmentom spektra moči. Strukturni in topografski relief površine predkambrijske podlage, lateralne razlike v susceptibilnosti podlage in njene notranje strukture, kot so prelomi in razpoke, prispevajo k razlikam v sestavi podlage. Srednjo debelino sedimentov predstavljajo D2 vrednosti, pridobljene iz spektralnih diagramov. Ocene globin na podlagi te raziskave so realistične in v skladu s predhodnimi ugotovitvami. Tektonsko aktivna območja imajo bistven vpliv na toplotni tok. Medtem ko je povprečni toplotni tok termično normalnih delov kontinentalne skorje nad 60 mW/m^2, vrednosti med 80 in 100 mW/m^2 predstavljajo dobre geotermalne vire, še višje vrednosti pa anomalne geotermalne pogoje.

Ključne besede: 3-D Eulerjeva dekonvolucija, spektralna inverzija, globina magnetne podlage, linearne strukture, Nigerija

Introduction

The Nigerian basement comprises the revitalized zone formed by plate collision between the West African craton's passive continental margin and the active continental margin [1]. The basement rocks are thought to be the consequence of at least four significant orogenic deformation processes.

The primary goal of the aeromagnetic survey is to identify minerals or rocks with peculiar magnetic characteristics that manifest themselves by producing anomalies in the strength of the earth's magnetic field [2]. The aeromagnetic survey is used to map abnormalities in the earth's magnetic field, which are connected to the subsurface geological structure. Faults are typically shown by magnetic anomalies as sudden shifts or close spacing in the orientation of the outlines. The premise of an aeromagnetic survey is similar to that of a magnetic survey conducted using a handheld magnetometer, but it enables far wider portions of the earth's surface to be covered swiftly for regional reconnaissance [3]. As the aircraft flies, the magnetometer registers slight variations in the intensity of the ambient magnetic field, which are due to both temporal impacts of the constantly shifting solar radiation and the geographic layout in the earth's magnetic field, the latter due to both the regional magnetic field and the local influence of magnetic minerals within earth's crust [4]. After removing solar and regional impacts, the subsequent aeromagnetic map depicts the global distribution and relative abundance of magnetic elements in the upper crust. Aeromagnetic methods may successfully map hidden and poorly exposed faults in a basin context. The magnetic basement is a group of rocks that reside under sedimentary basins and occasionally outcrop [5]. Linear features on aeromagnetic maps are plainly visible and often depict the form and position of particular folds, faults, joints, veins, lithologic contacts, and other geologic structures that may lead to the finding of specific mineral deposits [6]. They typically depict the general geometry of an area's underlying structures, resulting in a regional structural pattern. Certain lineament patterns have been identified as the most beneficial structural elements for mineral deposit management. The analysis of variations in a region's Curie isotherm can provide useful information about the regional temperature profile at depth and the composition of surficial geothermal energy [7]. A geothermal energy-rich area is defined by an extremely large temperature gradient and heat movement, based on measurements. As a result, geothermically active sites are expected to have shallow Curie point depths [8]. It is also generally recognized that the bulk of the geodynamic processes visible on the surface are directly influenced by the temperature within the earth [9]. Heat flow measurements in various sections of the African continent have indicated that the mechanical structure of the African lithosphere is diverse in this regard [8]. Magnetic anomalies are investigated in order to calculate the depths to the bottoms of magnetized entities in the crust.

Several geologic formations and stratigraphic strata have been identified and recognized as a result of research on the northern basement complex. The current study has used high-resolution aeromagnetic data to analyze the structures that exist in the northern basement complex. The goal of this research is to employ various methods in the geological interpretation of the section of the basement complex from which data was collected and to use the data to estimate the Curie point depth, heat flow, and geothermal gradient of the region. The aim of this study is to interpret geological features of part of northern basement complex and to infer its solid mineral potential as well as its geothermal energy reserve.

Location and Geology of Study Area

The study area, which covers part of the Northern basement complex, lies between latitudes 9°00′N and 10°00′N and longitudes 7°30′E and 8°30′E (Figure 1). The study area is enclosed within four (4) aeromagnetic maps of the Geological Survey of Nigeria.

The area is well drained by streams and rivers, the sources for most of which are found in the surrounding hills. The drainage system in the area generally flows either northwards or westwards into the Kaduna and Gurara rivers,

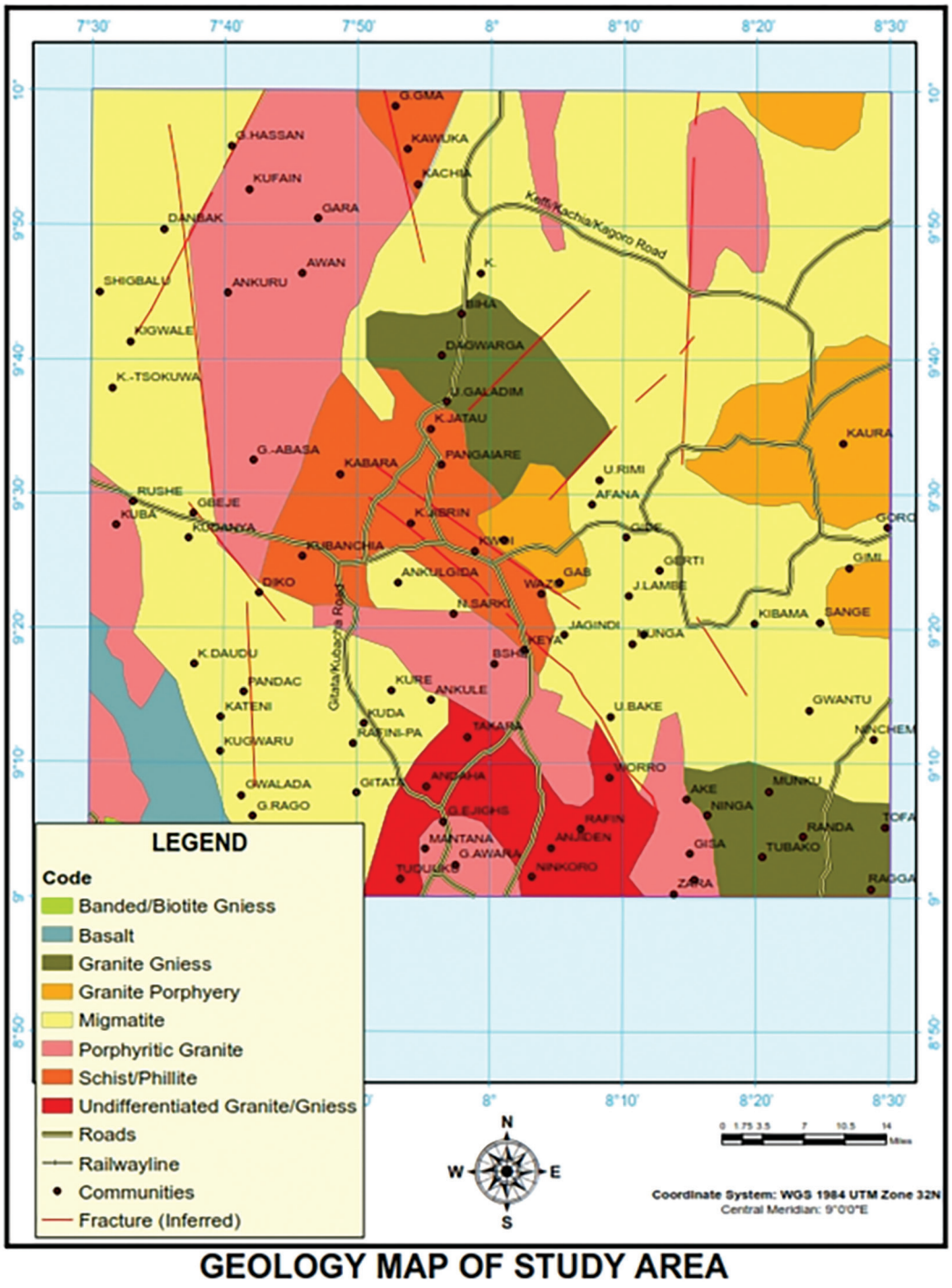

Figure 1: *Geologic map of the study area.*

which form part of the Niger basin, or southwards into the Mada River, which belongs to the Benue basin. The Farman range of hills forms the divide between the Gurara and Mada drainages. The Mada is represented by the Kogum River. The rivers and most of the smaller streams are perennial.

The relief of the area comprises the lowland and upland areas. The lowland is represented by the Kafanchan plain, which comprises the towns of Kafanchan, Matsirga, Madakia, Katsit, Garaje Kagoro, Tum, Fadan Daji, and Zakwa [10]. These areas have ground surface elevations above the mean sea level range of

between 594 m and 777 m. Examples of granitic rock are found in the Farman ranges, the Zuturung hill, Yariye Mutumbu Hill, Gatum Hill, and the Madauchi Hill [11]. The height of these hills above mean sea level ranged between 762 m and 996.70 m.

The Nigerian basement complex evolution took place over at least four orogenic cycles: the Liberian (2800 ± 200 Ma), the Eburnian (200 ± 200 Ma), the Kibaran (1100 ± 200 Ma), and the Pan-African (600 ± 150) Ma). The Pan-African orogeny is the most significant orogeny in Nigeria, its imprint being ubiquitous [12, 13]. The rocks in this zone (the Pan-African mobile belt) have witnessed a period of remobilization and reactivation that took place during the Pan-African thermo-tectonic event some 600 Ma ago. The study area's regional metamorphism, tectonism, and magmatism resulted in the formation of cracks and faults, and the deployment of intrusive and dyke-like structures [14].

Methods

Data source

The aeromagnetic maps used for the study were obtained from the Geological Survey of Nigeria. Four digitized aeromagnetic maps covering the study area were acquired, digitized, and interpreted (Figures 2 and 3). This map was part of the nationwide aeromagnetic survey carried out by Fugro Airborne Surveys in 2009 and was sponsored by the Geological Survey Agency of Nigeria. The survey was carried out at 500-m line spacing in NW-SE orientation and 80-m mean nominal terrain clearance flying altitude above the terrain was 500 feet (approximately 152 m) with 5-km control line spacing in the NE-SW orientation. The survey also used measured horizontal gradients and gradient-enhanced gridding. The regional correction of the magnetic data was based on the International Geomagnetic Reference Field (IGRF, Epoch date 1 January 1974). In order to obtain the actual total field magnetic data, 32,000 gammas should be added to the contour values. Out of this, 25,000 gammas represent the regional field while 7000 gammas are arbitrarily removed from the contour values.

Aeromagnetic data analysis

Numerous analytical techniques and procedures are used to examine aeromagnetic data. Among them are aeromagnetic data

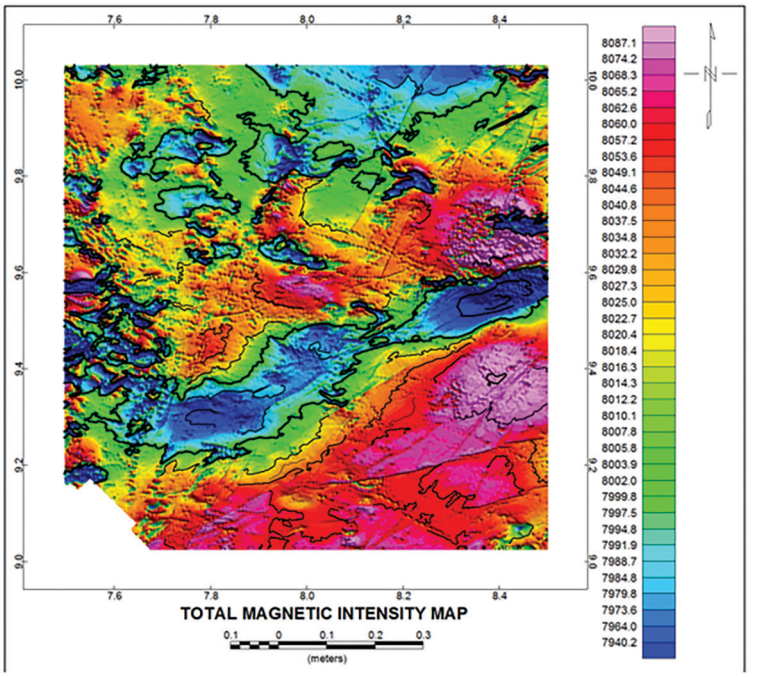

Figure 2: *Aeromagnetic field over the study area as a color-shaded, contoured map.*

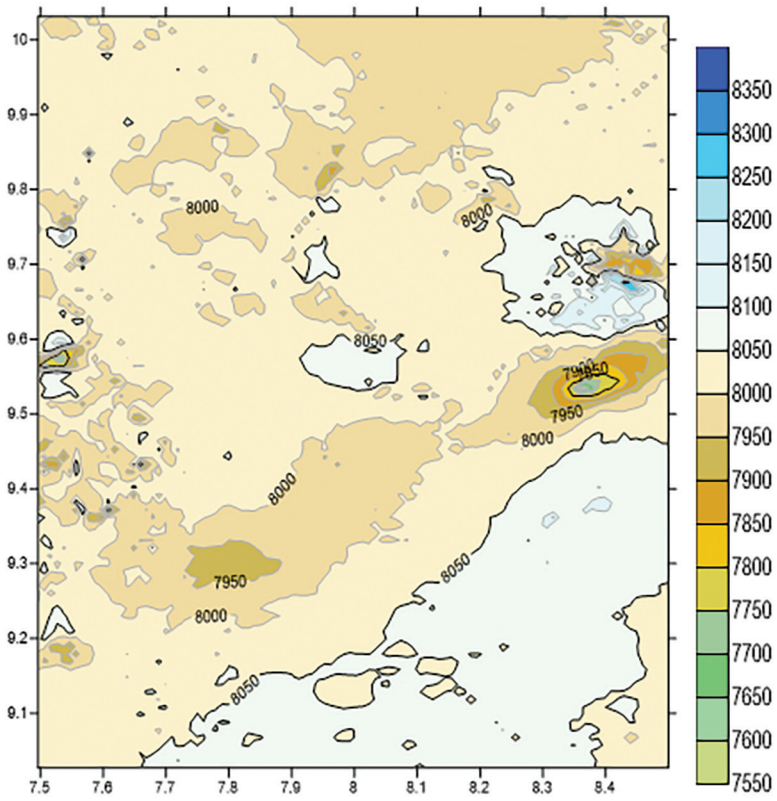

Figure 3: *Color-coded pixel contour map of the total magnetic field of the study area in gammas.*

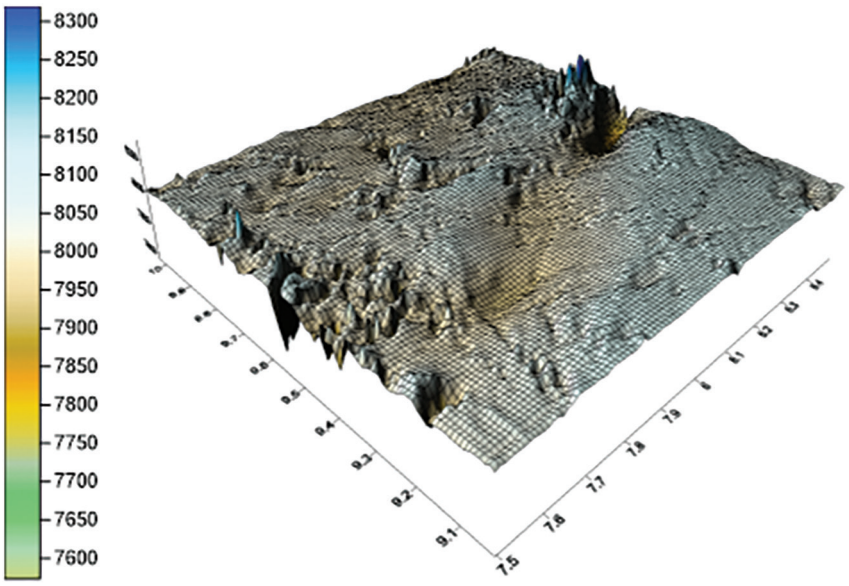

Figure 4: *3-D surface map of the total magnetic field of the study area in gammas.*

filtering and convolution, reduction to pole, regional-residual separation, and depth estimate analysis (Figure 4). These tactics are thoroughly examined for improved clarity. The major purpose of aeromagnetic data processing is to systematically differentiate between local and regional magnetic anomalies and to ameliorate these anomalies.

Aeromagnetic filters

Because not every signal in geophysical research is of interest, filtration methods are always required. Short-wavelength disturbance is often produced by near-surface or shallow, anomalous sources.

A low-pass filter is just a band-pass filter with a very big long-wavelength cutoff. A low-pass filter is called linear because it treats all data identically. When attempting to eliminate short-wavelength but high-amplitude characteristics, this might be an issue because relatively powerful filters may be necessary. Such filters have the potential to impact areas of the data that you did not plan to affect. A nonlinear filter, such as NLFILT, is another option.

A high-pass filter sharpens incoming data by using a convolution filter. This filter is referred to as a 'high-pass' filter because it enables high wave numbers (high frequencies) to pass through to the output channel. Longer-than-the-long wavelength cutoff features in the data will be deleted. Fraser's 1966 approach is used to create the convolution filter. The filter length can be supplied or computed by default. The default length will be established by subtracting the length of the longest wavelength. A band-pass filter is called linear because it treats all data equally. When attempting to eliminate short-wavelength but high-amplitude characteristics, this might be an issue because relatively powerful filters may be necessary. Such filters have the potential to impact areas of the data that you did not plan to affect. A nonlinear filter, such as NLFILT, is another option.

Nonlinear filters are extremely effective in removing high amplitude and short wavelength noise from data. A nonlinear filter can be followed by a linear low-pass filter to smooth out any low-amplitude noise that may remain. The decision process is based on the breadth and amplitude of characteristics in the data compared to a local backdrop. A feature must be smaller than a set width and have a bigger amplitude than a specified amplitude tolerance to be deemed noise.

Reduction to the pole and equator

The reduction to the pole (RTP) conversion compensates for the adjustment caused by the vector essence of the Earth's magnetic field in between locations of anomalies (closed highs or lows on a contour map) and their causes. Although the symmetric 'highs' are directly centered on the body, the highest gradient of the antisymmetric dipolar anomalies completely matches with the body edges.

The amplitude portion of reduction to the equator is the sin(I) term, and the phase aspect is the I cos(I) cos(D-q). North-south characteristics can blow up while lowering to the equator from low latitudes due to a quantitative error (from the term of 0/0) in amplitude correction (the sin(I) component) that is applied when (D-) is /2. (i.e., a magnetic east-west wavenumber). This complexity can be reduced or eliminated by choosing a larger latitude solely for amplitude correction, at the cost of substantially under-correcting the amplitudes of adjoining north-south features. Once the field has been decreased to the equator, the regional magnetic field will be horizontal, as will the majority of the source magnetizations.

Curie point depth, geothermal gradient, and heat flow

The Curie point depth is the depth at which the presence of magnetic mineral in the crust shifts from a ferromagnetic to a paramagnetic state, and its capacity to induce recognizable magnetic anomalies reduces as the temperature increases. It is also described as the moment at which some materials lose their permanent magnetic characteristics, allowing induced magnetism to take their place. Organized magnetic moments undergo ferromagnetic transformation and become chaotic paramagnetic [15]. The Curie point depth is calculated from aeromagnetic data as the basal depth of a magnetic source.

The upper limit and centroid of a magnetic layer are calculated using the slope of the power spectrum. The magnetic source's base depth is:

$$Z = 2Z_2 - Z_1 \tag{1}$$

where Z_2 is the centroid of the magnetic layer, and Z_1 is the top bound.

Heat flow estimations on the crust may thus be calculated using depth and thickness

data. The Curie point temperature at which rocks lose their ferromagnetic characteristics bridges the gap between thermal models and models based on magnetic source analyses [16].

Fourier's law is the fundamental relationship for conductive heat transmission. Under the premise that the temperature fluctuation is vertical and the temperature gradient $\left(\frac{\delta T}{\delta z}\right)$ is constant in one dimension, Fourier's law assumes the following form:

$$q = -k\frac{\delta T}{\delta z} \quad (2)$$

where, q is heat flow and k is thermal conductivity.

Curie temperature θ^0 can also be expressed as:

$$\theta = \left(\frac{\delta T}{\delta z}\right)d \quad (3)$$

where, d is the Curie-point depth (as obtained from the spectral magnetic analysis).

The surface temperature is 0°C, and $\frac{\delta T}{\delta z}$ will remain static if no heating systems or heat sinks exist between the earth's crust and the Curie-point depth. Magnetic mineralogy influences the Curie temperature.

Depth estimation by 3D Euler deconvolution

The standard 3D Euler method relies on Euler's homogeneity equation, which pertains to the potential field (magnetic or gravitational) and its gradient elements to the position of the causes via the extent of homogeneity N, which can be assumed to be a structural index. In addition to depth estimates, the method employs a structural index. On conventional maps, the Euler method observations are represented as point solutions that include the location (position of solution) and the depth (color range).

The located Euler 3D technique, which, unlike the standard Euler method, examines and restricts grid positions prior to actually computing depth estimations using Euler deconvolution, is another alternative for restricting the solutions discovered by the Euler method. The located Euler technique calculates the analytic signal (3p) and locates peaks in the grid of analytic signals. The standard depth assessment centered on Euler deconvolution is then implemented only to these peak spots. Nevertheless, since it generates far fewer solutions than the standard Euler method, it is only appropriate for overwhelmingly clear anomalies and does not form solution clusters.

$$ASig = \sqrt{(dx.dx)+(dy.dy)+(dz.dz)} \quad (4)$$

Results and Discussions

Total magnetic intensity map

Magnetic anomalies of both short and long wavelengths were interpreted within the study area. The total magnetic field intensity map produced by digitization is displayed as both a total field intensity map and a three-dimensional map.

The total magnetic intensity after digitization ranged from 7940.2 nT to 8087.1 nT, indicating a magnetic signature. The northern part of the study area is dominated by magnetic lows, indicating that the area has low magnetic concentration and thus lower susceptibility. Magnetic highs can be found in the study area's south-eastern corner. The existence of granitic rocks that intruded through both the crystalline basement and metasediment belts might explain the magnetic high of magnitude 8087.1 nT. When likened to the geological map of the study area, the total magnetic map in gamma has closures in the northeastern part of the area that conforms with the granite porphyry. These closures are lineament expressions.

The wireframe map of the total magnetic field of the study area has a lot of undulation with a lot of highs, which is an indicator of a magnetic high, as shown in the 3-D surface map of the total magnetic field of the study area in gammas. The magnetic highs are represented by the colors seen in the undulation. This indicates that there is a higher concentration of magnetically susceptible minerals.

The 3D aeromagnetic plot indicates that there is an undulating topography and are areas of magnetic low, relatively speaking. The 3-D relief map revealed two distinctive features:

areas of low relief (plains) and areas of high relief. The high-relief area is also believed to be more tectonically active than the low-relief area and as such contains mineral deposits.

Digital filtering

A high-pass filter sharpens the input data through the application of a convolution filter. A high-pass filter emphasizes short wavelengths and eliminates wavelengths larger than the cut-off wavelength. Figure 5a clearly shows clusters of positive and negative anomalies. These anomalies are found to be distributed with varying trends. The prominent anomalies in the southeastern part of the study area and the other anomalies were retained.

The low-pass filter is defined as a filter that passes long wavelengths and rejects all wavelengths smaller than the cut-off wavelength. The low-pass filtering process is used to isolate the regional features from the local ones. The anomaly map with a low-pass magnetic filter (Figure 5b) shows that the well-defined trends of anomalies in the aeromagnetic map still persist. A band-pass filter changes channel data such that features longer than the long-wavelength cutoff and shorter than the short-wavelength cutoff will be removed. A band-pass filter is considered linear because all data is treated by the filter equally (Figure 5c).

Nonlinear filters are very good for removing high amplitude and short wavelength

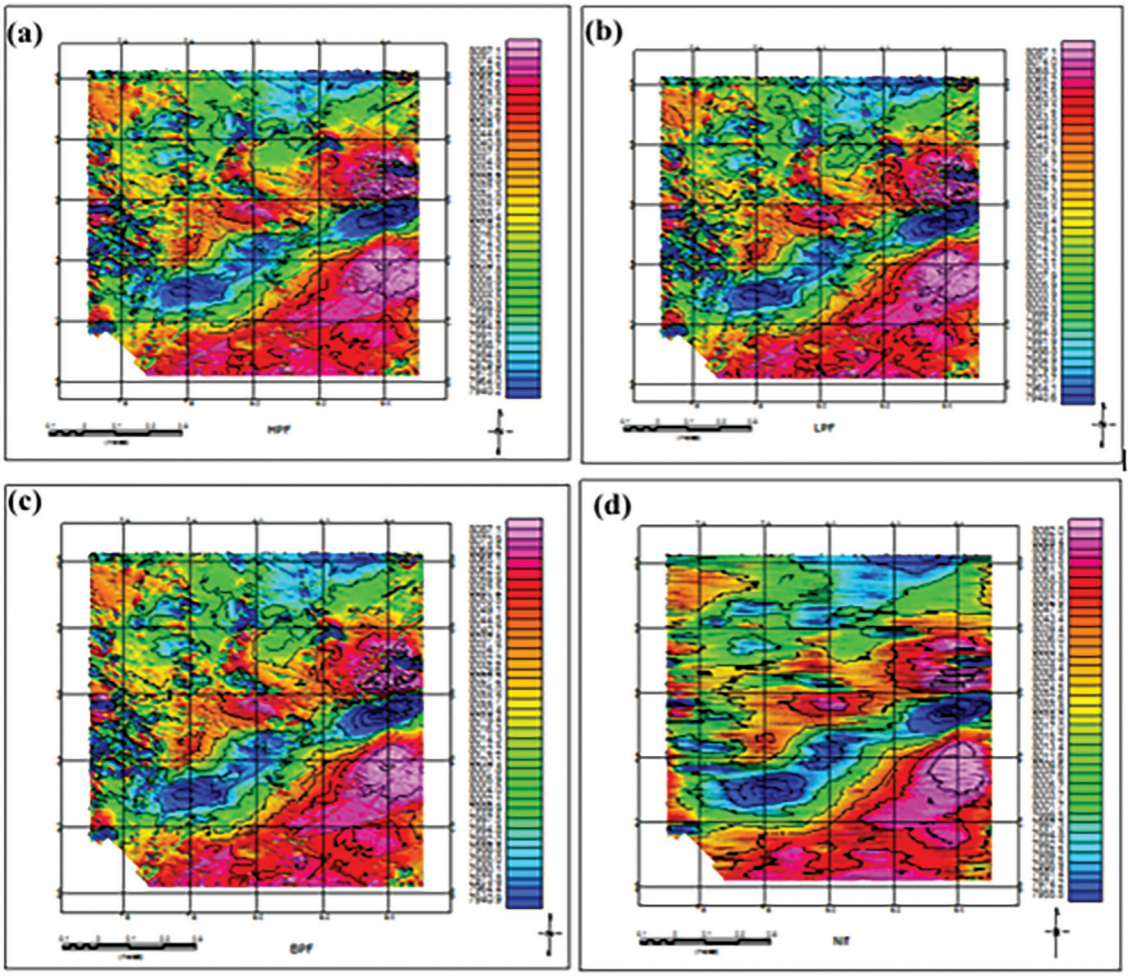

Figure 5: *(a) High-pass filter, (b)low-pass filter, (c) band-pass filter, (d) non-linear filter map of the total magnetic field intensity of the study area.*

noise from data. A nonlinear filter can be followed by a linear low-pass filter to smooth out any low-amplitude noise that may remain (Figure 5d).

Regional-residual separation

The regional gradients in the aeromagnetic data were removed using multi-regression least squares analysis to fit a plane surface to the data. The residual anomaly values are obtained by subtracting the regional field values from the observed data.

The residual magnetic intensity of the study ranges from -83.7 gammas to 70.2 gammas, as shown in Figures 6a-d. The study area is characterized by negative residual anomalies surrounded by positive residual anomalies, as shown by the figures. These negative anomalies, surrounded by an elongated positive anomaly, reflect a significant magnetization zone surrounded by a lower magnetization zone. The residual anomalies in Kafanchan and Jema'a are primarily positive, according to the first, second, third, and fourth residuals.

The negative residual anomalies correspond to a low magnetization zone, whereas the positive residual anomalies correspond to a high magnetization zone. Such negative anomalies, surrounded by an elongated positive anomaly, reflect a significant magnetization zone surrounded by a lower magnetization zone. Even so, the occurrence of the elongated positive anomaly in the study area might be credited to magmatic activity, which led to a high concentration of magnetic minerals in the majority of near-surface

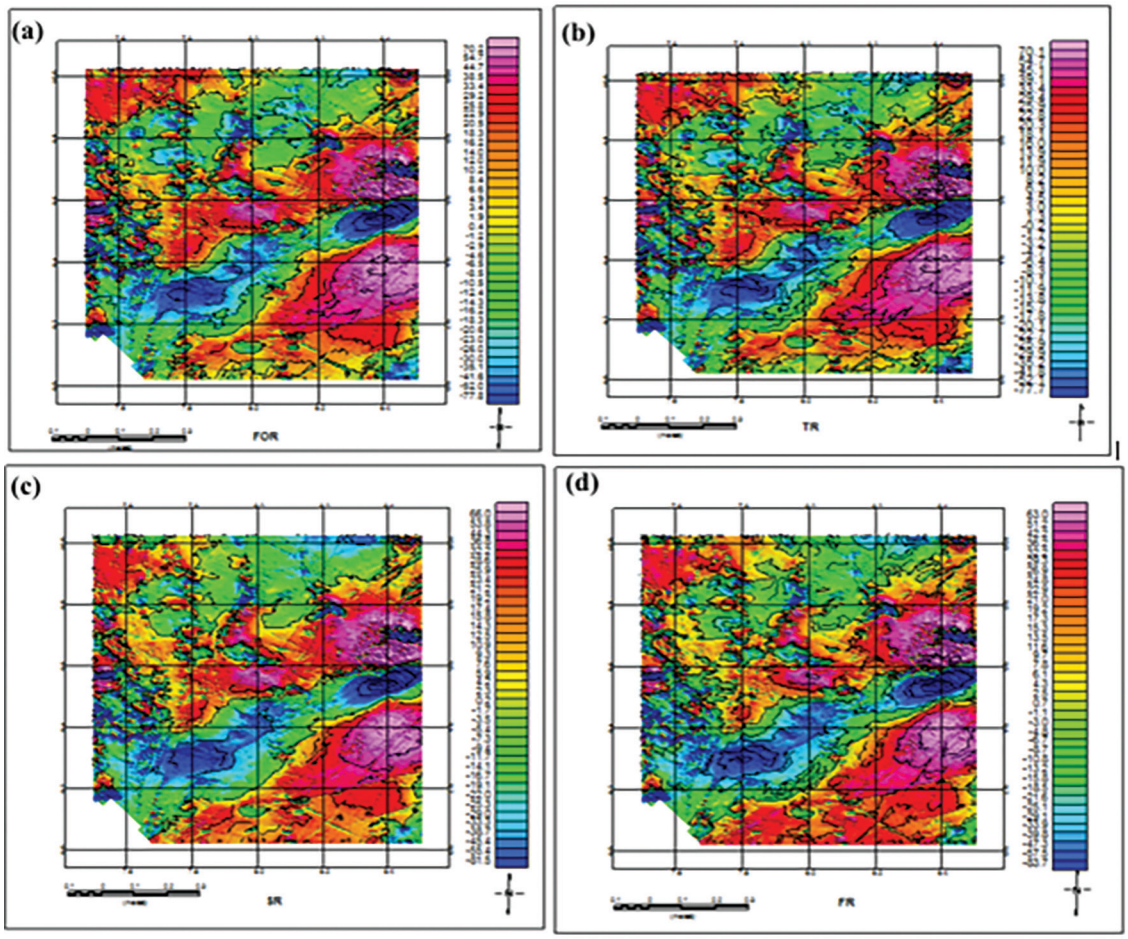

Figure 6: *(a) First-degree residual, (b) second-degree residual, (c) third-degree residual, (d) fourth-degree residual field over the study area as a color-shaded contour map.*

rocks. It should be noted that a strong magnetic anomaly in the vicinity of the study area might be influenced by mafic rocks.

The regional fields establish the major tectonic elements of a deeper and regional extent that affect and control the structural framework of the study area. First- to fourth-degree regional anomalies of the aeromagnetic data reveal a dominant regional trend of NE-SW trends and some E-W trends.

The structural trends suggested by the polynomial surfaces have trend directions of NE-SW, E-W, and NW-SE. The NE-SW trend is the dominant orientation in the study area, and it depicts the Pan-African orogeny. The fact that the structural trend is still dominant shows that there is little tectonic activity going on in the area. This agrees with the geologic literature that indicates the rocks in this zone (the Pan-African mobile belt) have witnessed a period of remobilization and reactivation that took place during the Pan-African thermo-tectonic event.

Equator reduction

In low magnetic latitudes, reduction to the equator is being used to focus the peaks of magnetic anomalies over their sources. This could improve the data's interpretability while preserving its geophysical relevance. The inclination and declination of the Earth's main magnetic field determine the shape of any anomaly. The same magnetic body will produce a different anomaly depending on where the anomaly occurs. The reduction to equator filter reconstructs the magnetic field of a data set as if it were at the equator.

The study area is located at a low latitude. At lower altitudes, a distinct amplitude adjustment is normally needed to avoid the north-south signal in the data from controlling the results. This explains why the trend orientation remains the same. It shows the most of the basement rocks have large remnant magnetizations similar to the present-day orientation.

The TMI data was reduced to the equator by assuming an inclination of I = –0.47° and a declination of D = –6.78° according to IGRF (International Geomagnetic Reference Field). To reduce the field to the equator, the Geosoft package software V.6.3 has been used (transformation done in the Fourier domain). These algorithmic transformations correlate to space domain convolutions of the initial signal with a specific operator. Analyses have usually been done in the Fourier domain, for which convolution was replaced by simple multiplication. The magnetic field and magnetization would be horizontal, as with the majority of magnetized sources.

The RTE map (Figure 7) depicts various zones based on magnetic intensity variations that may be associated to structural variation zones based on geologic investigations. The study area's southeastern corner has the largest magnetic intensity values.

Horizontal and vertical gradient

A horizontal gradient map can be used to define the contacts between basement lithologies, which can represent individual basement blocks, faults and fault boundaries, and other linear features. However, keep in mind that the horizontal gradient method requires many assumptions, and that violations of these assumptions can result in contact displacement away from their true locations.

When compared to the TMI and RTE-TMI maps, the horizontal gradient method provides contact locations that are continuous, thin, and straight (Figure 8). The HGM map reveals significant anomalies in the ENE-SWS and NE-SW directions. The range of anomalies is -5446.9 gammas to 5460.9 gammas. The anomalies are associated with a geological contact zone with a significant magnetic susceptibility difference. The maxima of the HGM map are shown to highlight the contacts direction shown on the HGM map. This map reveals structural complexities, such as faults in the basement. As a result, the horizontal gradient method is used to locate physical property (magnetization) boundaries.

Derivatives do have influence in sharpening anomaly edges and improving simplistic features. To improve magnetic anomalies affiliated with faults and other structural discontinuities, the first vertical derivative of the residual map is used. The TMI map has been sharpened in

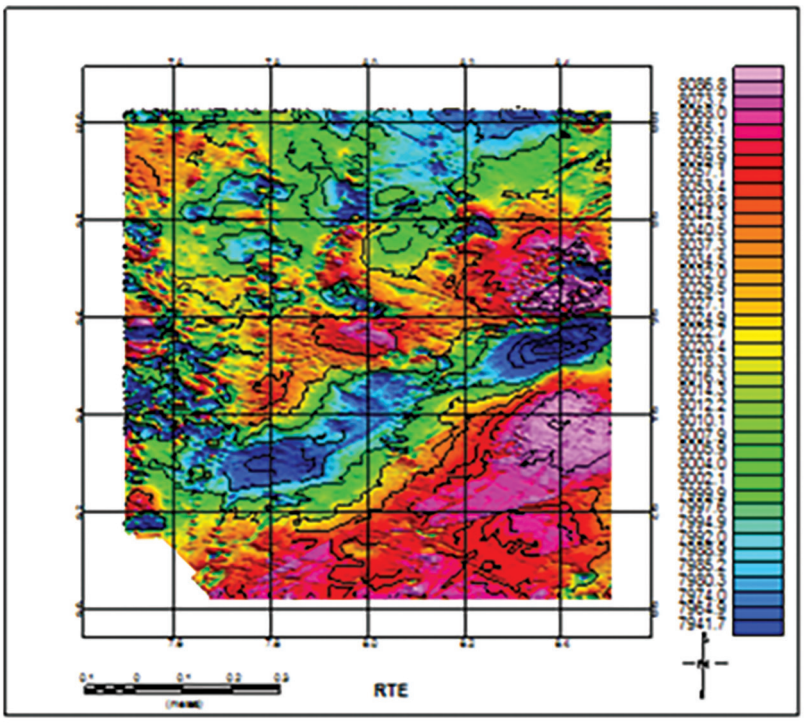

Figure 7: *Reduction to equator of the aeromagnetic field over the study area as a color-shaded, contoured map.*

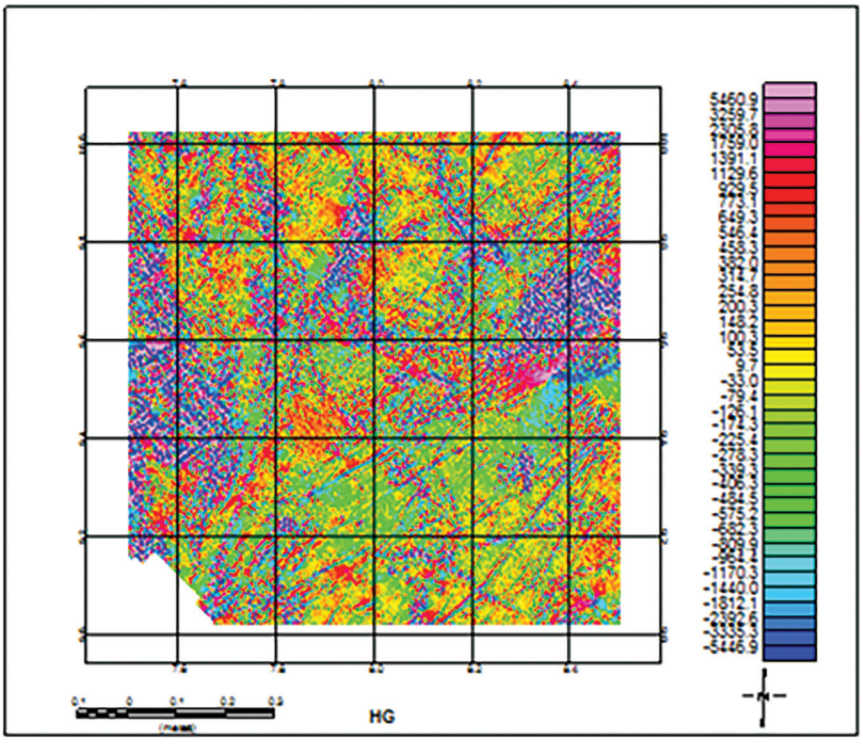

Figure 8: *Horizontal gradient of the aeromagnetic field over the study area as a color-shaded, contoured map.*

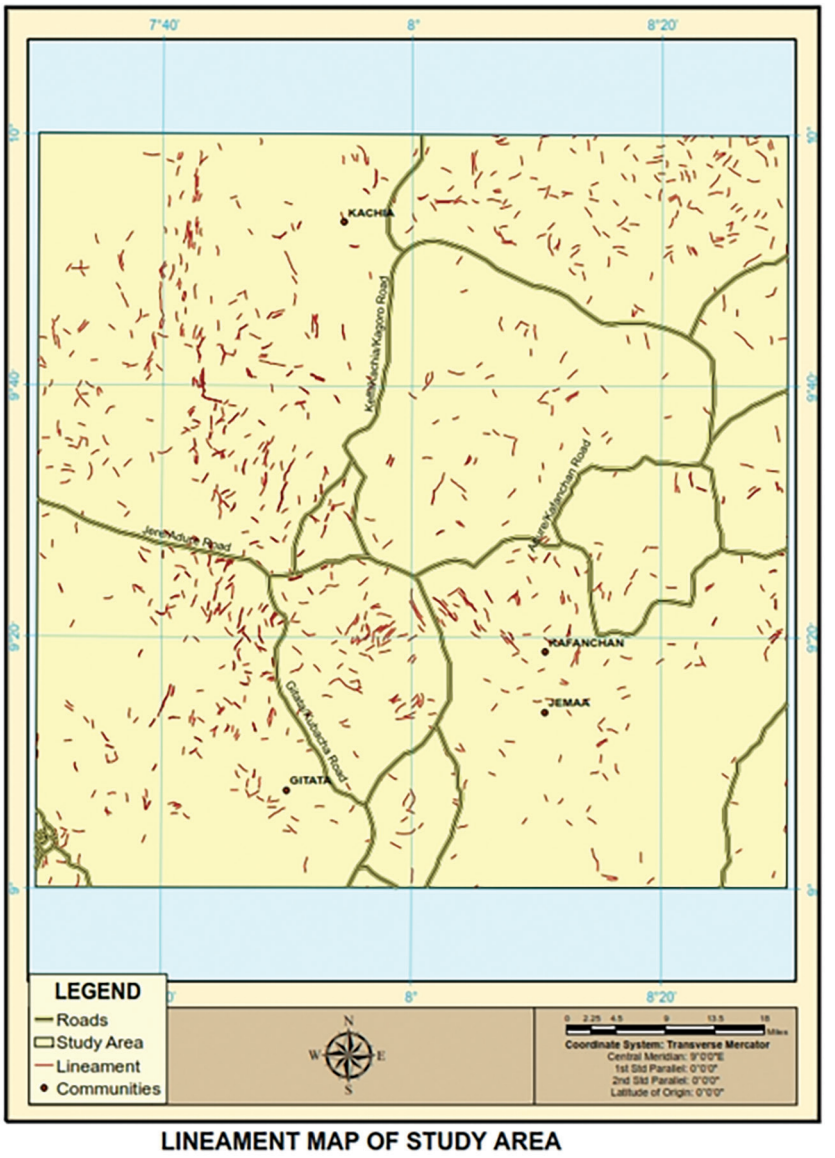

Figure 9: *Lineament map of study area.*

Figure 9. Concealed features such as fractures and dykes dominated. The geological contacts that are important for the structural framework of the study area are highlighted. Fractures and faults, and the formation of intrusive and dyke-like structures, are the effect of regional metamorphism, tectonism, and magmatism in the research region.

The lithologic limits between the various formations, primarily basement, were revealed by the zero contours of the second vertical derivatives. The dispersion of mafic and felsic rock-forming minerals was found to be linked to positive and negative second vertical derivative anomalies in the research region.

Spectral depth estimation

SPECTRDEP, a FORTRAN program, was used to perform spectral analysis on the aeromagnetic data. To evaluate the depths of the anomalies to their magnetic sources, the study area was divided into 16 intersecting segments.

Using the power spectrum of the total intensity field, the spectral analysis plot calculates the average depth to buried magnetic rocks. In the spectral analysis, a two-layer (D1 and D2)

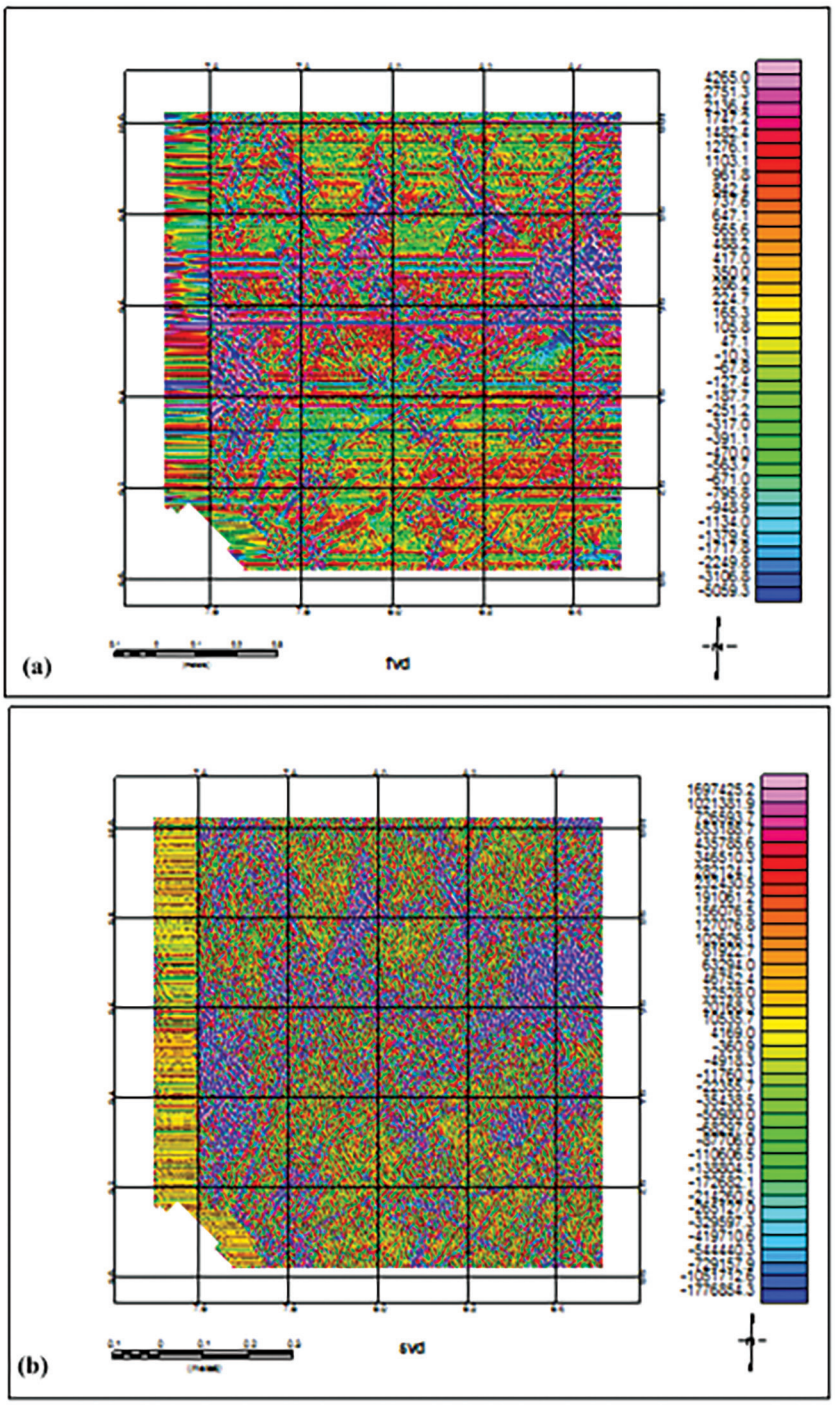

Figure 10: *(a) D1 values (shallow magnetic basement depths) and (b) D2 (basement depths across the study area).*

depth model is proposed. (Figure 10a and 10b). These depths have been calculated using the slope of the log-power spectrum at the lower end of the total wave number or spatial frequency band. The method estimates the depth of a group of magnetized blocks with varying depth, width, thickness, and magnetization.

The estimated depths to magnetic basement are shown as D1 and D2, respectively (Table 2). The depth to the shallower source

represented by the second segment of the spectrum is represented by the first-layer depth (D1). The depth of this layer (D1) ranges from 0.135 km to 0.201 km, with an average depth of 0.140 km. The depth of the second layer (D2) varies between 1.655 km and 2.021 km, with an average depth of 1.882 km. Magnetic rocks that have intruded onto the basement surface may be responsible for this layer. As a result, the D2 values obtained from the spectral plots represent the average depths to the basement complex (sedimentary thickness) in the blocks under consideration.

Table 1: *Computed spectral depths.*

Portions	Depth 1 (m)	Depth 2 (m)
1	136.34	1659.50
2	200.53	1618.28
3	135.85	1585.18
4	136.15	2021.74
5	136.37	1615.90
6	136.36	1864.81
7	136.41	1933.89
8	136.39	1770.43
9	136.36	1655.05
10	136.34	1657.43
11	136.30	1810.54
12	135.98	1784.44
13	136.42	1850.81
14	138.17	1999.46
15	135.50	1756.11
16	135.61	1871.02

Curie point depth, geothermal gradient, and heat flow

From Table 3 below, we observed that the Z_0 centroid of the magnetic source ranges from 12.120 to 15.426 and the depth to the top boundary Z_t ranges from 1.585 to 2.022. The basal depth (Z_b) of the magnetic source was calculated. The obtained basal depth (Z_b) of magnetic sources is assumed to be the Curie point depth. The obtained Curie point depth, which ranges from 22.306 to 29.234, reflects the average local curie depth point values beneath each block. The obtained Curie point was also used to construct curie isotherm as well as the 3-D Curie point depth in the study area. The shallow depth to bottom of magnetic sources indicates a concentration of major geologic

Table 2: *Computed spectral depths in km according to sheets.*

Sheets	Spectra L Block	Longitude		Latitude		Depth (km)	
		X_1	X_2	Y_1	Y_2	D_1	D_2
	13	7.50	7.75	9.75	10.00	0.136	1.851
	14	7.75	8.00	9.75	10.00	0.138	1.999
Kachia	9	7.50	7.75	9.50	9.75	0.136	1.655
	10	7.75	8.00	9.50	9.75	0.136	1.657
	15	8.00	8.25	9.75	10.00	0.136	1.756
Kafanchan	16	8.25	8.50	9.75	10.00	0.135	1.871
	11	8.00	8.25	9.50	9.75	0.136	1.810
	12	8.25	8.50	9.50	9.75	0.135	1.784
	5	7.50	7.75	9.25	9.50	0.136	1.616
Gitata	6	7.75	8.00	9.25	9.50	0.136	1.864
	1	7.50	7.75	9.00	9.25	0.136	1.660
	2	7.75	8.00	9.00	9.25	0.201	1.618
	7	8.00	8.25	9.25	9.50	0.136	1.934
Jema'a	8	8.25	8.50	9.25	9.50	0.136	1.770
	3	8.00	8.25	9.00	9.25	0.136	1.585
	4	8.25	8.50	9.00	9.25	0.136	2.021

Table 3: *Computed spectral depth, Curie temperature and heat flow.*

	Longitude		Latitude				CPD (km)	Geothermal Gradient (°Ckm^{-1})	Heat Flow (mWm^{-2})
SPECTRAL LINES	**X_1**	**X_2**	**Y_1**	**Y_2**	**Z_t**	**Z_0**	**Z_b**	**dT/dZ**	**q**
1	7.50	7.75	9.00	9.25	1.660	14.354	27.048	21.44336	53.6084
2	7.75	8.00	9.00	9.25	1.618	15.426	29.234	14	49.5997
3	8.00	8.25	9.00	9.25	1.585	14.286	26.987	21.49183	53.7296
4	8.25	8.50	9.00	9.25	2.022	12.950	23.878	24.2901	60.7253
5	7.50	7.75	9.25	9.50	1.616	13.980	26.344	22.01639	55.0409
6	7.75	8.00	9.25	9.50	1.865	12.620	23.375	24.81283	62.0321
7	8.00	8.25	9.25	9.50	1.934	12.120	22.306	26.00197	65.0049
8	8.25	8.50	9.25	9.50	1.770	12.340	22.91	25.31646	63.2912
9	7.50	7.75	9.50	9.75	1.655	12.734	23.813	24.35644	60.8911
10	7.75	8.00	9.50	9.75	1.657	14.320	26.983	21.49501	53.7375
11	8.00	8.25	9.50	9.75	1.811	14.240	26.669	21.74809	54.3702
12	8.25	8.50	9.50	9.75	1.784	13.980	26.176	22.15770	55.3943
13	7.50	7.75	9.75	10.00	1.851	13.410	24.969	23.22880	58.072
14	7.75	8.00	9.75	10.00	1.9996	13.510	25.0204	23.18108	57.9527
15	8.00	8.25	9.75	10.00	1.756	13.720	25.684	22.58215	56.4553
16	8.25	8.50	9.75	10.00	1.871	13.340	24.809	23.37861	58.4465

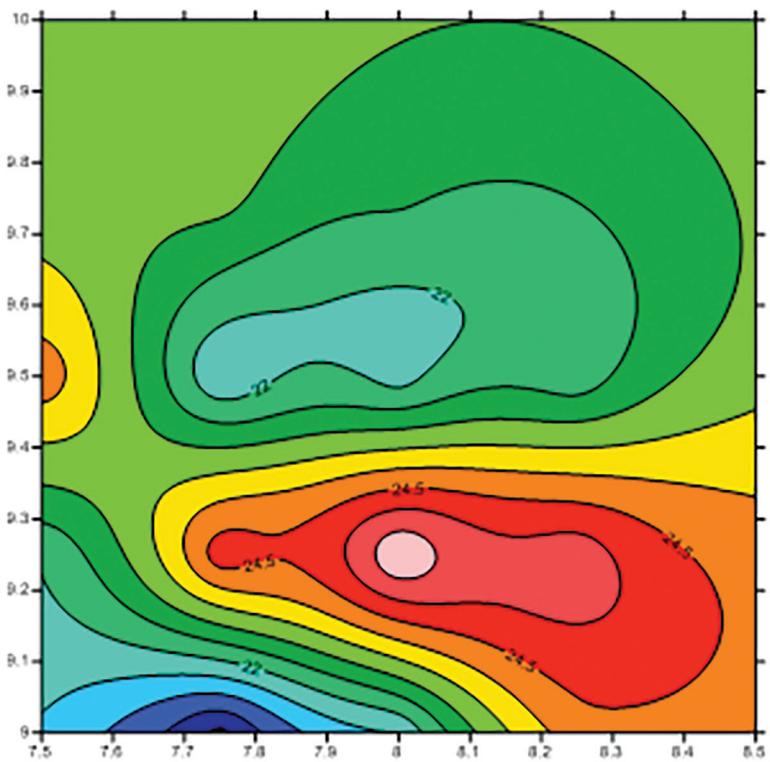

Figure 11: *Plot of the geothermal gradient of the study area.*

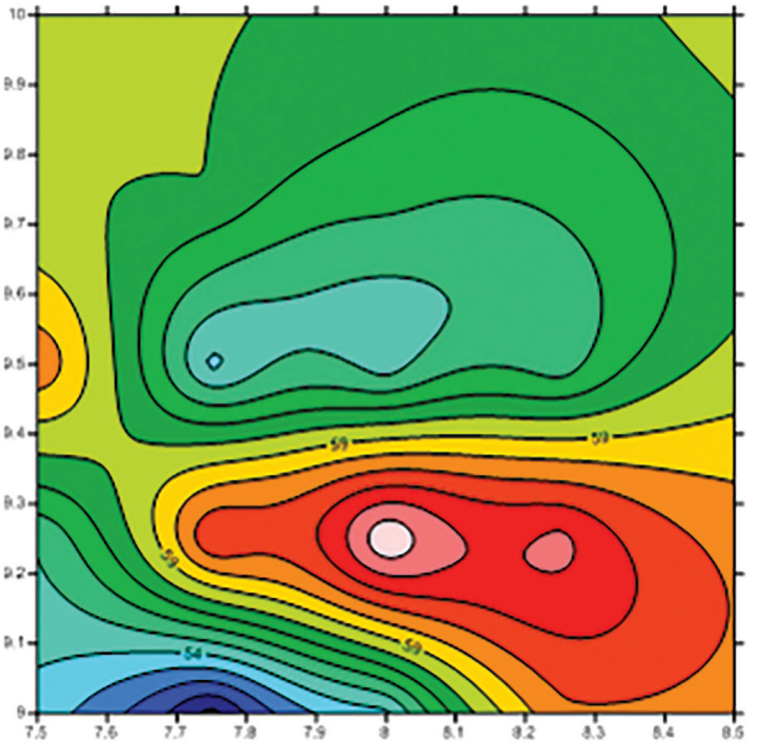

Figure 12: *Plot of the heat flow.*

lineaments (faults and fractures) is noticed in these regions and this is a result magnetic intrusion at depths.

An empirical relation, which is a one-dimensional heat-conductive transport model, is used to estimate heat flow and geothermal gradient. The model is based on Fourier's law. In a one-dimensional case under assumptions, the direction of temperature variation is vertical, and the temperature gradient is assumed to be constant. Using a Curie point temperature of 580 ^{0}C [9], the geothermal gradient was calculated, and it ranges from 19.839 to 26.002 ^{0}Ckm^{-1} with an average geothermal gradient of 22.959 ^{0}Ckm^{-1} (Figure 11).

The heat flow in the study area ranges from 49.608 to 65.005 mW/m^2. The average heat flow obtained in the study area is 57.397 mW/m^2 (Figure 12). This may be considered as typical of continental crust. And this is also consistent with the values of Curie point depth noted in this area. The areas with a high heat flow correspond to areas where we have anomalies. This depicts magnetic anomalies or areas where the crust is thin due to magmatic activities that took place during the tertiary period. The quantitative change in Curie depth observed in the study area implies that the heat flow in the study area is not uniform.

Measurements have shown that a region with significant geothermal energy is characterized by an anomalous high temperature gradient and heat flow. It is expected that geothermically active areas will be associated with shallow Curie points.

3D Euler deconvolution depth estimation

Figure 13a – d show the depth estimate solutions as colored point solutions. Four geological models' standard Euler solutions are presented. The figure shows the depth estimates for structural indexes of 0.0, 1.0, 2.0, and 3.0. The Euler solutions used for the plots were calculated using a variety of geologic models defined by contacts, dike and sill structures, pipes, and spheres. As a consequence, structural indices with values ranging from 0 to 3 were used. Whereas solutions for the standard Euler deconvolution were acquired using diverse structural indices, all of the solutions

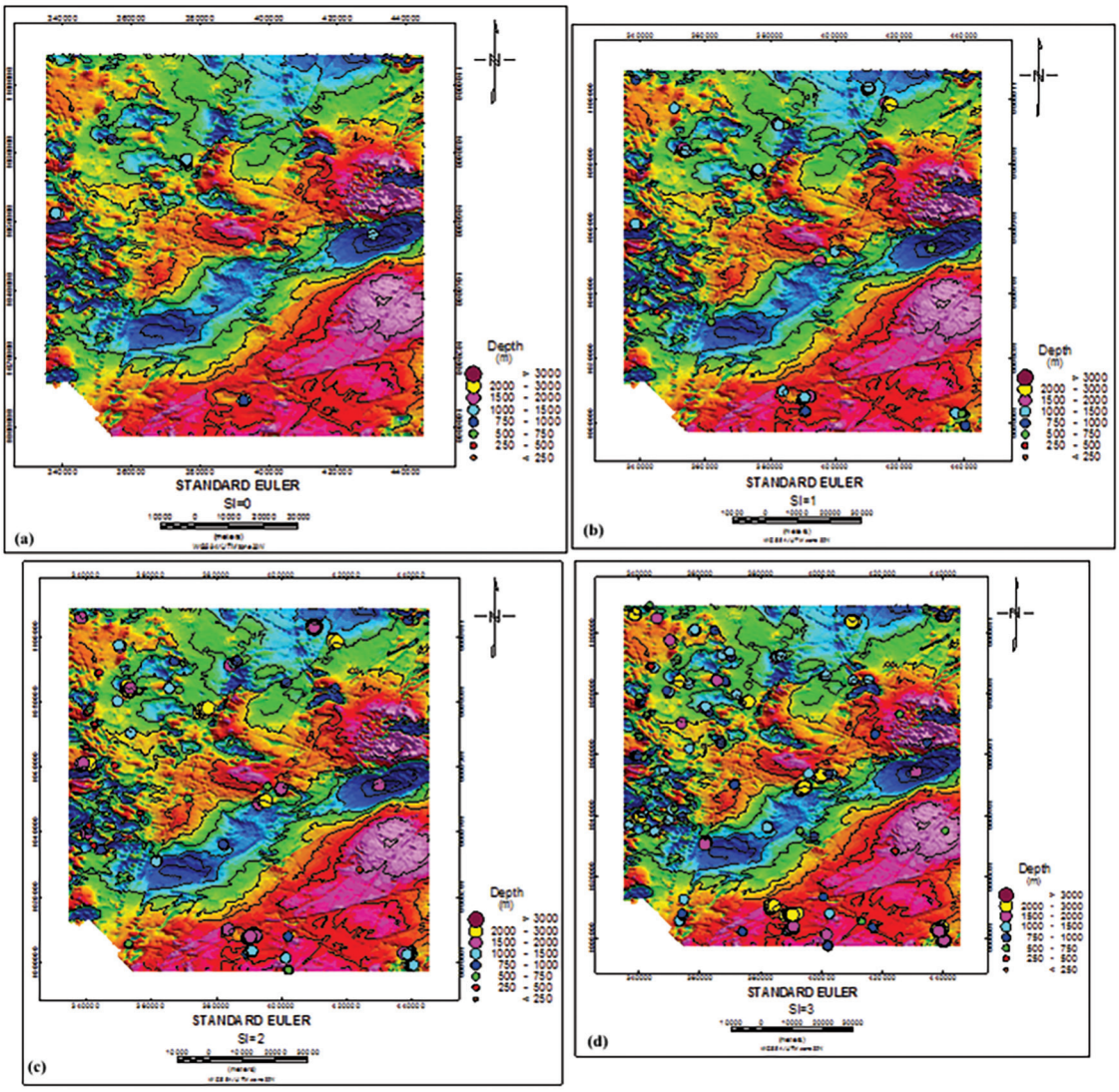

Figure 13: *3D Euler deconvolution depth solutions of the study area: (a) structural index = 0, (b) structural index = 1, (c) structural index = 2, (d) structural index = 3.*

are similar. As a result, Euler I values of 2.0 and 3.0 were considered too high to be expressly interrelated with recognized source bodies in the study region, and the correlating solutions were discarded.

When these depth estimates are compared to the information obtained from the spectral analysis, the results from both depth estimation methods show a positive correlation.

Conclusion

Ther magnetic basement is a group of rocks that underpin sedimentary basins and may occasionally outcrop. Onyedim et al. [17] believe that if magnetic units occur at the basement surface, then depth determinations for these will accurately map the basin floor morphology and structure. Nigeria has a complex network of fractures and lineaments with dominant NE-SW, NW-SE, and N-S axes [18]. A single-digitized total magnetic field map of the study area was created using the aeromagnetic analysis. The map has made the geology and basement topography of the study area clearer.

The study area has an average heat flow of 57.397 mW/m^2, which is less than 60 mW/m^2, but in the southwest region, heat flow increases significantly and can be termed as a

good geothermal source and as such should be investigated through further work to ascertain the cause of the anomaly. The knowledge of the depth to Curie point and its heat flow are of interest and can be related to the thermal history of an area. This study illustrates that surface magnetic data can be used to produce Curie depth estimates even for regions with a paucity of heat flow and geothermal gradient data. On the basis of this result, we then conclude that, the most plausible mechanism responsible for the moderate heat flow observed in this study is tectonically induced rifting and magmatism that occurred during the cretaceous, tertiary period and Pan-African orogeny.

The result of the Euler deconvolution suggests that there could be a presence of geologic structures such as dykes and sills in the area. This is substantiated by the many clusters in the Euler deconvolution map. This suggests the possibility of deep-seated intrusive rocks in the area.

A region with significant geothermal energy has an anomalous high temperature gradient and heat flow. It is expected that geothermically active areas will be associated with shallow active points. Geothermal energy can also be found in areas where basement rocks with reasonably mild heat flow are surrounded by a thick layer of thermally insulated sediments. As there is no indication of volcanic activity in the study region, it can be deduced that geothermal prospect areas in this study could be areas in which a thick blanket of thermally insulated sediment covers basement rocks; thus, these areas with high heat flow might be geothermal sources and reservoirs and will aid in defining the presence of productive geothermal reservoirs at desirable temperatures and depths in the study region. The pattern of the Curie point depths is useful as an index of geothermal structure.

References

[1] Abraham, E.M., Obande, E.G., Chukwu, M., Chukwu, C.G., Onwe, M.R. (2015): Estimating depth to the bottom of magnetic sources at Wikki Warm Spring region, northeastern Nigeria, using fractal distribution of sources approach. *Turkish Journal of Earth Sciences*, 24, pp. 31–50.

[2] Okereke, C.N., Ananaba, S.E. (2006): Deep crustal lineament inferred from aeromagnetic anomalies over the Niger Delta, Nigeria. *Journal of Mining and Geology,* 42, pp. 127–131.

[3] Hamidu, H., Bala, A.E., Ikpokonte, A.E. (2013): Assessment of groundwater potentials of the crystalline aquifers using hydraulic properties for Gidanwaya town and its environs, southern parts of Kaduna state, northwestern Nigeria*. Journal of Environment and Earth Science,* 3(14), pp. 12–24.

[4] Opara, A.I, Onyewuchi, R.A, Selemo, A.O, Onyekuru, S.O., Ubechu, B.O. (2014): Structural and tectonic features of ugep and environs, calabar flank, Southeastern Nigeria: evidence from aeromagnetic and landsat-ETM data. *Mitteilungen Klosterneuburg,* 3(16), pp. 23–27.

[5] Opara, A.I., Emberga, T.T., Oparaku, E., Essien, A.G., Onyewuchi, R.A., Echetama, H.N., Muze, N.E., Rock, O. (2015): Magnetic basement depth re-evaluation of Naraguta and environs north central Nigeria, using 3-D Euler deconvolution. *American Journal of Mining and Metallurgy*, 3(2), pp. 29–42.

[6] Kasidi, S., Nur, A. (2013): Estimation of Curie point depth, heat flow and geothermal gradient inferred from aeromagnetic data over Jalingo and environs, North-eastern Nigeria. *International Journal of Science and Emerging Technology*, 6(6), pp. 2–9.

[7] Lawal, K.M., Akaolisa, C.Z. (2006): Bougher correction density determination from fractal analysis using data from parts the Nigerian Basement complex. *Nigerian Journal of Physics*, 18(2), pp. 251–254.

[8] Nuri, D.M., Timur, U.Z., Mumtaz, H., Naci, O. (2005): Curie point depth variations to infer thermal structure of the crust at the African-Eurasian convergence zone, SW Turkey. *Earth Planets Space,* 57, pp. 373–383.

[9] Nwankwo, L.I., Olasehinde, P.I., Akoshile, C.O. (2011): Heat flow anomalies from the spectral analysis of airborne magnetic data of Nupe Basin, Nigeria. *Asian Journal of Earth Sciences,* 1(1), pp. 1–6.

[10] Salem, A., Ushijima, K., Elsirafi, A., Mizunaga, H. (2000): Spectral analysis of aeromagnetic data for geothermal reconnaissance of Quseier area, northern Red Sea, Egypt. *Proceedings World Geothermal Congress 2000*, Kyushu - Tohoku, Japan, May 28 - June 10, 2000, pp. 1669–1674.

[11] Grant (1978).

[12] Ajibade (1980)

[13] Tanaka, A., Okubo, Y., Matsubayashi, O. (1999): Curie point depth based on spectrum analysis of the magnetic anomaly data in east and southern Asia. Elsevier science B. V. *Tectonophysics*, 306, pp. 462–470.

[14] Ofoegbu, C.O., Odigi, M.I., Okereke, C.S., Ahmed, N.M. (1992): Magnetic anomalies and the structure of Nigeria's Oban massif. *Journal of African Earth Sciences*, 15(2), pp. 271–280.

[15] Hsieh, H., Chen, C., Lin, P., Hong-Yuan, Y. (2014): Curie point depth from spectral analysis of magnetic data in Taiwan. *Journal of Asian Earth Science*, 90, pp. 26–33.

[16] Tselentis, G.A. (1991): An attempt to define Curie depth in Greece from aeromagnetic and heat flow data. *PAGEOPH*, 136(1), pp. 87–101.

[17] Onyedim, G.C., Awoyemi, E.A. (2005): Aeromagnetic imaging of the basement morphology in the part of the middle Benue Trough. *Journal of Mining and Geology*, 42(2), pp. 157–163.

[18] Ananaba, S.E., Ajakaiye, D.E. (1987): Evidence of tectonic control of mineralization of Nigeria from lineament density analysis: a landsat study. *International Journal of Remote Sensing*, 1(10), pp. 1445–1453.

Original Scientific Article • DOI: 10.2478/rmzmag-2021-0021

Received: July 09, 2022
Accepted: October 10, 2022

Integration of VLF-EM and VES data for pavement failure investigation in a typical basement complex terrain of southwestern Nigeria

Kombinacija VLF-EM in VES podatkov pri preiskavi poškodb cestišča na magmatsko-metamorfni podlagi jugozahodne Nigerije

Akintunde A. Oyedele[1,*], Musa A. Bawallah[2], Joshua T. Akinwamide[3], Stephen O. Ilugbo[4], Segun N. Ogunyebi[5]

[1]Department of Physics, Ekiti State University, Ado Ekiti, Nigeria
[2]Department of Applied Geophysics, Federal University of Technology, Akure, Nigeria
[3]Department of Civil Engineering, The Federal Polytechnic, Ado – Ekiti, Nigeria
[4]Department of Physics, Lead City University, Ibadan, Nigeria
[5]Department of Mathematics, Ekiti State University, Ado – Ekiti, Nigeria

*Corresponding author: E-mail: akinakin02@yahoo.com

Abstract

Geophysical investigations involving very low frequency electromagnetic (VLF-EM) and vertical electrical sounding (VES) techniques were deployed to study the pavement failure along a major road in a typical basement complex terrain of southwestern Nigeria. This study was designed to assess the failure and provide a basis for ultimate engineering design. The study delineated a 3- to 4-layer geoelectric sequence: a topsoil of thickness varying from 0.4 to 1.2 m, a spectrum of clayey materials of thickness varying from 1.9 to 14.5 m and a weathered/fractured basement occurring at depths of between 3.6 and 15.0 m. The shallow basement indicated low bearing capacity, with resistivity values ranging from 62.1 to 377.9 Ωm. The presence of clay/clayey materials, linear features and the effect of rising water table within the influence zone underlined the pavement failure. This information will facilitate appropriate designing, soil improvements and selection of materials for road construction that can stand the test of time.

Keywords: basement, fractures, pavement failure, stability, subsoil characterization

Povzetek

Za določitev vzroka poškodb cestišča na magmatsko-metamorfni podlagi jugozahodne Nigerije smo uporabili zelo nizkofrekvenčno elektromagnetno metodo (VLF-EM) in vertikalno električno sondiranje (VES). Namen raziskave je bila ocena poškodb cestišča in pridobitev podatkov za ustreznejšo izvedbo cestišča, ki bo dolgoročno obstojno. Z omenjenima metodama smo ločili tri do štiri plastno geoelektrično zaporedje. Zgornji horizont tal je debel 0,4 do 1,2 m, sledi nabor zaglinjenih tal debeline 1,9 do 14,5 m ter preperela/razpokana podlaga na globini 3,6 do 15,0 m. Plitva podlaga kaže nizko nosilnost z upornostjo med 62,1 in 377,9 Ωm. Poškodbe cestišča lahko pripišemo prisotnosti gline/glinenih mineralov, linearnim strukturam in nihanju gladine podzemne vode. Ti podatki bodo pripomogli k primernemu načrtovanju, izboljšanju lastnosti tal in primerno izbiro materialov za izdelavo cestišča, ki bo obstojno dlje časa.

Ključnebesede: podlaga, razpoke, porušitev cestišča, stabilnost, karakterizacija podpovršja

Introduction

The incessant pavement failure along the Ado-Ikere road, a trunk "A" road in Southwestern Nigeria, has been a major concern to road users and relevant stakeholders. Reconstruction and rehabilitation works have not produced desired utility as the road slipped into failure shortly afterwards [1]. The huge financial and human resources committed to road construction demand that pavements do not fail soon after commissioning. It is however observed that several segments of our highways fail perpetually and are objects of rehabilitation with an accompanying colossal financial burden [2, 3].

Road failures have been attributed to poor visco-elastic properties of asphalt binder [4], inadequacies in pavement structural design [5] and poor sub-grade soil properties [6]. Adeyemo & Omosuyi, Akintorinwe et al., Layede et al. [7–9] and similar works hinged most problems of road failure on inadequate knowledge of the subsurface and associated geologic features governing the competency of the subsoil materials which bear the pavement.

The Ado-Ikere road is underlain by the basement complex terrain of southwestern Nigeria. Basically, the rocks weather to produce residual soils of varying geotechnical properties. The heterogeneous nature of the subsurface demands investigation in considerable detail [9, 10]. Adequate knowledge of the subsoil has become imperative for design and construction of civil engineering structures to mitigate failure.

The need for geophysical characterization of the subsurface and appraisal of the nature and integrity of the subsoil supporting pavement structure has been recognized. Geophysical studies provide a relatively rapid and cost-effective means of deriving aerially distributed information on subsurface geology. The methods offer characteristic bedrock delineation, lithological boundary differentiation and determination of structural trends. Geophysical methods are capable of detecting and delineating local features of potential interest that couldn't have been discovered by any realistic drilling programme [11, 12].

Road failures are associated with losses in terms of capital, labour and human misery. Often, road accidents are traceable to the deplorable conditions of roads, many a time resulting in severe injuries and loss of lives. The Ado-Ikere road often slips into failure not long after rehabilitation works. The road has been decimated by recurrent pavement failures.

The Ado-Ikere road is the main link between Akure and Ado-Ekiti, capital towns of Ondo and Ekiti States, Nigeria, respectively (Figure 1). The area lies in the tropical rain forest with mean annual rainfall of about 1300 mm and annual mean temperature of between 18 °C and 33 °C. The study area is underlain by the Precambrian basement complex of southwestern Nigeria (Figure 2).

The coarse-grained charnockitic rocks occupy the central portion of the study area. The coarse-grained type is the most prominent and is found in association with coarse-grained porphyritic granites. The fine-grained type occurs between the coarse-grained and gneissic fine-grained charnockitic rocks. The quartzite occurs as elongated bodies within the charnockitic, granitic, gneissic and migmatitic rocks. They are prominent as narrow ridges. The associated rock units include coarse-grained biotite and biotite hornblende granite and coarse-grained charnockitic rocks [1, 13, 14].

The thrust of this paper is to assess the pavement failure along the Ado-Ikere road using non-invasive VLF-EM and VES geophysical surveying. This information will provide a basis for ultimate engineering design and forestall the recurrent pavement failures.

Materials and methods

Very low frequency electromagnetic (VLF-EM) and vertical electrical sounding (VES) techniques were employed for the study. The theory and principles of the methods abound in the literature [12, 15, 16]. The methods being non-invasive enabled in-situ measurements and ensured preservation of the subsoil in its natural state. This combination has been widely used in engineering site investigations, given the existing good correlation of attributes such as electrical properties, geological composition and fluid content [7, 9, 17].

VLF-EM is an effective tool in mapping conductive materials and geologic structures in the

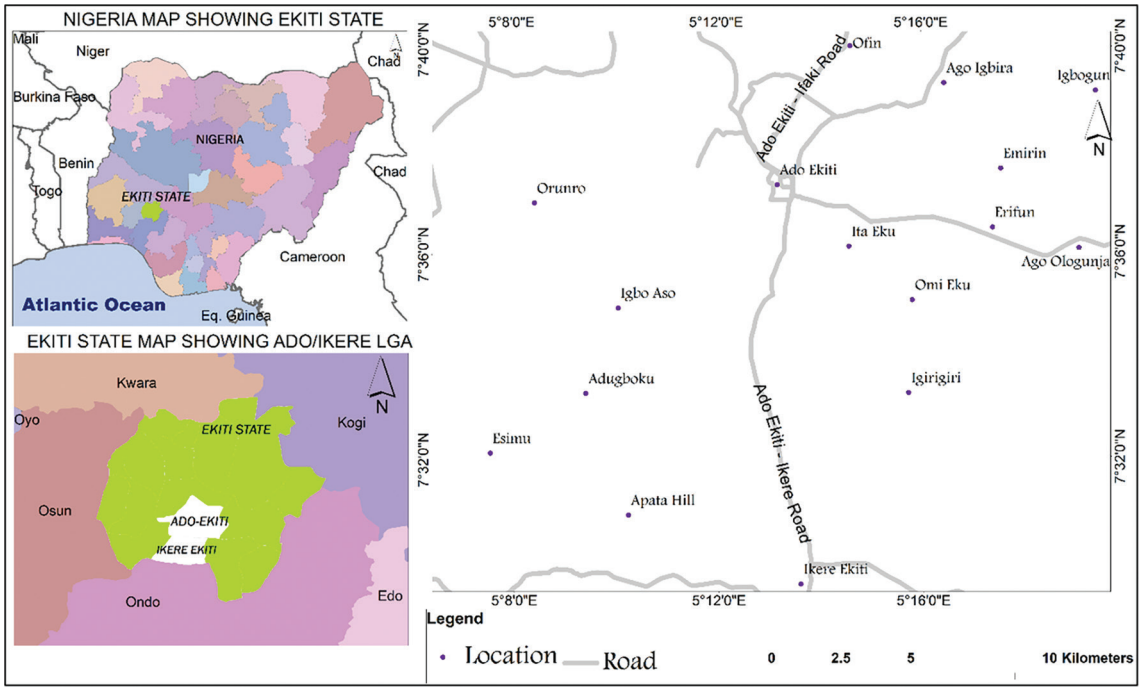

Figure 1: *Location Map of The Study Area.*

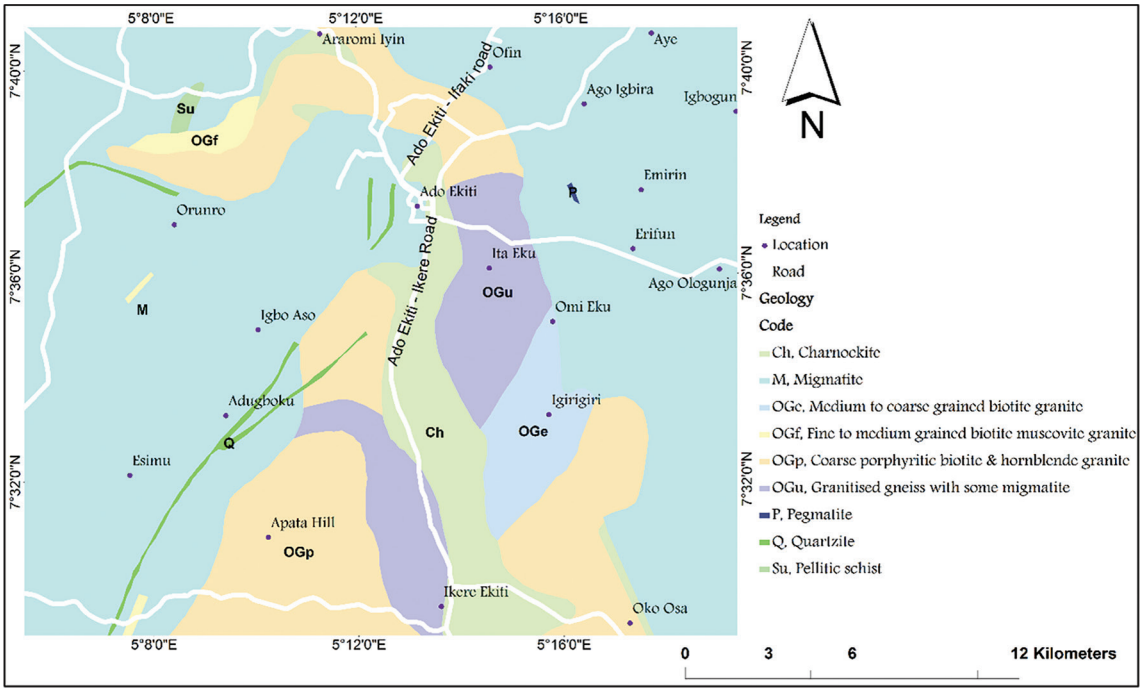

Figure 2: *Geological Map of Ado-Ekiti /Ikere-Ekiti Area, SW Nigeria.*

subsurface. The method detects electrical conductors, such as moderate to steeply dipping water-filled fractures or faults, by utilizing radio signals in the 15 to 30 kHz range. The method gives recognizable signatures over conductive bodies [15, 16]. The VES technique provides 1-D layering information in terms of resistivity variation with depth in site investigation.

The electrical resistivity method is well suited for structural mapping and lithology differentiation [17, 18].

The VLF-EM data were acquired along a profile parallel to the road, covering a distance of 1710 m at a 10 m station interval. ABEM WADI electromagnetic receiver unit synchronized with the radio signal from the GBR station located in Rugby (England) operating at a frequency of 18.8 kHz was used for the survey. The equipment measured the raw real/in-phase and imaginary/quadrature components of the vertical to horizontal magnetic field ratio on the field. An in-built filtering program provided by the equipment and a software package KHFfilt Version 1.0 enabled the conversion of the raw real data into filtered real data in which anomaly inflections appear as peak positive anomalies and false VLF anomaly inflections as negative anomalies of the profile. VLF-EM 2D Inversion model was prepared following the application of Fraser Filtering and Karous-Hjelt Filtering [19]. The VLF-EM mapping was particularly deployed to isolate subsoil conductive zones and linear structures of geological importance.

Subsequently, 12 VES stations were occupied along the profile. Measurements of ground resistance were made with a unit of Resistivity Meter. Schlumberger configuration with the half-current electrode separations ranging from 1 to 100 m was adopted for the survey. The current electrodes were moved more often during measurements until the measurable signal became very small. The potential electrodes were then expanded symmetrically around the point of investigation. The terrameter gave the apparent resistivity values digitally as computed fundamentally from Ohm's law. The VES data were plotted as depth sounding curves and interpreted qualitatively and quantitatively. The quantitative interpretation entailed partial curve matching and computer iteration technique with the aid of RESIST computer software. The subsurface 2D geoelectric sections were generated using the resulting layer resistivities and thicknesses [8, 9].

Results and discussion

The VLF-EM profile

The VLF-EM measurements and the filtered graphs are presented in Figures 3–6. The in-phase profile shows positive peaks of different intensities, suggesting the presence of shallow and deep conductors [16, 17]. The 2D inversion model shows the variation of equivalent current density and change in conductivity with depth. It discriminates between conductive and resistive structures. Higher values of relative current density are indicative of conductive subsurface structures with varying low values of resistivity while

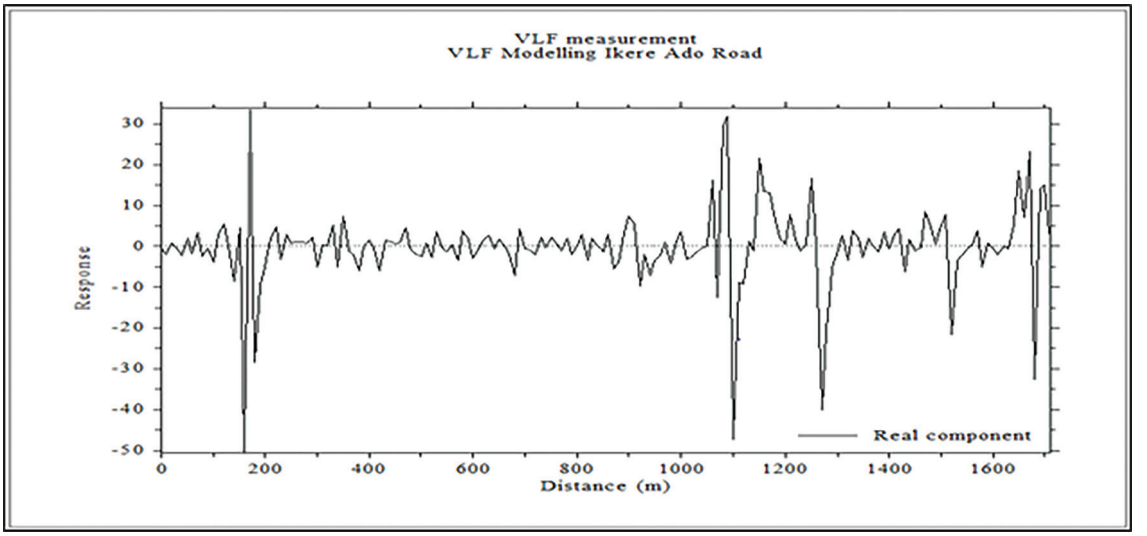

Figure 3: *VLF-EM measurement of the study area.*

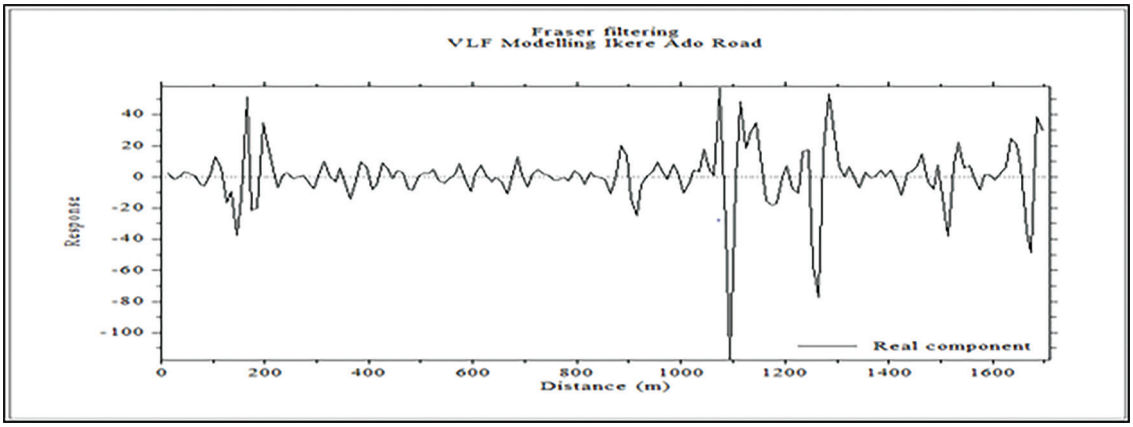

Figure 4: *VLF-EM Fraser Filtering Graph of the study area.*

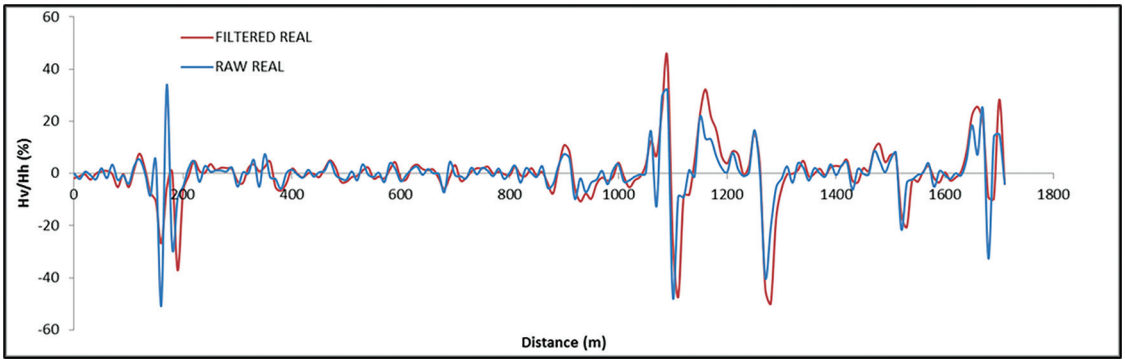

Figure 5: *VLF-EM data (raw real and filtered real) of the study area.*

lower values correspond to zones of low conductivity characterized by higher values of resistivity.

The 2D pseudosection indicates stable, partly failed, unstable and very unstable portions along the profile (Figure 6). The highly conductive zones, delineated as very unstable portions (distances of 150–260 m, 990–1200 m and 1600–1710 m) are underlain by conductive subsurface structures. These include linear geological structures (trending in different directions) which are indicative of major subsurface fractured/faulted zones with varying degrees of saturation and other conductive zones with lower positive amplitude suggesting the presence of clayey soil materials and/or fractures at varying depths. Partly unstable zones (distances of 0–100 m and 260–820 m) are characterized by moderately low conductivity values.

Distances of 100–150 m and 1200–1260 m correspond to the stable zones and are composed of highly resistive materials. These portions are characterized by lower values of relative current density. The stable segments of the road are generally devoid of geological features [7, 9, 18].

Geoelectric sequence and characteristics

A summary of the VES interpretation results is presented in Table 1. The curve types are H, A, Q, KQ, KH and QH; these are curves with occurrence of 33%, 17%, 8%, 8%, 17% and 17% respectively. They reflect the degree of weathering, fracturing and geoelectric complexity in the study area [8, 13, 14]. Figure 7 shows typical resistivity type curves in the study area.

The H-type curve predominates the area of study. A stratigraphic sequence comprising the topsoil whose composition is variable alluvium,

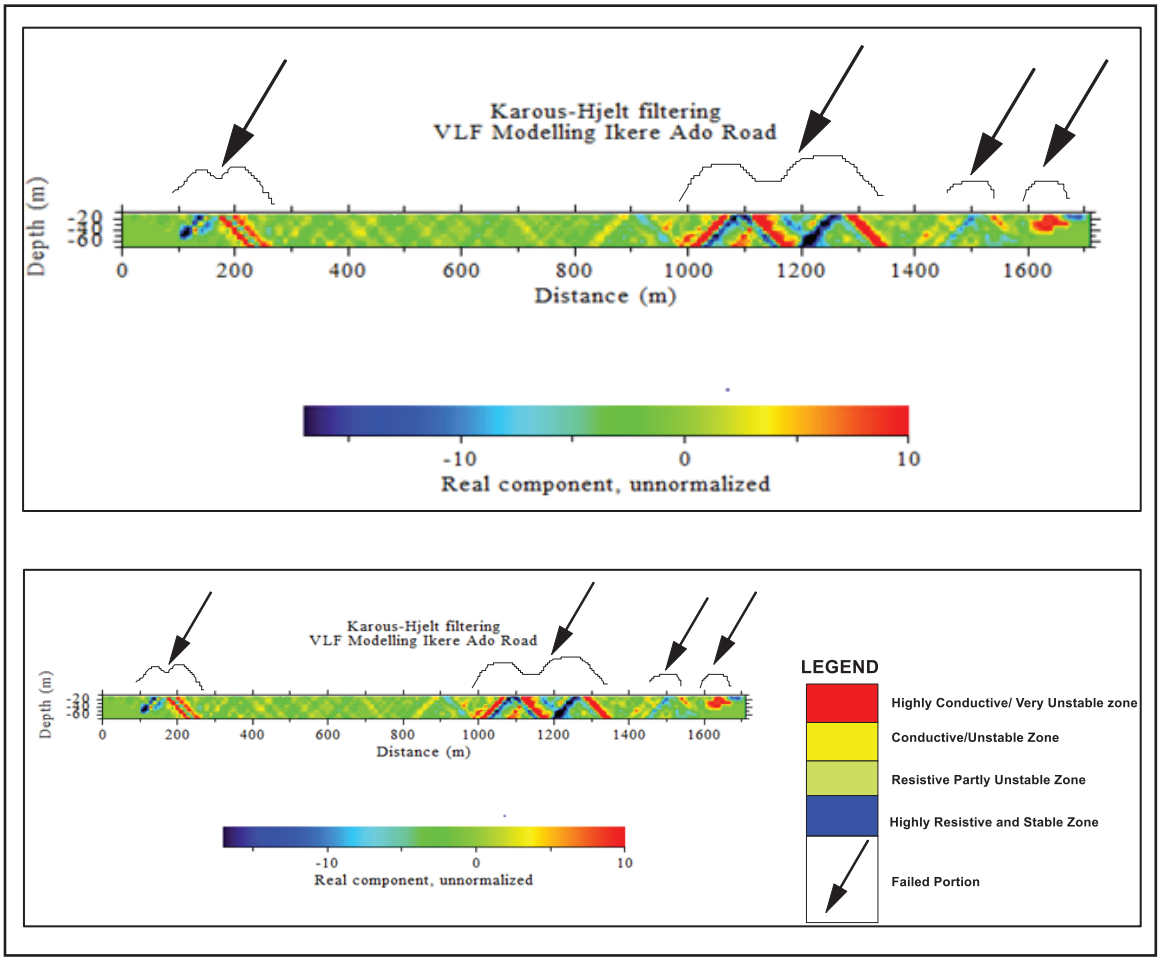

Figure 6: *VLF-EM 2D Inversion model of the study area.*

sand, lateritic clay or clay followed by clay/sandy clay and the bedrock corresponds to the H-type curve. The bedrock could be weathered or possibly fractured basement. The intermediate layer is characterized by low resistivity. It is commonly water-saturated. The A-type curve presents subsurface conditions in which there is a persistent increase in the layer resistivity values from the topsoil to the basement rock ($\rho_1 < \rho_2 < \rho_3$). It suggests increasing subsoil strength and integrity [3, 9, 11].

The underlying geoelectrical units in QH-type curves consist of clay and clayey sand/sand, respectively. The clayey sand and the weathered/fractured basement may jeopardize the stability of the pavement with varying degree of saturation. The KH-type curve has a succession of sand/sandy clay topsoil, lateritic clay, weathered basement and the fresh bedrock. The third layer is essentially clayey [7, 8].

The geoelectric sections

The 2D geoelectric sections, Figures 8–10, reveal the subsurface geology and structural disposition of the study area. Figure 8 shows the 2D section beneath VES 1 to 4 (segment I). The first layer constitutes the topsoil with layer resistivity values ranging from 57.4 to 288.4 Ωm indicating materials of varying clay contents. The thin layer has an average thickness of 0.65 m except at VES 3 where composite clayey material with resistivity of 57.4 Ωm extends to a thickness of up to 6 m. This suggests lateral inhomogeneity and varying level of competence/stability [2, 8].

The topsoil is underlaid by a clayey horizon of resistivity values ranging from 36.2 to 119.3 Ωm. The clayey substratum of about 14 m thickness delineated at VES 1 is inimical to the stability of the pavement as it is subject to flowing under traction. A clay fraction in a

Table 1. *The layer parameters and geoelectric characteristics.*

VES No.	Layer resistivity (Ωm)	Layer thickness (m)	Depth (m)	Curve types	Lithology
1	288.4	0.5	0.5		Topsoil/Laterite
	76.6	14.5	15	H	Clay
	182.6	-	-		Weathered layer
2	138.4	0.9	0.9		Topsoil/Laterite
	36.2	3.1	4.0	H	Clay
	113.6	-	-		Weathered layer
3	57.1	6.0	6.0		Topsoil/Laterite
	119.3	2.1	8.2	A	Clay
	157.7	-	-		Weathered layer
4	208.3	0.5	0.5		Topsoil
	307.2	1.1	1.6	KQ	Lateritic clay
	102.8	2.0	3.6		Clay
	100.8	-	-		Weathered layer
5	153.6	1.2	1.2		Topsoil
	121.6	2.6	3.8	QH	Lateritic clay
	64.7	8.4	12.2		Clay
	208.2	-	-		Weathered layer
6	170.2	1.0	1.0		Topsoil
	151.8	3.2	4.2	QH	Lateritic clay
	57.0	4.0	8.2		Clay
	126.5	-	-		Weathered layer
7	177.8	1.1	1.1		Topsoil
	277.9	2.1	3.2	KH	Lateritic clay
	48.0	4.2	7.4		Clay
	170.0	-	-		Weathered layer
8	88.7	0.8	0.8		Topsoil
	180.1	4.0	4.8	KH	Lateritic clay
	26.5	5.0	9.8		Clay
	113.9	-	-		Weathered layer
9	289.0	0.4	0.4		Topsoil/Laterite
	66.4	1.9	2.3	Q	Clay
	62.1	-	-		Weathered layer
10	94.9	9.9	9.9		Topsoil/Laterite
	146.0	2.4	12.3	A	Clay
	229.6	-	-		Weathered layer
11	105.7	0.9	0.3		Topsoil/Laterite
	33.4	2.1	3.0	H	Clay
	149.8	-	-		Weathered layer
12	131.5	0.5	0.5		Topsoil/Laterite
	38.2	6.8	7.3	H	Clay
	377.9	-	-		Weathered layer

soil is generally expandable and compressible thereby promoting swelling and shrinkage. High clay contents thus impact weaknesses to the pavement structure [10, 20]. A lateritic cap with resistivity of 307.2 Ωm and average thickness of 1.2 m, observed at VES 4 may support stability at that zone.

The weathered/fractured basement is revealed at varying depths ranging from 4.0 to 15.0 m with a resistivity spectrum of 100.8 to 182.6 Ωm. This affirms a system of linear geological structures prescribed by the VLF-EM profile. The generally low resistivity values indicate low bearing capacity. Transmitting load

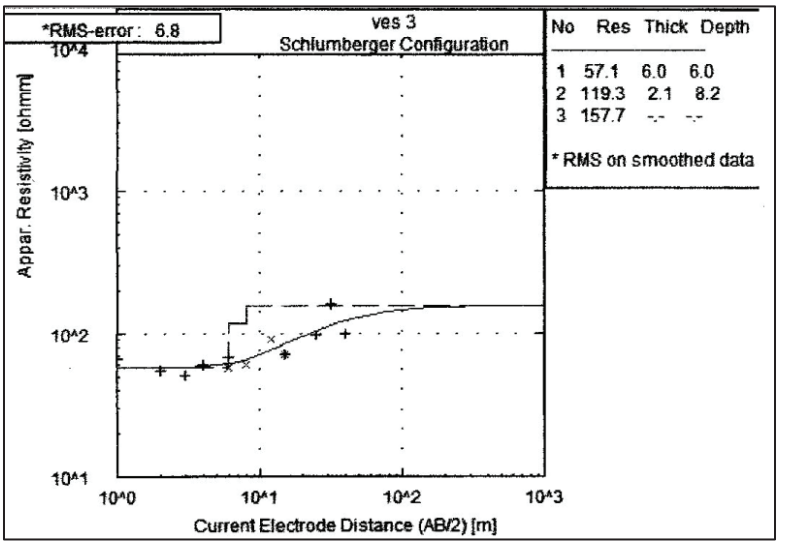

(a) Typical resistivity A-type curve

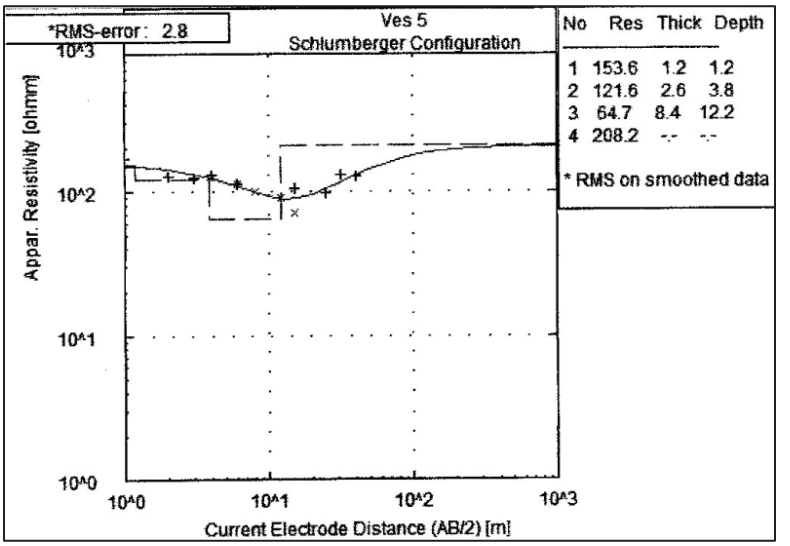

(b) Typical resistivity QH - type curve

Figure 7: *Typical resistivity type curves in the study area.*

to this layer may induce differential settlement of the pavement structure and precipitate failure [3, 7, 9].

Figure 9 reveals a 4-layer geoelectric sequence below VES 5–8 (segment II). The topsoil is clayey with resistivity values ranging from 88.7 to 177.8 Ωm and its thickness varies from 0.8 to 1.2 m. A lateritic crust forms the second layer with resistivity values ranging from 121.8 to 277.9 Ωm and thickness ranging from 2.1 to 4.0 m. This suggests varying levels of competence/stability giving rise to the partly unstable/stable zones along the profile. The average thickness of 2.98 m and varied composition may not absolutely fulfil the expected characteristics of a base course/sub-base course, particularly acting as the structural portion of the pavement and distributing the imposed stresses evenly [2, 9, 11].

The third geoelectric layer, a clay/clayey horizon extending to a depth of about 12.5 m at VES 5 is geotechnically significant. The layer resistivity values ranging from 26.5 to 64.7

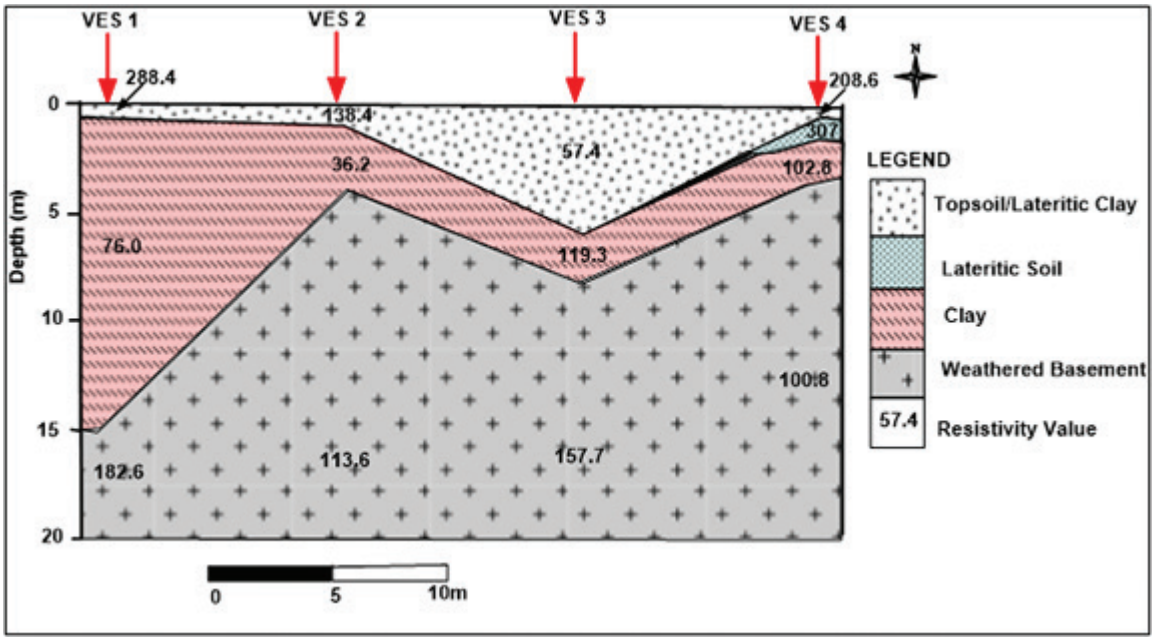

Figure 8: *Geoelectric section of segment I covering VES 1–4 along Ado-Ikere Road.*

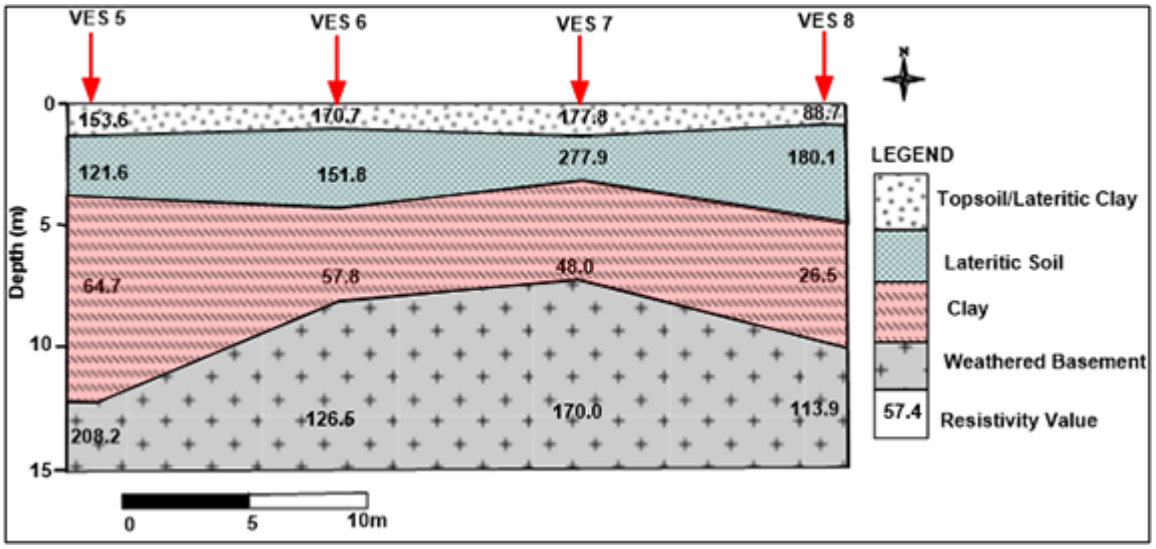

Figure 9: *Geoelectric section of segment II covering VES 5–8 along Ado-Ikere Road.*

Ωm indicate varying degrees of saturation owing to capillary effect. The material in place lacks a basic requirement of sub-base course to facilitate the drainage of free water that may accumulate below the pavement. Clayey formations are prone to differential settlement under prolonged vehicular traffic/axle loading owing to high porosity and practically little or no permeability [5, 21]. This fragile layer is underlain by a weathered/fractured basement with resistivity values ranging from 113.9 to 208.2 Ωm. The degree of weathering and fracturing permits groundwater accumulation and the effect of rising water table. The bearing capacity of the layer is corresponding low [3, 16, 20].

The geoelectric section of segment III encompassing VES 9 to 12 presents a 3-layer geoelectric succession (Figure 10). The resistivity of the topsoil ranges from 94.4 to 289

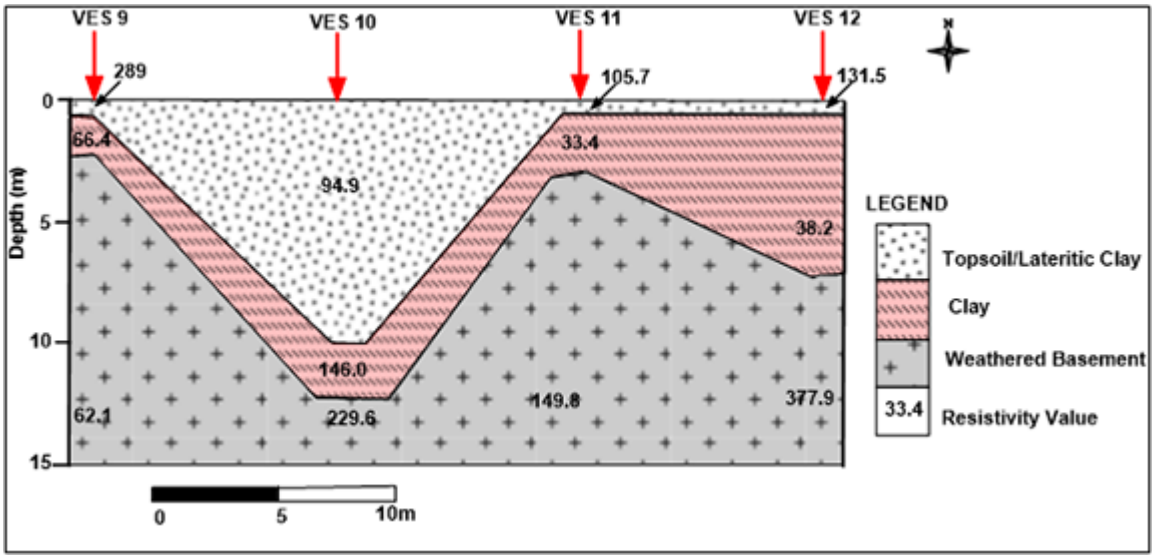

Figure 10: *Geoelectric section of segment III covering VES 9–12 along Ado-Ikere Road.*

Ωm; indicating materials of varying clay contents, with thickness varying from 0.4 to 9.9 m. The generally thin layer is delimited by a massive clayey material (resistivity of 94.9 Ωm) stretching from VES 9 to VES 11 and extending to 9.9 m at VES 10. It is underlaid by a clayey substratum with resistivity value as low as 33.4 Ωm at a depth of 0.9 m around VES 11.

A weathered/fractured basement forms the third layer with resistivity values ranging from 62.1 to 377.9 Ωm. The layer is closer to the surface at VES stations 9 and 11, being at 2.3 m and 3.0 m depth, with associated resistivity values of 62.1 and 149.0 Ωm, respectively. High contrasts of resistivity values confirm the presence of linear features, mainly fractures/faults, lithologic contacts and near-surface lateral inhomogeneity [9, 17].

Adverse effects of groundwater can be expected across the third layer as the features often store groundwater in the basement complex terrain [16, 20]. This geoelectric layer constitutes a layer of low bearing capacity. It is structurally weak and may not be able to support heavy wheel loading structures [6, 18, 22].

Subsoil Integrity Evaluation

The basic structure of a pavement represents four layers of surface: wearing course, base course, sub-base course and the subgrade. A flexible pavement surface reflects the entire behaviour of the subgrade layer. The characteristics of the soil bed over which the entire pavement system rests are indicative of the geotechnical properties of the pavement [21, 22]. Engineering design should be in line with the anticipated traffic load and ultimate strength of the pavement layers to ensure the stability and durability of the pavement structure [2, 18, 23].

The crystalline basement terrain of southwestern Nigeria presents challenges in geotechnical investigations due to the heterogeneous nature of the subsurface and the existence of localized geologic features [13, 20]. In this study, the subsurface geology indicates substantially clayey subsoil with relatively low resistivity values and presence of geological features including fractures, faults and lateral inhomogeneity. The presence of the linear features in the area suggests lithological contacts and/or fault/fracture zones along the road alignment occurring within the coarse-grained biotite and biotite hornblende granite and coarse-grained charnockitic rocks associations [13, 14].

According to Akintorinwa & Oluwole [11] and Asif et al. [23], the electrical resistivity of subsoil increases with increase in compaction and decrease in porosity. Higher moisture content decreases the value of subsoil

resistivity. Compact subsoil is characterized by reduced porosity and moisture content with consequent increase in electrical resistivity. Diastrophic features and lithological contacts are associated with typically high porosity and permeability which enhance groundwater accumulation and transmission. The presence of these tectonic features readily permits the flow of water to the overlying clayey materials. The subgrade at some portions of the road might be wholly or partly immersed in the zone of saturation, particularly during the wet season of the tropics when groundwater table rises, leading to low resistivity and bearing capacity [16, 24]. This geological scenario ultimately promotes heaving, differential settlement and reduction in the load bearing capacity of the near surface subsoil [10, 22, 25].

The failure of the overlying pavement becomes apparent due to the plastic nature of the clayey soil and high moisture content [2, 7, 9]. Clays characterized by low resistivity (usually less than 100 Ωm) are regarded as incompetent materials as they tend to flow under stress. This result agrees with Akintoriwa & Oluwole [11] and Falowo [26], whose studies indicate an inverse relationship between apparent resistivity and moisture content, clay and silt content, liquid limit, plastic index, linear shrinkage, and unconfined compression shear strength. The specific gravity, maximum dry density and California Bearing Ratio (CBR) were shown to exhibit a direct relationship with apparent resistivity.

In an earlier study, Adams et al. [1] adopted conventional geotechnical methods to study the pavement indices influencing failure along the road under investigation, the Ado-Ikere Road, in southwestern Nigeria. The work provides a basis for comparison and validity of the present study. The study classified most of materials in place as clayey soil under group A-2-6 and A-7, rated as fair to poor material for road use according to the AASHTO classification system. The compaction and CBR tests indicated unsuitable base course materials. The soil has a high water retention capacity, with the natural moisture content ranging between 7.7 and 14.5% for base course, between 10.5 and 17.5% for sub-base and between 12 and 19% for subgrade, for all failed segments considered. The liquid limit showed that the majority of the failed section exceeded the allowable limit for base course materials.

The study of Adams et al. [1] significantly affirmed the presence of clayey formation underlying the pavement and effect of a rising water table, as reported in the present geophysical investigations. Application of the geophysical methods enabled delineation of linear geological structures including fractures, faults and lateral inhomogeneity beneath the pavement. The presence of these features renders geomaterials at such regions geotechnically weak with resultant pavement failures [9, 20, 26]. Incessant failure of the pavement under investigation has been promoted by the effect of the rising water table, heterogeneity of the subgrade materials, presence of expansive clays and linear features such as fractures, faults and geological contacts.

Conclusions

Pavement failures along Ado-Ikere Road have been investigated using the integration of data from VLF-EM and VES techniques. The study revealed the dominant presence of clay/clayey materials below the topsoil, the presence of linear features and contributory shallow water table. Aside from any unethical engineering practice, the presence of clayey subgrade, lateral inhomogeneity, near surface geological structures and fluctuations in the saturated zone largely accentuated the pavement failures along the road. Soil stabilization procedures should be deployed as appropriate. These should include excavation to requisite depths, replacement of excavated materials with competent materials, as well as construction of appropriate drainage systems.

The present study demonstrates the usefulness of geophysical techniques in civil engineering works, particularly the advantage of high spatial resolution, over results from boring and coring, which are known to provide information at discrete locations. Geophysical site investigations offer to reduce cost outlay by reducing the number of borings, sampling, and time-consuming tests required in the

geotechnical procedure. An all-inclusive and pragmatic approach is required for subsoil characterization and ultimate engineering design. This is a necessary prerequisite to achieve sustainable development and reduce investment losses through routine rehabilitation of failed segments of highways.

Acknowledgements

The authors gratefully acknowledge all useful suggestions regarding this work.

References

[1] Adams, J.O., Aderinola, O.S., Akinwamide, J.T. (2015): Geotechnical study of pavement indices influencing failure along Ado-Ajebandele-Ikere Road, southwestern Nigeria. *International Journal of Engineering Innovation & Research,* 4(4), pp. 567–572.

[2] Ebhohimen, V., Luke, M. (2014): Geophysical investigation of road failure: The case of Opoji in Nigeria. *International Journal of Scientific & Engineering Research*, 5(1), pp. 1769–1779.

[3] Okpoli, C.C., Bamidele, A.A. (2016): Geotechnical investigation and 2D electrical resistivity survey of a pavement failure in Ogbagi Road, southwestern Nigeria. *International Journal of Basic and Applied Sciences,* 2(7), pp. 47–58.

[4] Nahid, E. (2011): Enhanced Pavement Management System. In: *Proceedings of the Conference on Engineering Research, Innovation and Education,* Bangladesh, pp. 324–332.

[5] Ogundipe, R., Olumide, M. (2012): Road pavement failure caused by poor soil property. *International Journal of Engineering Technology*, 2(1), pp. 7–15.

[6] Talukder, M.J. (2009): Evaluation of existing pavement of Sylhet-Sunamganj Road by dynamic cone penetrometer. The Institution of Engineers, Bangladesh Penetrometer. *Journal of Civil Engineering*, 35(1), pp. 51–59.

[7] Adeyemo, I.A., Omosuyi, G.O. (2012): Geophysical investigation of road pavement instability along part of Akure-Owo Expressway, southwestern Nigeria. *American Journal of Scientific and Industrial Research,* 3(1), pp. 191–197.

[8] Akintorinwa, O.J., Ojo, J.S., Olorunfemi, M.O. (2010): Geophysical investigation of pavement failure in a basement complex terrain of southwestern Nigeria. *Pacific Journal of Science and Technology*, 11(2), pp. 649–663.

[9] Layade, G.O., Adegoke, J.A., Oyewole, I.T. (2017): Integrated geophysical investigation of the causes of road pavement failure along Ibadan-Lagos Dual-Carriage, southwestern Nigeria. *Journal of Applied Science and Environmental Management*, 21(3), pp. 547–554.

[10] Imoukhuede, M.I., Ayibawari, O.E., Michael, E.O. (2014): Evaluation of the geotechnical properties of residual soils in two different basement complex areas of Nigeria. *British Journal of Applied Science and Technology*, 4(36), pp. 5000–5013.

[11] Akintorinwa, O.J., Oluwole, S.T. (2018): Empirical relationship between electrical resistivity and geotechnical parameters: A case study of Federal University of Technology campus, Akure SW, Nigeria. *NRIAG Journal of Astronomy and Geophysics*, 7(1), pp. 123–133.

[12] Reynolds, J.M. (2011): *An introduction to applied and environmental geophysics*. Wiley-Blackwell: Chichester, 710 p.

[13] Ayodele, O.S., Akinyemi, S.A. (2014): Petrostructural and mineralogical assessment of the Precambrian rocks in Ikere Area, southwestern Nigeria. *Asian Review of Environmental and Earth Sciences*, 1(3), pp. 66–83.

[14] Olanrewaju, V.O. (1987): Charnockite-granite association in southwest Nigeria. Rapakivi granite type and charnokitic plutonism in Nigeria. *Journal of African Earth Science*, T(1), pp. 67–77.

[15] Aizebeokhai, A.P., Oyeyemi, K.D. (2014): Application of geoelectrical resistivity imaging and VLF-EM for subsurface characterization in a sedimentary terrain, southwestern Nigeria. *Arabian Journal of Geosciences,* 8(6), pp. 4083–4099.

[16] Jayeoba, A., Oladunjoye, M.A. (2013): Hydrogeophysical evaluation of groundwater potential in hard rock terrain of southwestern Nigeria. *RMZ – Materials and Geoenvironment,* 60, pp. 271–285.

[17] Muhammad, T.Z., Nordiana, M., Adeeko, T.O., Rosli, S., Muhammad, N.A.R. (2020): Self-potential and 2D resistivity application for groundwater exploration in fractured reservoirs. *Songklanakarin Journal of Science and Technology*, 42(2), pp. 292–298.

[18] Shao, P., Shang, Y., Hasan, M., Yi, X., Meng, H. (2021): Integration of ERT, IP and SP methods in hard rock engineering. *Applied Sciences,* 11, 10752, DOI:10.3390/app112210752.

[19] Pirttijarvi, M. (2004): *Manual of the KHFFILT Program; Karous-Hjelt and Fraser Filtering of VLF*

Measurements, Version 1.1a; University of Oulu: Oulu, Finland.

[20] Odunfa, S.O., Owolabi, A.O., Aiyedun, P.O., Sadiq, O.M. (2018): Geotechnical assessment of pavement failure along Lagos-Ibadan Expressway. *FUOYE Journal of Engineering and Technology*, 3(2), pp. 113–117.

[21] Woods, W.R., Adcox, J.W. (2006): A general characterization of pavement system failures with emphasis on a method for selecting repair process. *Journal of Construction and Transportation,* l4(2), pp. 26–34.

[22] Ahmed, M.Y., Nury, A.H., Islam, F., Alam, M.J.B. (2012): Evaluation of geotechnical properties and structural strength enhancing road pavement failure along Sylhet-Sunamganj highway, Bangladesh. *Journal of Soil Science and Environmental Management,* 3(5), pp. 110–117.

[23] Asif, A.R., Ali, S.S., Noreen, N., Ahmed, W., Khan, S., Khan, M.Y., Waseem, M. (2016): Correlation of electrical resistivity of soil with geotechnical engineering parameters at Wattar area district, Nowshera, Khyber Pakhtunkhwa, Pakistan. *Journal of Himalayan Earth Sciences,* 49(1), pp. 124–130.

[24] Hen-Jones, R.M., Hughes, P.N., Stirling, R.A., Glendinning, S., Chambers, J.E., Gunn, D.A., Cui, Y.J. (2017): Seasonal effects on geophysical–geotechnical relationships and their implications for electrical resistivity tomography monitoring of slopes. *Acta Geotechnica,* 12, pp. 1159–1173.

[25] Bouassida, M., Manigniavy, S.A., Azaiez, D., Bouassida, Y. (2022): New approach for characterization and mitigation of the swelling phenomenon. *Frontiers in Built Environment,* 8, 836277, DOI:10.3389/fbuil.2022.836277.

[26] Falowo, O.O. (2020): Engineering site investigation and shallow foundation design in Ore Area of Ondo State, Nigeria. *Materials and Geoenvironment*, 67(1), pp. 21–33, DOI:10.2478/rmzmag-2020-0004.

Original Scientific Article • DOI: 10.2478/rmzmag-2021-0020

Received: March 20, 2022

Accepted: April 05, 2022

Petrophysical Evaluation of H-field, Niger Delta Basin for Petroleum Plays and Prospects

Petrofizikalna ocena H-polja v bazenu delte reke Niger za scenarije ogljikovodikov in prospekcije

Thomas A. Harry[1], Camillus E. Etim[1], Agbasi E. Okechukwu[2,*]

[1]Department of Geology, Akwa Ibom State University, Mkpat-Enin, Nigeria

[2]Department of Physics, Michael Okpara University Agriculture, Umudike, Nigeria

*Corresponding author: E-mail: agbasi.okechukwu@gmail.com

Abstract in English

As a result of a combination of several methodologies, the H-Field, Niger-Delta, has been delineated. To identify probable reservoirs, seals, and source rocks in the study area, this study integrates sequence stratigraphy with petrophysical concepts through a comprehensive analysis of 3D seismic and well logging datasets. According to the 3D facies model, reservoirs are dominated by sand and are laterally extensive. They were then upscaled and stochastically distributed to create a 3D reservoir property model. On average, the porosity of these clastic reservoirs ranges from 22 to 28%. Reservoir net-to-gross (NTG) ratios range from 0.67 to 0.96. Water saturation ranges from 8% to 30%, while hydrocarbon saturation ranges from 70% to 92%. Four gas-bearing units and six oil-bearing units are present in reservoirs P 0.5 and P 1 compartments. All reservoir intervals' oil and gas volumes are evaluated based on the hydrocarbon distribution. Geological models of the subsurface, such as the one in this paper, are crucial for future reservoir development programs.

Keywords: Niger Delta, Nigeria, Petrophysics, Reservoir Quality Assessment

Abstract in Povzetek

Na podlagi različnih metodologij je opisano H-polje v delti reke Niger. V pričujoči študiji so z namenom identifikacije možnih rezervoarjev, zapornih plasti in izvornih kamnin na podlagi celovite analize 3D seizmičnih podatkov ter popisov vrtin integrirani sekvenčna stratigrafija in petrofizikalni koncepti. Glede na 3D faciesni model v rezervoarjih dominira pesek. Rezervoarji so lateralno širokega obsega. Za izdelavo 3D modela lastnosti rezervoarja so bili faciesni modeli razširjeni v vertikalni smeri in stohastično razporejeni. V povprečju poroznost klastičnih rezervoarjev znaša med 22 in 28%. Neto do bruto (NTG) razmerja rezervoarja so med 0,6 in 0,96. Nasičenost z vodo je med 8% in 30%, medtem ko je nasičenost z ogljikovodiki od 70% do 92%. V P 0,5 in P1 delih rezervoarja so prisotne štiri enote s plinom in šest enot z nafto. Prostornine intervalov z nafto in plinom so ocenjene glede na razporeditev ogljikovodikov. Geološki modeli podlage, kakršen je ta, ki je predstavljen v tem članku, so ključni za prihodnje programe razvoja rezervoarja.

Ključne besede: delta reke Niger, Nigerija, petrofizika, ocean kvalitete rezervoarja

Introduction

Recent research breakthroughs in the energy industry aim to improve subsurface resource utilization through increased output. This may be accomplished by accurately predicting physical and fluid properties in 3D space in order to increase production efficient resource recapture [1]. The essential aspect that governs reservoir appraisal and simulation for improved exploitation and successful development is three-dimensional (3D) modeling of hydrocarbon resources. Despite 3D geological simulation in oil and gas reservoirs is simple utilizing different available software, factors will lead remains a significant barrier that has a significant impact on the successful exploitation of gas resources [2–5]. Data from

other sources may be included into the reservoir's 3D geologic feature models. Each cell is assigned properties by the modeling system, and numerical reservoir simulations are frequently cell-dependent. Such models impose much bigger loads on the geologist than conventional models do, because at any part of the reservoir's 3D volume, geology needs a complete explanation. Multi-integrated properties can be used to define a 3D geological model, which is critical for connecting data from a wellbore to a 3D geological model to create reservoir simulations [6–10].

The hydrocarbon prospective of the Niger Delta Basin's with its many fields and depobelts has yet to be completely realized. A thorough and correct fusion of petrophysical and sequence stratigraphic techniques will effectively provide a more accurate picture of reservoir attributes.

Identifying a field's depositional context is also crucial in determining reserves and designing optimal reservoir management strategies. Sands formed in various depositional conditions exhibit varying geometry in terms of its body patterns, form, size, and variability [11–12]. This indicates that the physical characteristics of sandstone reservoirs are the result of complex interplay of sedimentological processes. As a consequence, the reconstructing of sandstone successional sedimentological settings offers the ultimate framework for characterizing and evaluating reservoir character variation [13–15].

Given the existence of huge datasets of 2D/3D seismic lines, well logs, and biofacies from oil projects in the basin, the integration of sequence stratigraphy and petrophysics is still to be extensively utilised in the investigation of the Coastal Swamp depobelt. The success of peripheral field operators demonstrates the substantial opportunities of the Niger Delta basin's onshore sections. In other words, proper application of petrophysical investigations within those marginal fields would yield additional and greater deposits. This is due to the inclusive process of analysis being robust enough to scan the delta's diverse, different structural and stratigraphic features [16].

The current study aims to provide a new set of prospect evaluation in field optimistic parts for modeling reservoir characteristics in the Niger Delta Basin.

Geology of the study area

The study field is located in the Niger Delta Basin, south of the Atlantic, between latitudes 4°N and 6°N and longitudes 3°E and 9°E. It is a huge rift basin surrounded by several other basins in the offset region that have had comparable histories. The geologic setting of the Qua Ibo collapse summarizes the basin's tectonostratigraphic framework, which originated when a major piece of the southern margin of the Niger Delta underwent catastrophic failure and slid oceanward as a result of volcanism in the Cameroon hinterland [17].

The H-Field under investigation is located in the offshore depobelt region. Figure 1 depicts a schematic map of the research area, highlighting the possible locations of examined wells. From the bottom up, the

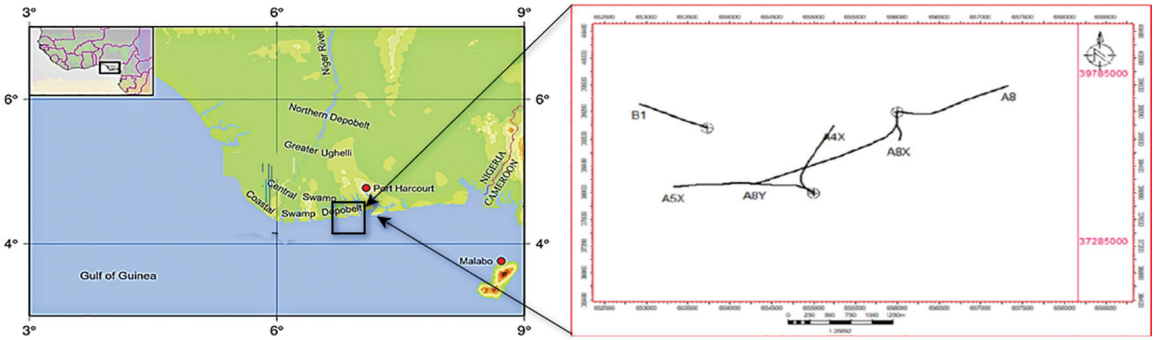

Figure 1: *This map depicts a generic location map of the research region as well as the basic concession map.*

basin comprises three thick, prominent lithostratigraphic units: the AKata Formation, the Agbada Formation, and the Benin Formation. The Paleocene Akata Formation is distinguished by marine shales with excellent source rock characteristics, and its maximum thickness can reach 20,000 feet in the delta's center region [18–20]. The largest source of hydrocarbons is the Eocene Agbada Formation, which formed in a deltaic to the fluvial-deltaic system directly above the Akata Formation. The Niger Delta Basin has a peak Agbada Formation thickness of around 9000 ft. The Benin Formation is the most recent stratigraphic unit, and it is composed mostly of fluviatile sediments [21].

The H-field is located in the Niger Delta's offshore region at a water depth of roughly 12 meters. The 3D seismic survey of H-field was completed in 1996 after being acquired in 1994. It covered approximately 400 km^2, and was conducted in shallow water using a land-type geometry. The inline and crossline processing spacing was 25m. The seismic data is generally of good quality and allows a reliable interpretation to be carried out over the major part of the field area. Before the start of the 2002 drilling campaign, a complete re-interpretation and mapping exercise of the top H3600 and top H3900 reservoirs was carried out using the reprocessed OPL98 3D seismic dataset, integrating all existing well data. Depth maps were generated using a complex depth conversion to account for a pull-down effect due to gas in the eastern part of the field. The 2002 drilled wells are largely used in seismic to well tie and confirming the interpreted structural.

The field structure is on a tilted horst in the central part of the macrostructure. Static reservoir models have been constructed for the H3600 and H3900 reservoirs for computing oil and gas volumes.

Materials and methods

Data sets

This study combines checkshot data, deviation data, geological reports, wireline logs (caliper, compressional sonic slowness, density, gamma-ray, neutron, and resistivity) and 3D seismic volume from H-field drilled wells. There were seven wells available: B1, A5X, A8Y, A4X, A8X, A8 and A1. The methodologies and workflow used in this work are represented in Figure 2.

Well log correlation

The correlation was performed across the wells, and suitable sand makers were identified to designate the reservoir units of significance [22–25]. The hydrocarbon-bearing sands were identified for examination of the field's reservoir potential and mapped at real vertical depth underwater [26–27]. The logs were used to delineate the parasequences and system tracts to determine the depositional settings [22]. The checkshot data has been used to match the depth and time of the seismic and well data (Well to seismic tie). This was also used to pick and determine the depth of the postulated horizons and faults.

Petrophysical analysis

The petrophysical analysis of logs was aimed mainly at determining the reservoir properties using a variety of qualitative and quantitative techniques. The GR logs were used for shale volume determination and lithology identification through discriminating between shale and non-shale beds. The resistivity logs were used in combination with the GR logs to distinguish among oil-gas and non-oil-gas bearing sections. By correlating equivalent intervals of log motif, the gamma-ray log was employed to achieve lithologic correlation of homologous strata among wells [14]. This was expanded to include the lateral extent of prospective hydrocarbon reserves calculated by connecting units across wells. Correlation panels are used to present the results. The well logs were used to construct many crossplots to identify the various correlations among reservoir rock properties characteristics and how they impact the reservoir's ability to retain or transfer fluid [28].

Shale volume estimation

The volume of shale (V_{sh}), which constitutes approximately of shale material in a sandstone or heterolith reservoir, was calculated using

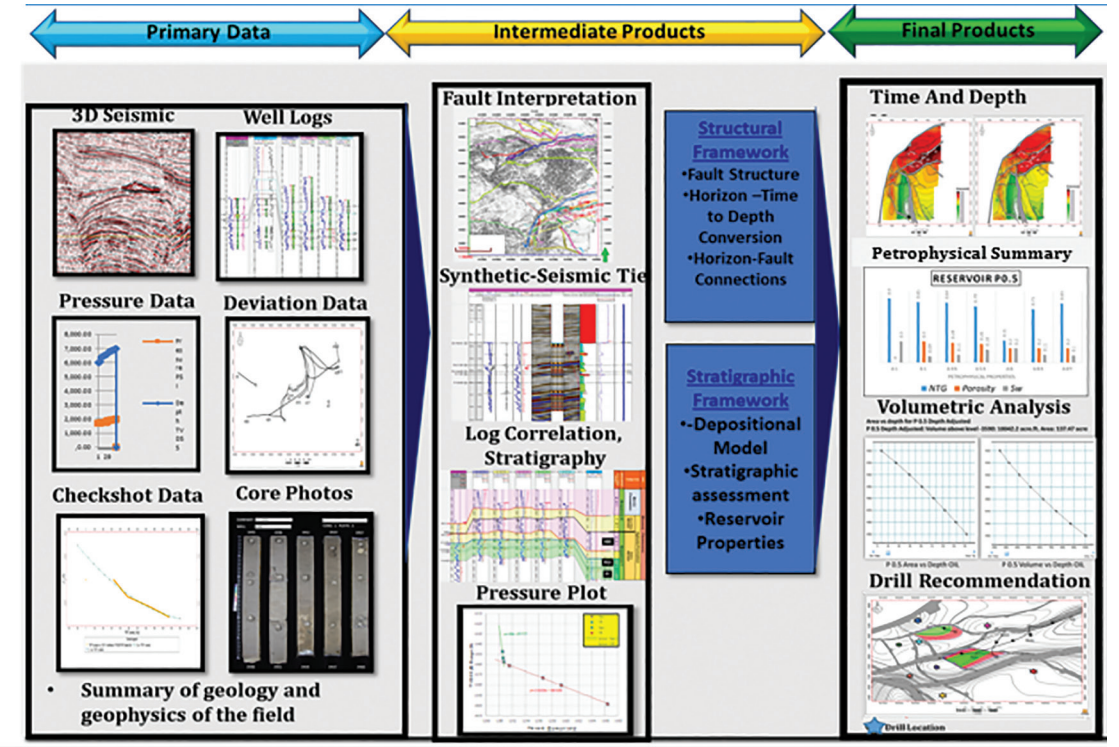

Figure 2: *Flowchart for the methodology utilized in the current study.*

equation 1 [29], that incorporates gamma-ray index (GR) estimates in equation 2.

$$V_{sh} = 0.083^{(2(3.7\times IGR))} \quad (1)$$

$$I_{GR} = \frac{GR_{log} - GR_{min}}{GR_{max} - GR_{min}} \quad (2)$$

where I_{GR} = gamma-ray index, GR_{log} = chosen log value, and GR_{min} and GR_{max} are the values used for the sand and shale foundation lines.

Determination of porosity

Porosity is described as the proportion of cavities to overall amount of rock (Agbasi, et al. 2021). As shown in equation 3, this variable is calculated by using bulk density values obtained from the formation density log.

$$\phi = \frac{\rho_{ma} - \rho_b}{\rho_{ma} - \rho_f} \quad (3)$$

where ϕ = Apparent density porosity, ρ_{Ma}= Matrix density, ρ_b = Bulk density log reading, ρ_f = Fluid density.

Water and hydrocarbon saturation

To compute uninvaded region water saturation, a water resistivity (R_w) estimate at formation temperature calculated from porosity and resistivity records inside clean water zones is employed. To measure the saturation of the reservoir sands' fluid content, the formation water saturation was first calculated in equation 4 using Archie's water saturation equation:

$$S_w^n = \frac{FR_w}{R_t} \quad (4)$$

where n = saturation exponent, R_w = formation water resistivity, R_t = rock resistivity and F = formation factor.

Hydrocarbon Saturation (S_h) is the proportion of pore volume filled by hydrocarbon in a formation. As indicated in equation 5, it can be computed by deducting the number derived from water saturation from 100 percent.

$$S_h = (100 - S_w)\% \quad (5)$$

where S_h = Hydrocarbon Saturation.

Permeability determination

K denotes a rock's capacity to carry fluids. For each reservoir, permeability is evaluated using equation 6.

$$K = \sqrt{\frac{250 \times Ø^2}{S_{wir}}} \quad (6)$$

where S_{wir} = irreducible water saturation.

Volumetric hydrocarbon estimation

The use of one or more mathematical models to characterize the petroleum porous structure in the reservoir and also the volumetric migration from of the reservoir to the surface was required for probabilistic hydrocarbon in situ assessment. The hydrocarbon in place was assessed using the net pay zone's average percentage hydrocarbon saturation [5]. The initial oil in situ (OIIP) is calculated as follows:

$$OIIP = GRV \times \frac{N}{G} \times \phi \times (1 - S_w) \quad (7)$$

GRV = Gross Rock Volume, $\frac{N}{G}$ = Net-to Gross, ϕ = Porosity, S_w = Water Saturation.

Results and discussion

In the studied H-Field, a well tie between the wells was based on the motif sand model (Figure 3) and stratigraphic correlation (Figure 4). The identified reservoirs were classified as P 0.5 and P1. Variable hydrocarbon contact across reservoirs suggests compartmentalization. Reservoir ABC, P0.5, and P1 are Biafra sands, and Reservoir ABC is not widespread as it is frequently truncated by the Qua-Iboe Channel erosive unconformity. P0.5, and P1 are lowstand reservoir facies. As shown in Figure 5, faults and horizons are delineated in the seismic volume using well log-based inferences. Fault pillars were identified and structural modeling was implemented based on the seismic volume's horizon and fault mapping (Figure 6).

It is possible to see a network of faults in time (Figure 7) and depth (Figure 8) maps that cover up to 66% of the surveyed area. Syn-depositional listric faults and small antithetic faults dominate the whole map region. Normal faults have a NW-SE trend and a SW dip. As a result of these structural patterns, the H-Field was able to capture hydrocarbons.

Petrophysical research identified two primary reservoir intervals, P 0.5 and P 1, with

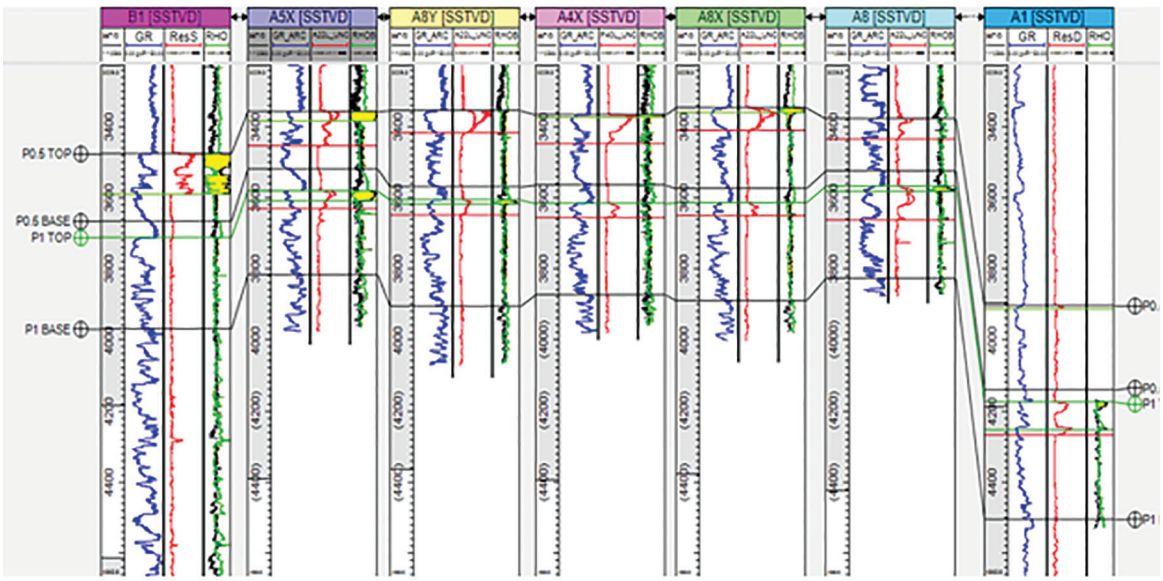

Figure 3: *Well log correlations between the wells analyzed.*

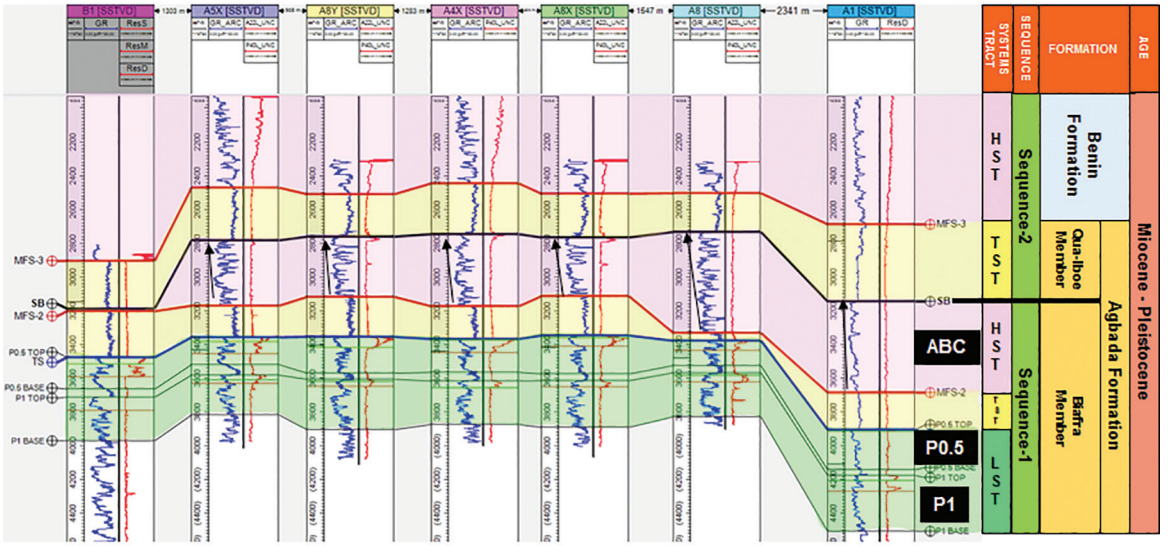

Figure 4: *Well log correlations between the studied wells with stratigraphic correlation.*

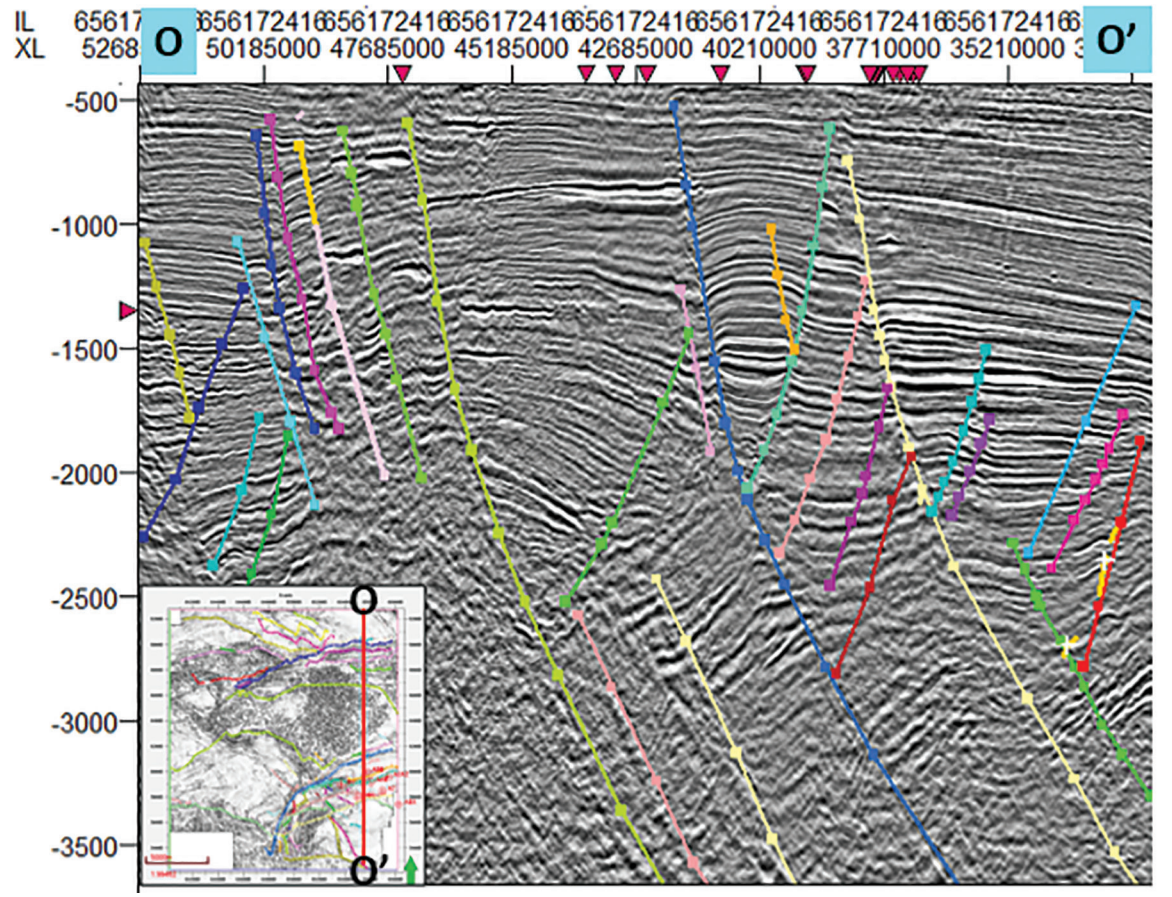

Figure 5: *Fault framework as delineated in the seismic sections.*

depths ranging from low to deeper. Well logs and seismic horizon modeling both demonstrate that all of these reservoirs are widely expansive throughout the simulated region and are impacted by the fault lines. The porosity in these reservoirs ranges between 22 and 29 percent on average. The reservoir net-to-gross (NTG) ratio varies from 0.67 to 0.96.

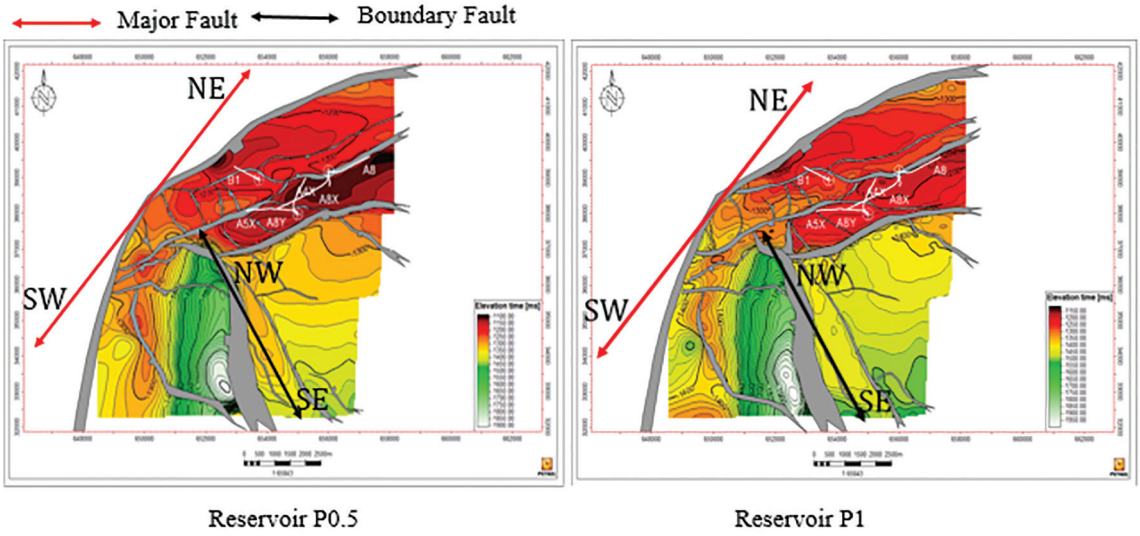

Figure 6: *Horizon and fault mapping for Reservoir P 0.5 and P 1.*

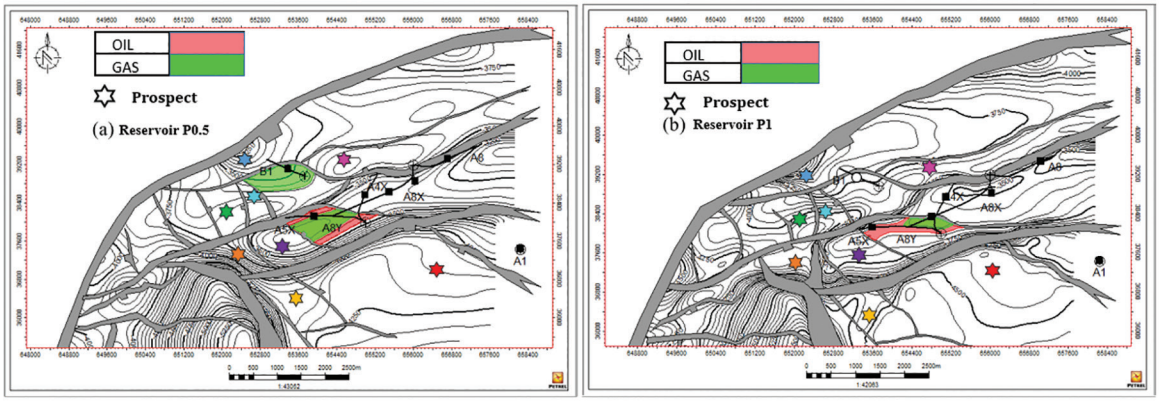

Figure 7: *Depth map for reservoir P 0.5 and P 1 showing GOC from both reservoirs.*

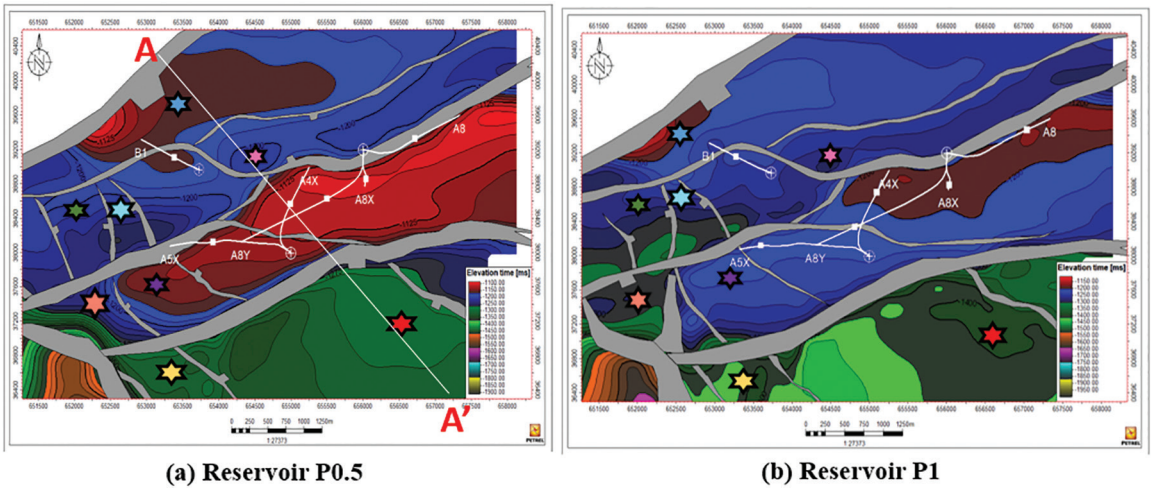

Figure 8: *Time attribute map for reservoir P 0.5 and P 1.*

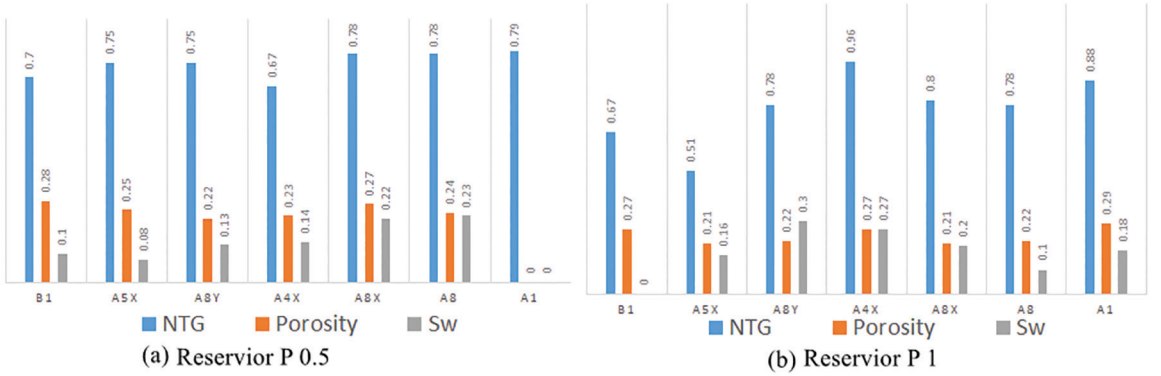

Figure 9: *Summary of the result of the petrophysical analysis from the studied wells for both Reservoir (a) P 0.5 and (b) P 1.*

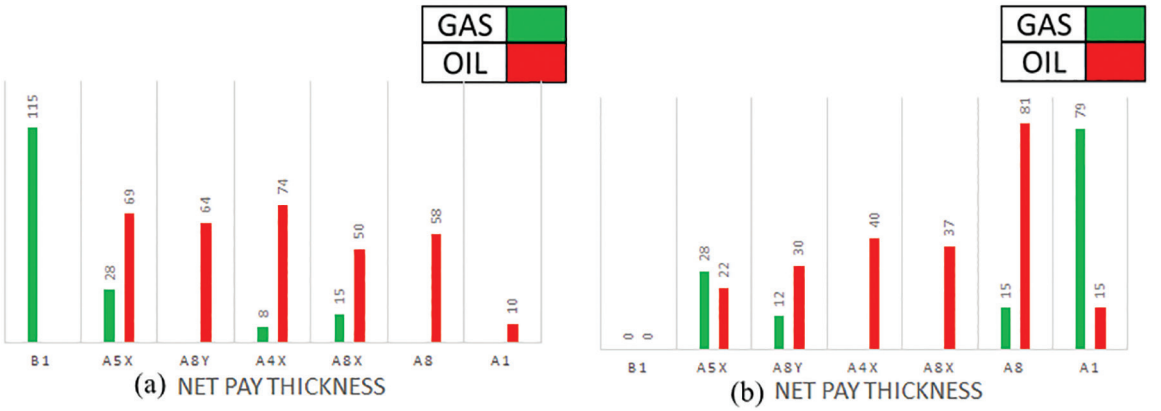

Figure 10: *Summary of the result of the net pay thickness for oil and gas in reservoirs P 0.5 and P 1.*

Water saturation varies from 8% to 30%, while hydrocarbon saturation values vary from 70% to 92%.

According to Figure 9a, well A1 has the greatest NTG value of 0.79 in reservoir P 0.5, whereas well A4X has the lowest NTG value of 0.67. Well B1 has a maximum effective porosity rating of 0.28, whereas well A8Y has the lowest mean value of 0.22. The hydrocarbon saturation is greatest in well A5X at 0.92 and lowest in well A8 at 0.77. In reservoir P1, well A4X has the maximum NTG rating of 0.96, whereas well A5X has the minimum NTG value of 0.51.Well A1 has the highest effective porosity value of 0.29, while wells A5X and A8X have the lowest value of 0.21. The hydrocarbon saturation is greatest in well A8 at 0.90 and lowest in well A8Y at 0.70.

Figure 9 (a & b) depicts a summary graphic of the average values of the results. The H-field has often been demonstrated to have very good to good reservoir quality. Furthermore, the effective porosities are excellent and the hydrocarbon saturation is high. As a result, the field has a significant chance of producing hydrocarbons. When compared to the reservoirs, the sand facies are less laterally extensive and more irregular, resulting in a larger NTG range and more unpredictability water saturation.

The results presented in Figure 10 show that four gas-bearing units and six oil-bearing units are present in reservoirs P 0.5 and P 1. The dominant reservoir fluid type is oil. Figure. 11 shows the 3D static model for wells A5X and B1. Well A5X has both Gas-Oil-Contact (GOC) at 3384ft and Oil-Water-Contact (OWC) at 3453ft. Figure 11 depicts Well B1's only Gas Water Contact (GWC) at 3590 ft. Static reservoir simulation is used to generate the lateral and longitudinal dispersion of the inferred hydrocarbons, which is shown in Figure. 11. The calculated stock tank oil initially in place (STOOIP) and gas initially in place is shown in Table 1 for wells A5X and B1. Figure 12 shows viable prospects in the H-field for exploration.

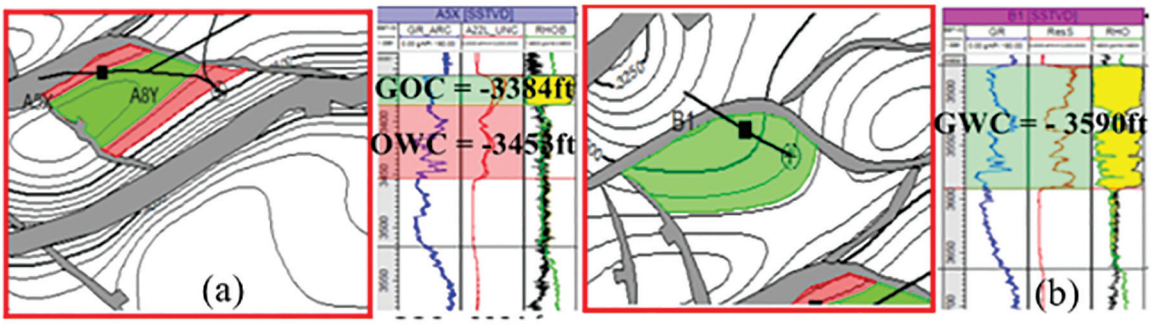

Figure 11: *Oil-gas-water contact in reservoirs P 0.5 and P 1.*

Table 1: *Estimates of mean; porosity, NTG, water saturation, and hydrocarbon volume in the two examined H-Field reservoir intervals.*

Reservoir Interval	Average Porosity (%)	Average NTG (%)	Average Water Saturation (%)	Average Pay Thickness (Gas)	Average Pay Thickness (Oil)	GIIP (BSCF)	STOIIP (MMSTB)
P 0.5	24.3	74.5	64	41.75	54.16	23.83	11.5
P 1	24.1	76	73	33.5	37.5	0.64	1.13

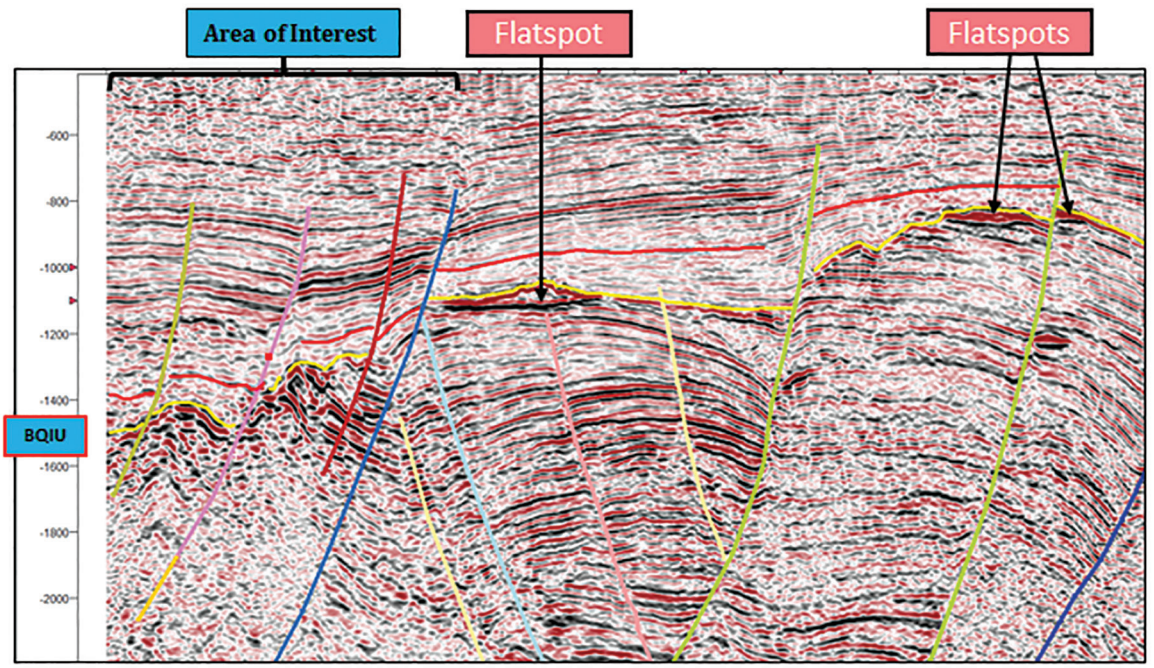

Figure 12: *Viable prospects in the H-field for exploration.*

Conclusion

This study used sequence stratigraphy and petrophysical approaches to predict prospective petroleum plays and prospects for the H-field in the Niger Delta Basin. The current 3D static reservoir simulation provides a better knowledge of the reservoir facies, structural type, and petrophysical parameters' field-wide dispersion. Because of their distinct petrophysical and sequence stratigraphic features, two large clastic reservoir sand sections were regarded as attractive hydrocarbon possibilities. Seismic

interpretation and 3D structural modeling are used to evaluate NW-SE trending normal faults that affect hydrocarbon trapping in the research area. According to facies modeling, the sand-dominated reservoir facies has substantial lateral continuity. The porosity range is 22–28 percent, according to the 3D reservoir petrophysical simulation. Utilizing rock properties fluid variety data and volumetric assessment of in-place hydrocarbons, it was found that oil, gas, and water are available in the reservoirs in various proportions so the amounts are sufficient to support effective exploration and mining activities to a certain degree. The subsurface geological model given in this paper is essential for future reservoir development efforts. It could aid in the identification of future well locations. The reservoir models will be more detailed and fine-tuned depending on the prospective well data set in the future.

References

[1] Yu, X.Y., Ma, Y.Z., Psaila, D., Pointe, P.L., Gomez, E., Li, S. (2011): Reservoir characterization and modeling - A look back to see way forward. In: *Uncertainty and reservoir modeling*, Ma, Y.Z., La Pointe, P.R (eds.). AAPG Memoir, pp. 289–309.

[2] Adelu, A.O., Aderemi, A.A., Akanij, A.O., Sanuade, O.A., Kaka, S.I., Afolabi, O., Olugbemiga, S., Oke, R. (2019): Application of 3D static modeling for optimal reservoir characterization. *Journal of African Earth Sciences*, 152, pp. 184–196, DOI:10.1016/j.jafrearsci.2019.02.014.

[3] Adeoti, L., Onyekachi, N., Olatinsu, O., Fatoba, J., Bello, M. (2014): Static reservoir Modeling Using Well Log and 3-D Seismic Data in a KN Field, Offshore Niger Delta, Nigeria. *International Journal of Geosciences*, 5, pp. 93–106.

[4] Jika, H.T., Onuoha, K.M., Dim, C.I.P. (2020): Application of geostatistics in facies modeling of Reservoir-E, "Hatch Field" offshore Niger Delta Basin, Nigeria. *Journal of Petroleum Exploration and Production Technology*, 10, pp. 769–781, DOI:10.1007/s13202-019-00788-1.

[5] Okoli, E.A., Agbasi, O.E., Lashin, A.A., Sen, S. (2021): Static Reservoir Modeling of the Eocene Clastic Reservoirs in the Q-Field, Niger Delta, Nigeria. *Natural Resources Research*, 30(2), pp. 1411–1425, DOI:10.1007/s11053-020-09804-2.

[6] Adesoji, O.A., Oluseun, A.S., SanLinn, I.K., Isaac, D.B. (2018): Integration of 3D Seismic and Well Log Data for the Exploration of Kini Field, Offshore Niger Delta. *Petroleum and Coal*, 60(4), pp. 752–761.

[7] Ahmed, H., Nyeche, M., Engel, S., Nworie, E., Mooij, H. (2011): 3D reservoir simulation of X field onshore Niger Delta, Nigeria: The power of multiple iterations. In: *SPE Nigeria International Conference and Exhibition*, Abuja, Nigeria, July 30-Aug 3. SPE-150730-MS. DOI:10.2118/150730-MS.

[8] Edwin, E.V., Jose, L.P., Carlos, A.M., María, C.H. (2011): High Resolution Stratigraphic Controls on Rock Properties Distribution and Fluid Flow Pathways in Reservoir Rocks of The Upper Caballos Formation, San Francisco Field, Upper Magdalena Valley, Colombia. In: *South American Oil and Gas Congress*, *SPE Western Venezuela Section*, Maracaibo, Venezuela, Oct 18-21. SPE WVS 095.

[9] Godwill, P.A., Waburoko, J. (2016): Application of 3D Reservoir Modeling on Zao 21 Oil Block of Zilaitun Oil Field. *Journal of Petroleum Environmental and Biotechnology*, 7, p. 262, DOI:10.4172/2157-7463.1000262.

[10] Oluwadare, O.A., Osunrinde, O.T., Abe, S.J., Ojo, B.T. (2017): 3-D Geostatistical Model and Volumetric Estimation of 'Del' Field, Niger Delta. *Journal of Geology and Geophysics*, 6, p. 291, DOI:10.4172/2381-8719.1000291.

[11] Inyang, N.J., Akpabio, O.I., Agbasi, O E. (2018): Shale Volume and Permeability of the Miocene Unconsolidated Turbidite Sand of Bonga Oil Field, Niger Delta, Nigeria. *International Journal of Advanced Geoscience*, 5(1), pp. 37–45, DOI:10.14419/ijag.v5i1.7586.

[12] Olubunmi, C.A., Olawale, O.A. (2018): Structural Interpretation, Trapping Styles and Hydrocarbon Potential of Block-X, Northern Depobelt, Onshore Niger Delta. In: *AAPG Annual Convention and Exhibition*, Salt Lake City, Utah, May 20–23.

[13] Oyeyemi, K.D., Olowokere, M.T., Aizebeokhai, A.P. (2018): Hydrocarbon resource evaluation using combined petrophysical analysis and seismically derived reservoir characterization, offshore Niger Delta. *Journal of Petroleum Exploration and Production Technology*, 8, pp. 99–115, DOI:10.1007/s13202-017-0391-6.

[14] Agbasi, O.E., Igboekwe, M.U., Chukwu, G.U., Sunday, E.E. (2018): Discrimination of pore fluid and lithology of a well in X Field, Niger Delta, Nigeria. *Arabian Journal of Geosciences*, 11, p. 274, DOI:10.1007/s12517-018-3610-7.

[15] Agbasi, O.E., Inyang, N., Ibout, J. (2013): Estimation of Water Saturation in Niger Delta Nigeria Using Wire-Line logs. *Journal of Applied Physics (IOSR-JAP).* 3(4), pp. 66–71.

[16] Inyang, N.J., Agbasi, O.E., Akpabio, G.T. (2021): Integrated analysis of well logs for productivity prediction in sand-shale sequence reservoirs of the Niger Delta—a case study. *Arabian Journal of Geoscience* 14(7), p. 587, DOI:10.1007/s11053-020-09804-2.

[17] Harry, T.A., Etuk, S.E., Joseph, I.N., Okoli, E.A. (2018): Geomechanical evaluation of reservoirs in the coastal swamp, Niger delta region of Nigeria. *International Journal of Advanced Geoscience.* 6(2), pp. 165–172, DOI:10.14419/ijag.v6i2.13762.

[18] Igboekwe, M.U., Agbasi, O.E., Chukwu, G.U., Etuk, S.E. (2021): Delineation of apparent water resistivity and porosity exponent of the Miocene unconsolidated sandstone reservoir of coastal swamp depobelt, Niger Delta, Nigeria. *Journal of Sedimentary Environments.* 6(5), pp. 551–559, DOI:10.1007/s43217-021-00068-1.

[19] Ejedavwe, J., Fatumbi, A., Ladipo, K., Stone, K. (2002): Pan-Nigeria exploration well look—back (Post-Drill Well Analysis). Shell Petroleum Development Company of Nigeria Exploration Report 2002.

[20] Doust, H., Omatsola, E. (1990): Niger Delta. In: *Divergent/passive margin basins*, Edwards, J.D., Santogrossi, P.A. (eds.). AAPG Memoir, 48, pp. 239–248.

[21] Tuttle, M.L., Charpentier, R.R., Brownfield, M.E. (1999): The Niger Delta petroleum system; Niger Delta Province, Nigeria, Cameroon, and Equatorial Guinea, Africa. United States Geological Survey (USGS) Open-File Report 99-50- H, DOI:10.3133/ofr9950H.

[22] Adiela, U.P. (2018): Reservoir Modeling Using Seismic Attributes and Well Log Analysis: A Case Study of Niger Delta, Nigeria. In: *AAPG International Conference and Exhibition*, Cape Town, South Africa, Nov 4–11.

[23] Egbe, T., Ugwu, S.A., Ideozu, R.U. (2019): Reservoir Characterization of Buma Field Reservoirs, Niger Delta using Seismic and Well Log Data*. Petroleum and Chemical Industry International*, 2(4), pp. 1–11.

[24] Farouk, I.M., El-Arabi, H.S., Mohamed, S.F. (2017): Reservoir Petrophysical Modeling and Risk Analysis in Reserve Estimation; A Case Study from Qasr Field, North Western Desert, Egypt. *Journal of Applied Geology and Geophysics (IOSR-JAGG)*, 5(2), pp. 41–52.

[25] Ndip, E.A., Agyingyi, C.M., Nton, M.E., Oladunjoye, M.A. (2018): Seismic Stratigraphic and Petrophysical Characterization of Reservoirs of the Agbada Formation in the Vicinity of 'Well M', Offshore Eastern Niger Delta Basin, Nigeria. *Journal of Geology and Geophysics*, 7, pp. 1–9, DOI:10.4172/2381-8719.1000331

[26] Ismail, A., Raza, A., Gholami, R., Reza, R. (2020): Reservoir characterization for sweet spot detection using color transformation overlay scheme. *Journal of Petroleum Exploration and Production Technology,* 10, pp. 2313–2334, DOI:10.1007/s13202-020-00913-5.

[27] Kalu, C.G., Obiadi, I.I., Amaechi, P.O., Ndeze, C.K. (2020): Petrophysical Analysis and Reservoir Characterization of Emerald Field, Niger Delta Basin, Nigeria*. Asian Journal of Earth Sciences*, 13, pp. 21–36, DOI:10.3923/ajes.2020.21.36.

[28] Okoli, E.A., Agbasi, O.E., Samuel, O.O., Etuk, S.E. (2018): Crossplot analysis of rock properties from well log data for gas detection in X-field, coastal swamp depobelt, Niger Delta Basin. *Journal of Geoscience, Engineering, Environment and Technology*, 3(4), pp. 180–186, DOI:10.24273/jgeet.2018.3.4.1318.

[29] Larionov, V. (1969): *Radiometry of Boreholes*. NEDRA: Moscow, pp. 238–240.

[30] Agbasi, O.E., Igboekwe, M.U., Chukwu, G.U., Etuk, S.E. (2021): Formation evaluation of reservoirs in Eocene, Niger Delta Nigeria using modified formation factor from Pickett's plot. *Modeling Earth Systems and Environment*. 6(4), pp. 1–10, DOI:10.1007/s40808-020-01009-z.

RMZ – Materials and Geoenvironment
RMZ – Materiali in geookolje
ISSN 1408-7073

Old title/Star naslov
Mining and Metallurgy Quarterly/Rudarsko-metalurški zbornik
ISSN 0035-9645, 1952–1997

Published by/Izdajatelj
Faculty of Natural Sciences and Engineering, University of Ljubljana/
Naravoslovnotehniška fakulteta, Univerza v Ljubljani

Associated Publisher/Soizdajatelj
Institute for Mining, Geotechnology and Environment, Ljubljana/
Inštitut za rudarstvo, geotehnologijo in okolje
Velenje Coal Mine/Premogovnik Velenje
Slovenian Chamber of Engineers/Inženirska zbornica Slovenije

Editorial Office/Uredništvo
Technical editors/Tehnična urednika Blaž Janc and Jože Žarn
Secretary/Tajnica Nives Vukič

Editorial Address/Naslov uredništva
RMZ – Materials and Geoenvironment
Aškerčeva cesta 12, p. p. 312
1001 Ljubljana, Slovenija
Tel.: +386 (0)1 470 46 10
Fax.: +386 (0)1 470 45 60
E-mail: bostjan.markoli@ntf.uni-lj.si
joze.zarn@ntf.uni-lj.si

Published/Izhajanje
4 issues per year/4 številke letno

Partly funded by Ministry of Education, Science and Sport of Republic of Slovenia./Pri financiranju revije sodeluje Ministrstvo za izobraževanje, znanost in šport Republike Slovenije.

Articles published in Journal "RMZ M&G" are indexed in international secondary periodicals and databases:/Članki, objavljeni v periodični publikaciji „RMZ M&G", so indeksirani v mednarodnih sekundarnih virih:
CA SEARCH® – Chemical Abstracts®, METADEX®, GeoRef.

Annual subscription for individuals in Slovenia: 20 EUR, for institutions: 30 EUR. Annual subscription for the rest of the world: 30 EUR, for institutions: 50 EUR/Letna naročnina za posameznike v Sloveniji: 20 EUR, za inštitucije: 30 EUR. Letna naročnina za tujino: 30 EUR, inštitucije: 50 EUR

Transaction account/Tekoči račun
Nova Ljubljanska banka, d. d., Ljubljana: UJP 01100-6030708186

VAT identification number/Davčna številka
24405388

Online Journal/Elektronska revija
https://content.sciendo.com/view/journals/rmzmag/rmzmag-overview.xml?result=4&rskey=iClOT4#

ISSN 1408-7073